Title

Dynamics of pyroclastic density currents and submarine eruptions

Author

Fauria, Kristen

Publication Date

2017

Dynamics of pyroclastic density currents and submarine eruptions

by

Kristen E. Fauria

A dissertation submitted in partial satisfaction of the
requirements for the degree of
Doctor of Philosophy

in

Earth and Planetary Science

in the

Graduate Division

of the

University of California, Berkeley

Committee in charge:

Professor Michael Manga, Chair
Professor William E. Dietrich
Assistant Professor Laurel Larsen

Fall 2017

Dynamics of pyroclastic density currents and submarine eruptions

Abstract

Dynamics of pyroclastic density currents and submarine eruptions

by

Kristen E. Fauria

Doctor of Philosophy in Earth and Planetary Science

University of California, Berkeley

Professor Michael Manga, Chair

Density gradients are fundamental drivers of volcanic flows. Pyroclastic density currents propagate because they are more dense than the ambient fluid and pyroclasts can rise through water as a result of their buoyancy. This dissertation focuses on understanding the processes that govern the density evolution, and therefore the fate of, pyroclasts in water and pyroclastic density currents. Chapter 2 examines how the entrainment of substrate material affects the density and runout distance of dilute pyroclastic density currents (PDCs). I use experiments to validate a clast-scale model for particle entrainment and then develop a one-dimensional PDC model to examine the effects of particle entrainment on large-scale PDC behavior. I conclude that particle entrainment can increase the distance PDCs travel by an order of magnitude. Chapter 3 explores the density evolution of individual pyroclasts in water. Understanding the behavior of single clasts is foundational for understanding the dynamics of submarine eruptions. Through experiments I discover that pyroclasts cool in multiple stages, that water ingestion accelerates cooling, and that saturation is limited by heat transfer rather than permeability. I test these interpretations with quantitative models that can later be used to build and validate models of large-scale submarine plume dynamics. While Chapter 3 shows why large pyroclasts can get to the surface from great depths, Chapter 4 explains why pyroclasts may float at the surface once they arrive there. It has been known that pyroclasts can float at the ocean surface for years, and yet previous models for pumice saturation predict rapid sinking. In Chapter 4 I propose that pumice floats on water because of the trapping of non-condensable gases. Gas trapping refers to the isolation of gas by water within pore throats such that the gas becomes disconnected from the atmosphere and unable to escape. I use X-ray microtomography experiments to confirm this gas trapping hypothesis and then use laboratory experiments to conclude that pumice eventually sinks because of the outward diffusion of trapped gas. Together this work exemplifies how small-scale processes can modify clast and PDC density and govern the fate of volcanic material in both the oceans and on land.

Contents

Contents **i**

List of Figures **iv**

List of Tables **ix**

1 Introduction **1**

2 Effect of particle entrainment on the runout of pyroclastic density currents **3**
- 2.1 Summary . . . 3
- 2.2 Introduction . . . 4
- 2.3 Conceptual Model of Dilute Pyroclastic Density Currents . . . 5
- 2.4 Particle splash experiments . . . 6
  - 2.4.1 Experimental and Splash Function scaling . . . 6
  - 2.4.2 Experimental Methods . . . 6
  - 2.4.3 Experimental results . . . 8
- 2.5 Splash Function . . . 9
  - 2.5.1 Splash Function validation . . . 11
- 2.6 One-dimensional model a dilute pyroclastic density current that entrains air and sediment . . . 13
  - 2.6.1 1D PDC model results . . . 15
- 2.7 Discussion . . . 18
  - 2.7.1 Quantification of particle entrainment . . . 18
  - 2.7.2 The effect of particle entrainment on PDC runout distance . . . 18
  - 2.7.3 Entrainment processes in dilute PDCs . . . 20
- 2.8 Conclusions . . . 21
- 2.9 Acknowledgements . . . 22
- 2.10 appendix . . . 22
  - 2.10.1 Splash Function comparison . . . 22
  - 2.10.2 Alternative Splash Functions . . . 24
  - 2.10.3 Settling Velocities . . . 24

3 Pyroclast cooling and saturation in water 27
3.1 Summary 27
3.2 Introduction 28
3.3 Experimental Methods 29
3.4 Results 32
  3.4.1 Cooling and saturation of a representative clast 32
  3.4.2 Initial temperature effects 33
  3.4.3 Conceptual models for pumice cooling and saturation 34
3.5 Quantitative models of pumice cooling and saturation 37
  3.5.1 Stage 1a: Saturation of pumice, $T_i < 100°\text{C}$ 37
  3.5.2 Stage 1a: Saturation of pumice $T_i > 100°\text{C}$ 38
  3.5.3 Stage 1b: Steam condensation drives saturation (why saturation is controlled by heat transfer) 39
  3.5.4 Stage 2: Conductive Cooling 43
  3.5.5 Stage 2: Saturation 45
  3.5.6 Estimating a stage 1 average cooling rate 46
  3.5.7 Estimating an average stage 1 liquid flux 48
3.6 Discussion 50
  3.6.1 Experimental and model limitations 50
  3.6.2 Application to submarine eruptions 52
3.7 Conclusions 53
3.8 Acknowledgements 54
3.9 Appendix 56
  3.9.1 Conductive Cooling on a Sphere 56
  3.9.2 Modified Stefan Problem 57
  3.9.3 Derivation of equation for trapped gas content 58
  3.9.4 Supplement 58

4 Trapped bubbles keep pumice afloat and gas diffusion makes pumice sink 64
4.1 Summary 64
4.2 Introduction 65
  4.2.1 Gas trapping in porous media 66
    4.2.1.1 Bypass trapping 67
    4.2.1.2 Snap-off trapping 68
    4.2.1.3 Percolation Model Predictions 68
4.3 X-ray microtomography 68
  4.3.1 Experimental Set-Up 68
  4.3.2 X-ray microtomography results 70
  4.3.3 Comparison to percolation theories 72
4.4 Mechanisms that cause pumice to sink 73
  4.4.1 Pumice floatation experiments 74
  4.4.2 Pumice floatation timescale 75

4.4.3 Pumice floatation results and model comparison 75
4.5 Discussion 77
4.5.1 Gas Trapping Timescale 77
4.5.2 Water saturation of hot versus cold pumice 77
4.5.3 Bypass versus snap-off trapping 79
4.5.4 Gas diffusion model 79
4.6 Conclusions 81
4.7 Acknowledgements 81

5 Conclusions and future directions 83
5.1 Future work: erosion by pyroclastic density currents and multiphase flows . . 83
5.2 Future work: submarine eruption dynamics 85
5.3 Conclusions 87

Bibliography 88

List of Figures

2.1 Conceptual model of a pyroclastic density current that can entrain loose substrate particles by particle splash. We hypothesize that splash-driven entrainment occurs in dilute regions of the current where the lower boundary of the flow lacks a bed load region and is dominated by particle fallout. 4

2.2 (a) A composite image (100 frames recorded at 600 fps) of a nylon sphere impacting sand and the resultant particle splash. (b) A schematic diagram of our experimental setup. The diameter of the hole in the stiff paper is 8 cm. The high-speed camera was in the foreground. 7

2.3 Experimental measurements of ejected mass over the mass of the incident particle, m_i, plotted against a dimensionless ratio of kinetic to potential energy. Our experimental results demonstrate that $\frac{N_e m_e}{m_i}$ increases with V_i^2 and that impacts can suspend masses greater than the incident particle mass (i.e., $\frac{N_e m_e}{m_i} > 1$). Wood spheres eject less mass than pumice for a given kinetic energy. 9

2.4 Measurements of particle splash from eight studies are plotted to solve for a mean restitution coefficient, e_n^2, which represents the fraction of energy retained during impact. The orange bars show the mean and standard deviation of the restitution coefficient for each study. For most studies, restitution coefficients fall within a small range. This demonstrates that the restitution coefficient is fairly constant for the range of materials, impact velocities, and angles used in each study. It is not surprising that e_n^2 varies between studies because different materials were used. Black symbols represent data from physical experiments, and gray symbols represent data from discrete element model (DEM) simulations. 10

2.5 Equation (2.3) is tested by substituting measured values from eight studies into equation (2.3). Equation (2.3) holds (plots on a 1:1 line) across a large parameter space ($0.25 < V_i < 81$ m s^1 and $0.02 < d_i < 2$ cm), suggesting that equation (2.3) is a valid Splash Function. Black symbols represent data from physical experiments, and gray symbols represent DEM simulations. The symbol shapes correspond to those in Figure 2.4. 12

2.6 (a) Density and (b) temperature model results as a function of distance within currents with four different particle sedimentation and entrainment regimes. All currents had an initial particle temperature of 600°C and initial mean PDC temperature of 457°C. The PDC that entrains cold particles runs out the farthest and has the highest mean density and lowest internal temperature. The PDC that entrains hot particles runs out the second farthest and has the second highest mean density but maintains the highest internal temperature. 16

2.7 Runout distance model results. Runout decreases with initial temperature for all currents. The occurrence and temperature of particle entrainment have order of magnitude effects on runout distance. PDCs that entrain cold particles run out the farthest. 17

2.8 The impact of bombs on the flank of Sakurajima volcano, Japan, on 22 July 2013 generates small density currents during a Vulcanian eruption. 20

2.9 Splash Function predictions versus the observed number of ejected particles from eight studies (Table 1). The symbols correspond to those shown in Figure 2.4. Gray represents data from numerical studies, and black represents data from physical experiments. Where d was unspecified we let . (a) Werner [1990]; (b and c) Oger et al. [2008]; (d) Anderson [1987] where $a = 1$; (e) Andreotti [2004]; (f) Wu [2013] where $e_n^2 = 0.008$ and $\alpha = 1$; and (g) the Splash Function from this study, equation (3), where $e_n^2 = 0.008$ and $\mu = 0.5$. Figure A1g (our Splash Function) shows that predictions match observations. 23

3.1 Experimental set-up. We measure the internal temperature and submerged weight of pumice clasts as they are cooled in a water bath. 30

3.2 Cooling and saturation of 7.9 g Medicine Lake clast ML03 from an initial temperature of 265°C. I measure internal temperature at two locations within the clast: 6 and 11 mm from the clast edge. I find that submerged weight increases and internal temperatures drop rapidly in the first 19 seconds following submersion. I observe bubbles flowing in the first $3 - 5$ seconds following submersion. I find that ΔM_S plateaus at the same time (≈19 s) internal temperatures reach local minima. 32

3.3 Effects of initial temperature on cooling and saturation. (A) Internal temperature of clast ML01 as a function of time. Clast internal temperature declines rapidly, then plateaus near 100°C, and finally drops quickly below 100°C. Initially hotter clasts take longer to cool below 100°C. (B) Liquid flux (g s^{-1}) into the clasts as a function of time. Clasts with initial temperatures below 100°C exhibit the lowest liquid fluxes. Otherwise, initial liquid flux decreases with increasing initial clast temperature. All clasts with initial temperatures above 100°C exhibit sharp high-to-low liquid flux transitions (marked with stars). The inset shows how the timing of the high-to-low liquid flux transition increases with clast initial temperature. 35

3.4 Cooling and saturation stages of representative clast ML01. We propose that cooling and saturation takes place in several stages and over which different processes dominate. Stage 1a: Water enters the clast as air flows out. Stage 1b: Ingested water is heated and converted to steam. As the clasts cool, internal steam condenses and generates a pressure gradient that draws in liquid water. Stage 1 ends once all internal steam has condensed. Stage 2: We propose that cooling occurs through conduction and saturation is controlled by the thermal contraction of trapped non-condensable gas. 36

3.5 Flow declines exponentially with time for clasts with initial temperatures < 100°C. I fit Equation 3.5 to measurements of liquid flux from clast ML02 and find that liquid flux increases with clast initial temperature. 38

3.6 Conceptual model of stage 1b cooling and saturation. Clasts contain steam in their interiors that cools and condenses as heat is conducted out of the clast. The production of latent heat from steam condensation balances outward heat conduction at the interface. Liquid water is drawn in at the velocity at which the condensation interface moves inward. The mathematical details of this model are given in Section 3.9.2. 39

3.7 Dimensionless liquid infiltration front location as a function of time. We use our experimental measurements to calculate the condensation front position (Equation 3.9 with $C_1 = 2.6$, black circles). I compare calculated front position to solutions from a modified Stefan model in spherical and planar geometries (Section 3.9.2). I find that, using similar Stefan numbers, the modified Stefan model matches our experimental measurements, lending support to the conceptual model for stage 1b depicted in Figure 3.6. 40

3.8 Stage 2 temperature as a function of dimensionless time, τ. I find that dimensionless temperature scales with $e^{-\tau}$, supporting the concept that clasts cool through conduction during stage 2. I fit conduction model solutions on a sphere (black line) to the experimental measurements to estimate Biot numbers and heat transfer coefficients. See Table 3.1 for a list of fitted Bi and H values. 43

3.9 Stage 2 saturation of clast ML01. Submerged weight increases linearly as temperature declines during stage 2. The linear relationships between submerged weight and temperature indicate that the clast saturates as thermal contraction draws in liquid water during stage 2. I propose that $\frac{\Delta M_S}{\Delta T_r}$ increases with trapped gas content and use Equation 3.15 to solve for trapped gas content, g_f. I find that trapped gas content generally decreases as clast initial temperature increases. . . 45

3.10 High-to-low liquid flux transition, t^*, as a function of clast initial thermal energy and surface area. Consistent with the concept that clasts must lose a sufficient amount of thermal energy to condense all internal steam and reach t^*, the linear relationship indicates that clasts experience the same time-integrated average rate of heat loss, $q = 7.5 \pm 0.5$ W cm^{-2}. 47

3.11 Observed time-averaged liquid flux versus modeled time-averaged liquid flux (Equation 3.17). I propose that, because model Q_l predictions match observed values, that I can use Equation 3.17 to estimate average rates of liquid flow into clasts and where liquid flow balances steam condensation. The line is 1:1. 49

3.12 Time for a clast to reach neutral buoyancy (dashed lines) and time to rise to the ocean surface from 1000 meter depth (solid lines) as functions of clast size and porosity. We model clast saturation as a function of heat loss and steam condensation (Equations 3.17−3.19). We estimate clast rise times using Equation (3.19−3.21). From this figure, we can estimate how long a water-vapor filled clast will remain buoyant (excluding the effects of decompression and vapor expansion) and minimum clast sizes required to reach the surface (intercepts of dashed and solid lines). Porosities are listed in percent. 51

3.13 Comparison between pumice cooling in water versus air. Representative clast ML02 cools faster in water compared to air. I also plot ΔM_S that corresponds to the temperature measurements taken in water. 60

3.14 Cooling and saturation of clast Pum06 in water. I observe an inflection point in internal temperature when $T = 100°$C. 61

3.15 Effects of initial temperature on cooling and saturation. (A) Internal temperature of clast ML02 as a function of time. (B) Liquid flux (g s^{-1}) into the clasts as a function of time. Clasts with initial temperatures below 100°C exhibit the lowest liquid fluxes. Otherwise, initial liquid flux decreases with increasing initial clast temperature. All clasts with initial temperatures above 100°C exhibit sharp high-to-low liquid flux transitions (marked with stars). The inset shows how the timing of the high-to-low liquid flux transition increases with clast initial temperature. 62

3.16 Pyroclasts used in this study 63

4.1 Mechanisms of gas trapping. Illustrations of gas trapping by (a) bypass and (b) snap-off trapping in pumice with connected pores. In both cases capillary forces draw water into pores such that water completely surrounds the gas phase and the gas is unable to escape. 67

4.2 X-ray microtomography images. 2D slices through μXRT images of pumice containing water and trapped gas. While hot pumice (SM04 and SM05) contain trapped gas, they hold smaller volume percentages compared to ambient temperature pumice. Contacts between rock, liquid, and gas demonstrate that the liquid is the wetting fluid (see red box). While glass walls are too thin to resolve in places (particularly in SM02 and SM05), we do not see any evidence in the μXRT that the thin glass walls in pumice are broken or damaged due to cleaning in an ultrasonic bath. (For interpretation of the references to color in this figure legend, the reader is referred to the web version of this article.) 71

4.3 Shapes of trapped gas bubbles. 3D μXRT images of trapped gas bubbles within pumice. Colors in this figure are chosen at random to identify separate gas bubbles. The top rows show the largest gas bubbles and the bottom row shows all gas bubbles within a single pumice. A single interconnected gas bubbles extends throughout many pores in pumice SM01. (For interpretation of the references to color in this figure legend, the reader is referred to the web version of this article.) 72

4.4 Bubble and vesicle size distributions. Trapped gas bubbles, locations where only the gas is present, are shown in black, and vesicles, pumice pores that can be filled with liquid or gas, are in grey. At least a third of the trapped gas is contained with a single large bubble for most of samples. The existence of large trapped bubbles, in combination with the vesicle size distribution, demonstrates that at least the largest gas clusters often extend through multiple pores. Bubbles and vesicles are binned into fifty logarithmically spaced bins and each bin is divided by the total volume of air or vesicles. Volume fraction is not weighted by bin width such that the sum of all bins equals one. 73

4.5 Power-law fits of bubble-size distributions. Measured distributions of trapped bubble volume (grey circles) and the fitted power-law distributions (dashed lines). The y-axis shows the probability that a bubble is larger than a given volume, V. With the exception of ML02, the fitted power-law coefficients, β, are consistent with the value predicted from percolation theory, $\beta = 2.19$. Because our machine learning segmentation method generated very small (artifact) bubbles, we removed bubbles smaller than 10^6 mm^3 before fitting a power-law coefficient. . . 74

4.6 Floatation time as a function of pumice volume. Measurements of pumice floatation from this study, [70], [141], [115], and [142]. Pumice floatation time predictions from this study (Equation 4.6) and [82] are also shown. Measured floatation times fit the trend predicted by Equation 4.6 (grey bar). Filled symbols represent measured sinking times while open symbols represent projected sinking times. . 76

4.7 Floatation time as a function of clast size, porosity and initial saturation. We plot solutions to Equations 4.14 and 4.15 to demonstrate how floatation time varies with pumice size, porosity, and initial gas saturation, ξ_i. We assume $\rho_r = 2.4$ g cm^3, $\rho_l = 1.0$ g cm^3, and sum the first ten terms of Equation (14). 78

5.1 Channel erosion by a Februrary 2017 debris flow. The debris flow removed overlying sediment and scoured at least 10 cm into shale bedrock. Debris flow scouring in this channel continued for 100s of meters downstream of this photo. One can see boulder and fine-sediment deposits from a debris flow that entered the channel on the right side of the figure. 84

List of Tables

2.1 Splash Function study comparison. N is the number of experiments for a given set of input parameters 12
2.2 p value model fit comparisons. A combination of d_c and V_i provides the p value closest to 1 and the best model fit 24
2.3 Notation 26

3.1 Pumice clast characteristics: characteristic radius, r_o, is estimated by assuming a spherical geometry and * refers to values calculated by assuming porosities (70% for Pum08 and 80% for HRaft01). n refers to the number of experiments conducted on each clast. $\frac{r_t}{r_o}$ refers to the thermocouple position relative to clast radius, $\frac{r_t}{r_o} = 1$ implies that the thermocouple is at the center of the clast. Uncertainties are calculated as the standard deviation of a set of measurements. We do not report uncertainties where only one measurement was made or if multiple measurements report the same values. 31
3.2 Cooling and saturation stages 34
3.3 Notation 55
3.4 Description of Experiments 59

4.1 While μXRT analysis is done on subvolumes of larger clasts, we expect the subvolumes to be representative of the larger pumice in part because the pumice are relatively small (i.e., < 1 g). Furthermore, the selected pumice samples do not have bread crust textures such that we expect differences between rim an internal porosities to be minimal. 70
4.2 Floatation time measurements for Santa Maria pumice 80

Acknowledgments

I would like to first thank my advisor, Michael Manga, for showing me new ways of thinking and for guiding me through the unique and inspiring journey that is graduate school. I admire Michael's willingness to lead by example and ability to provide insightful (and very rapid) feedback. Michael afforded me a great number of scientific opportunities while also providing the academic freedom to explore.

I would like to thank Bill Dietrich for investing in me and our field site in Colusa County. Bill Dietrich introduced me to geomorphology and encouraged me to tackle challenging science questions during my first year at Berkeley. Those initial questions led us to establish a new field site and the development of that site has been possible, in part, because of Bill's ambition and continued support. I am grateful for Bill's time, energy, and his patience as I balanced different research projects.

I also want to thank my committee members, Laurel Larsen and Roland Burgmann, for their encouragement, advice, and for making the qualifying exam challenging and rewarding.

The 2015 Mapping Exploration and Sampling at Havre (MESH) research cruise was a formative part of my PhD experience. I want to thank all the MESH cruise participants for teaching me about volcano science and acknowledge Rebecca Carey, Adam Soule, and James White in particular. I am grateful to Ben Andrews for his generosity of time and for opening up his pyroclastic density current laboratory facility to me. I want to thank Jean Braun for teaching me about landscape evolution and generously sharing his FastScape model. Mong-Han Huang has been an important friend and collaborator at Berkeley. I am grateful to him and our other Leesville Hills collaborators, Daniella Rempe, Alex Bryk, Behnaz Hosseini, and Mariel Nelson as well as the ranch owners, Rhonda Gruber, Greg Hemmi, Jerry Brown, and Anne Gust-Brown, for making our field study possible. I have also been fortunate to work with a number of talented and motivated undergraduate students, in particular: Michael Chamberlain, Zihan Wei, Christina Lin, and Berenice Gonzalez. I want to thank Alan Rempel and Kathy Cashman for the support and guidance they have provided on my career path.

My time at Berkeley has been shaped by the students and postdocs here and I am grateful for their passion, inspiration, and friendships. In particular I want to acknowledge: Marissa Tremblay, Chelsea Willett, Elizabeth Mitnick, Barbara Tripoli, Doug Hemmingway, Jesse Hahm, Tushar Mittal, Carolina Munoz-Saez, Steve Breen, Seth Saltiel, Jill Marshall, Elizabeth Niespolo, Courtney Sprain, and Ben Black. My friends from UC Davis have also remained an important source of support and fun: Judy Wexler, Diane Moug, Rachel Kerwin, and Danielle Haulman.

Michael Brunelle has provided perspective and balance on a daily basis and I am grateful for his support and patience. Finally, I want to thank my father, Tom Fauria, for showing me how to be curious and fun-loving and my mother, Charlene Fauria, for modeling how to be compassionate and ambitious.

Chapter 1

Introduction

Volcanic flows are complex, hot, and involve multiple phases such as gases and particles. As a result, answering fundamental questions about their behavior can be challenging. Active research questions include: What processes drive volcanic flows? What processes make flows stop? Can the speed and travel distance of volcanic flows be forecast? These questions are important because they both inform our understanding of volcanic hazards and help us to interpret the geologic record. The focus of this dissertation is on the use and development of physical models that, at least partially, address the above questions and increase our understanding of the processes that govern volcanic flows. I specifically examine the dynamics of dilute pyroclastic density currents and the products of submarine eruptions.

Pyroclastic density currents (PDCs) are fast-moving, turbulent mixtures of rock and gas that can travel over water, traverse barriers hundreds of meters high [e.g., 1–3], and runout hundreds of kilometers. Their high mobility makes them especially hazardous and, at times, unpredictable. PDCs are common and flows have been generated in just this year at dozens of volcanoes (e.g., at Sinabung Volcano, Indonesia and Colima Volcano, Mexico). At the time of writing, the potential for PDCs at Agung Volcano, Bali resulted in the evacuation of more than 133,000 people from a 6 km exclusion zone around the volcano (Smithsonian GVP, 2017).

Many aspects of PDCs are already understood. We know that they form due to the gravitational collapse of eruption columns or volcanic domes and that they are driven by their density difference with the atmosphere [4]. We know that PDCs can stop due to friction and energy dissipation, because their particles settle out, or because they entrain and heat enough air to become buoyant and form a plume [e.g., 5]. At the same time, it is still difficult to predict where PDCs will go in part because the distance PDCs travel is influenced by how much air they entrain, how much mass they lose by sedimentation, and how much mass they gain through substrate erosion - and these processes are not well quantified or understood.

In chapter 2 I use laboratory experiments to understand the small-scale processes that influence large-scale PDC behavior, specifically particle entrainment. From these experiments I develop process-based models of PDC dynamics that can be used to understand how particle entrainment affect runout distance. This chapter touches on research priorities identified by the volcano science community including how " particle-scale processes influence the large-scale dynamics of ... pyroclastic density currents ... [and] the role of evolving substrates in controlling flow dynamics" [6].

The submarine realm is a relatively new frontier in volcano science, in part because submarine volcanoes are difficult to observe. To date, only two submarine explosive eruptions have been directly witnessed [7–9] and mid-ocean ridge eruptions have only been seen with seismic data [10]. At the same time, up to 85 percent of volcanism occurs under water [11] and "expanding the study of submarine volcanism ... [is central to] overcome[ing] our biased understanding of the spectrum of volcanic eruptions" [6].

In 2015 I was fortunate to participate in an NSF-sponsored research cruise to map and sample submarine deposits from the 2012 eruption of Havre submarine volcano, the largest known pyroclastic submarine eruption in modern history [12, 13]. On the Mapping Exploration and Sampling at Havre (MESH) research cruise we found that most, but not all, of the volcanic material from the large 2012 eruption (> 1 km^3) was partitioned into a pumice raft rather than the submarine deposit [14]. Our observations raised questions about how pyroclasts are sorted during submarine eruptions, in particular: what processes control the dispersal of pyroclasts in the submarine environment and why do some pyroclasts float for years in pumice rafts while others sink to the seafloor?

To begin to address these questions, I have conducted laboratory experiments to understand the behavior of pyroclasts in water. In chapter 3, I examine and develop models for pumice cooling and saturation in water. Pyroclast cooling and saturation are important because they govern clast buoyancy and thereby control dispersal dynamics. In chapter 4, I examine why pumice can float in rafts for years and why pumice eventually sink, again using experiments to inspire new process-based models.

Together this dissertation provides insights into how volcanic products are dispersed in the ocean and across Earth's surface. I use experiments as a central tool to examine small-scale behavior and to inspire testable physical models. The new models presented here help us understand how far dilute pyroclastic density currents travel, how quickly pyroclasts cool, saturate, and thus rise to the ocean surface, and why pumice can remain afloat in rafts for months to years.

Chapter 2

Effect of particle entrainment on the runout of pyroclastic density currents

This chapter was previously published in Fauria, K.E., Manga, M., and Chamberlain, M., *Journal of Geophysical Research: Solid Earth* **121**, (2016). doi:10.1002/2016JB013263

2.1 Summary

Pyroclastic density currents (PDCs) can erode soil and bedrock, yet we currently lack a mechanistic understanding of particle entrainment that can be incorporated into models and used to understand how PDC bulking affects runout. Here we quantify how particle splash, the ejection of particles due to impact by a projectile, entrains particles into dilute PDCs. We use scaled laboratory experiments to measure the mass of sand ejected by impacts of pumice, wood, and nylon spheres. We then derive an expression for particle splash that we validate with our experimental results as well as results from seven other studies. We find that the number of ejected particles scales with the kinetic energy of the impactor and the depth of the crater generated by the impactor. Last, we use a one-dimensional model of a dilute, compressible density current where runout distance is controlled by air entrainment and particle exchange with the substrate to examine how particle entrainment by splash affects PDC density and runout. Splash-driven particle entrainment can increase the runout distance of dilute PDCs by an order of magnitude. Furthermore, the temperature of entrained particles greatly affects runout and PDCs that entrain ambient temperature particles runout farther than those that entrain hot particles. Particle entrainment by splash therefore not only increases the runout of dilute PDCs but demonstrates that the temperature and composition of the lower boundary have consequences for PDC density, temperature, runout, hazards and depositional record.

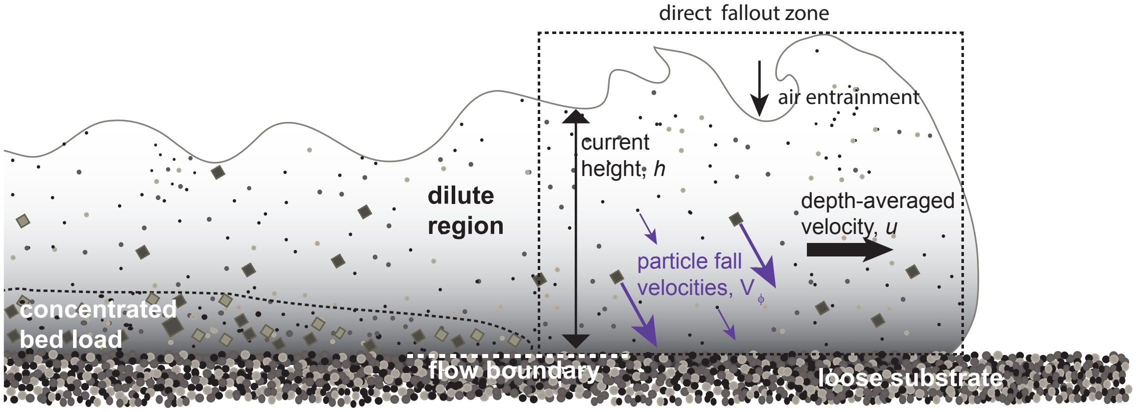

Figure 2.1: Conceptual model of a pyroclastic density current that can entrain loose substrate particles by particle splash. We hypothesize that splash-driven entrainment occurs in dilute regions of the current where the lower boundary of the flow lacks a bed load region and is dominated by particle fallout.

2.2 Introduction

Pyroclastic density currents (PDCs) are complex multi-phase flows governed by mass, momentum, and energy conservation. As a result, any process that adds or subtracts substantial mass, momentum, or energy may be important for PDC dynamics. For example, entrainment of ambient air increases PDC mass yet its thermal expansion lowers mean PDC density [e.g., 15, 16]. When PDC density becomes less than ambient air, the PDC rises buoyantly into the atmosphere - or liftoff. PDC mass, momentum, and energy are also affected by particle exchange with the substrate. For example, sedimentation lowers PDC density and kinetic and thermal energy [4, 17, 18], can stop PDC runout [5, 19, 20] and is the process that controls the geologic record of PDCs.

PDCs can also transfer particles from the bed into the current [e.g., 4, 17]. This process - particle entrainment, the erosion and incorporation of bed material - may also affect PDC dynamics. We currently lack, however, a process based understanding of "erosion and bulking of currents during transport" that is needed "to simulate the full range of pyroclastic density current behaviors" [5]. While understanding substrate entrainment remains a scientific challenge in general [21], erosion by PDCs is well documented through observations of depositional unconformities [4, 22–25], erosional furrows [26, 27], the removal of scree or topsoil [24, 27–29], lithics and transported blocks within ignimbrites [25, 27, 30–33], striations against bedrock [27, 29], and the creation or deepening of channels and gullys [25, 28].

Recent progress has been made towards connecting observations of erosion with a mechanistic understanding of entrainment processes. These studies have focussed on granular flows and the dense PDC end-member [34–36]. Yet the processes that occur at the base of dilute PDCs (e.g., particle rebound and steam generation) are also known to greatly affect PDC dynamics [18, 37]. We therefore turn to the dilute PDC end-member and ask: (1) How can we mechanistically quantify entrainment? (2) How does particle entrainment affect PDC runout distance? and (3) What entrainment and resuspension processes are important in dilute PDCs?

The lower boundary of dilute PDCs is often conceptualized as a direct fallout zone where sedimenting particles fall onto the underlying substrate or dense undercurrent [e.g., 4]. In this setting, we hypothesize that the impact of falling particles against the lower boundary can eject other particles into the current. We test this idea with laboratory experiments and validate an expression for impact-driven particle entrainment. We then use a 1D model of a dilute PDC to explore how particle entrainment - as parameterized by an expression for particle "splash"- affects dilute PDC density, temperature, and runout distance. We find that particle entrainment can significantly increase PDC runout distance.

2.3 Conceptual Model of Dilute Pyroclastic Density Currents

Pyroclastic density currents are hot and turbulent mixtures of rock and gas that propagate because of their density difference with air. There are two common end-member models for PDCs (Figure 2.1): (1) concentrated currents where friction dominates; and (2) dilute currents where there are few particle-particle interactions [e.g., 4, 5]. Here we study particle entrainment processes relevant to the dilute end-member where individual particles settle through the current and onto the base of the flow (Figure 2.1). Furthermore, we model the flow boundary as a direct fallout zone where there is a sharp velocity, rheological, and particle concentration gradient between the flow and substrate surface [4]. Our conceptual model, and later our numerical model, therefore requires that dense bed load regions are absent. Because concentrated bed load regions often lag behind the dilute head [38], this assumption applies best at the front of PDCs (Figure 2.1) where the majority of entrainment occurs for at least some flows [39].

PDCs can pass over many different types of surfaces such as rock, water, recent PDC deposits, soil, or vegetation. The composition of this substrate will determine which processes occur at the lower PDC boundary and can thereby affect large-scale PDC dynamics. For example, [18] quantified the amount of steam generated by pyroclasts as PDCs flow over water and found that steam generation can initiate littoral blasts. [37] compared two types of PDC boundariesone that falling particles pass through and one that particles rebound fromand found that particle rebound increased small particle concentration and the transport distance of large clasts.

We consider the case where a dilute PDC passes over loose, unconsolidated soil or PDC deposit (Figure 2.1). Because active volcanoes can generate multiple PDCs on the decadal timescale, PDCs commonly pass over ash and lapilli. When particles within dilute PDCs hit loose substrate,we hypothesize that the particle impacts can eject substrate particles into the current. In the next section we quantify this process at the particle scale and later introduce particle entrainment into a one-dimensional PDC model.

2.4 Particle splash experiments

Impact driven particle entrainment, or splash, refers to the ejection of unconsolidated particles from a surface because of impact by a projectile (Figure 2.2a). While we hypothesize that splash is important within dilute PDCs, this process has been studied in other contexts - particularly with respect to aeolian transport [e.g., 40–43]. Splash Functions are mathematical expressions that describe this process, and many empirical, theoretical, and numerical studies have been undertaken to derive and validate Splash Functions (Section 2.10.1). In general, these studies agree that $N_e \propto V_i^n$, where N_e is the number of ejected particles, V_i is the impactor velocity, and n is a coefficient that is typically about 2, consistent with ejection scaling with kinetic energy.

2.4.1 Experimental and Splash Function scaling

In the next section we present splash experiments with velocities and particle sizes relevant to dilute PDCs. These experiments will allow us to validate a new Splash Function, an expression of the scaling between ejected particle mass and impactor and substrate properties, across this PDC appropriate parameter space. Specifically, we will measure the mass of sand ejected by pumice lapilli impacts. We choose loose, dry sand because of its similarity (size, packing, and texture) to pyroclastic surge deposits [e.g., 44] and tendency to settle quickly. We choose pumice lapilli as a direct analog to falling pyroclasts in dilute PDCs.

Previous studies have conducted splash experiments with 0.2 - 20 mm diameter particles, 0.25-60 m s^{-1} velocities, and impacting and ejected particles with the same diameters (Table 1). We will also test our Splash Function with data from these seven studies. As long as the same processes (e.g., transfer of kinetic to potential energy) control particle splash, our Splash Function, if valid, should apply to this extended parameter range. We note, howver, that no experiments have measured particle splash when a small particle impacts a bed of larger particles. Any Splash Function extrapolation to this scenario, or far beyond the parameter space shown in Table (2.5.1), is therefore unvalidated.

2.4.2 Experimental Methods

We used laboratory experiments to measure the mass of sand ejected during impact by a projectile. To create impacts, we propelled 1.2 cm diameter particles with compressed air

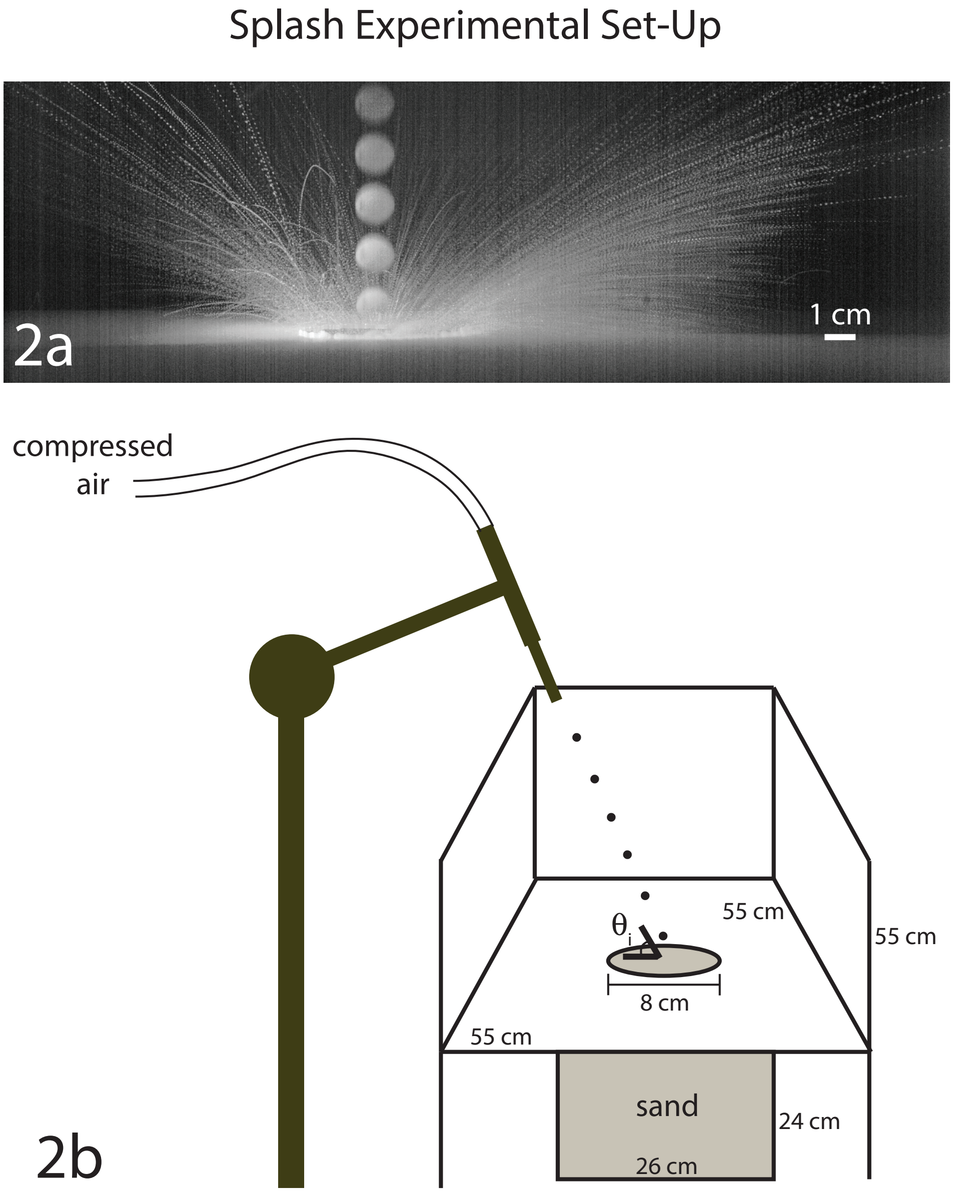

Figure 2.2: (a) A composite image (100 frames recorded at 600 fps) of a nylon sphere impacting sand and the resultant particle splash. (b) A schematic diagram of our experimental setup. The diameter of the hole in the stiff paper is 8 cm. The high-speed camera was in the foreground.

into dry sand. In these experiments we varied impactor type (natural pumice clasts, nylon spheres, wood spheres) and density (0.88 - 1.25 g cm^{-3}), impactor speed (5 - 65 m s^{-1}), and impact angle (40 - 90°). We conducted sixty-one total experiments and we did not vary the type of material in the substrate (0.56 mm diameter loosely packed sand).

During the experiments we measured the impactor velocity immediately prior to impact with a high speed camera at 1000 frames per second (fps). We estimated the uncertainty of the velocity measurements to be 2 pixels/frame x 1000 fps x 1 cm/20 pixels = 1 m s^{-1} [45]. We set the impact angle by rotating the arm of the compressed air blaster (Figure 2.1b). A 26 x 26 x 24 cm container (large enough to avoid edge effects) held the sand and we stirred the sand such that it was loosely packed before each experiment. To measure the total mass of suspended particles, we placed stiff paper 1 mm above the sand surface. The paper contained an 8 cm diameter hole to allow for particle escape; we fired the projectile into the center of this hole such that the majority of suspended material landed on the paper (Figure 2.2). Vertical walls blocked high-velocity ejected particles from traveling off the edge of the collection paper (Figure 2.2). After each experiment, we collected and weighted the sand. If the projectile rebounded upon impact, the rebound velocity was measured with the high speed camera. As did [37], we found that the impactor rebounded more often at shallow incidence angles, θ_i, and only when $\theta_i \leq 70°$. Rebound occurred during relatively few experiments.

Our methods for measuring suspended particle mass underestimated suspended mass for several reasons. First, suspended particles that landed within the 8 cm diameter hole were not collected. Furthermore, particles that would have been ejected from locations outside the hole opening were not able to escape. Lastly, particles that were ejected towards the camera were not caught on the paper.

2.4.3 Experimental results

Figure 2.3 shows experimental measurements of the ratio of ejected to projectile mass versus a dimensionless ratio of kinetic to potential energy. We found that the total suspended mass increased with the square of the impact velocity and that the ejected mass generally exceeded the mass of the impactor. Pumice (0.99 and 1.25 g cm^{-3}) ejected, in general, more particles than the wood spheres (0.88 g cm^{-3}) of similar impact speeds. We hypothesize that this is because pumice has a rough and irregular surface that can grab and eject more sand than smoother spheres.

We compare our experimental results to several previously published Splash Functions in Section 2.10.1. The fits to all these functions are unsatisfactory (Figures 2.9). Many of the existing expressions are off by several orders of magnitude. We also test our experimental results against Splash Functions where $N_e \propto (V_i \sin\theta_i)^2$ and $N_e \propto V_i^2$, where θ_i is the incidence angle of the impactor (Figure 2.1b, Section 2.10.2). Section 2.10.2 shows that we find better fits when V_i is used instead of $V_i \sin\theta_i$. In the next section we derive a new Splash Function that we compare to our experimental results as well as measurements from seven other studies.

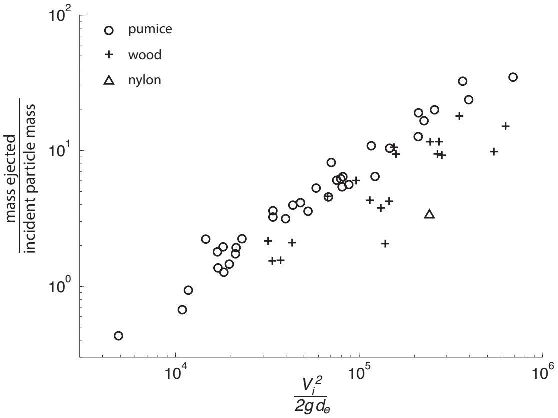

Figure 2.3: Experimental measurements of ejected mass over the mass of the incident particle, m_i, plotted against a dimensionless ratio of kinetic to potential energy. Our experimental results demonstrate that $\frac{N_e m_e}{m_i}$ increases with V_i^2 and that impacts can suspend masses greater than the incident particle mass (i.e., $\frac{N_e m_e}{m_i} > 1$). Wood spheres eject less mass than pumice for a given kinetic energy.

2.5 Splash Function

We derive a new Splash Function based on a conversion of kinetic energy to potential energy. While other Splash Functions have been derived based on energy conservation [e.g., 40, 46–48], we allow impacting and ejected particles to have different sizes and densities.

Consider an impacting particle with kinetic energy $\frac{1}{2}m_i V_i^2$, where m_i is the mass of the impactor, and V_i is the impactor velocity. During a collision the kinetic energy of the impacting particle (1) contributes to the plastic and elastic deformation of both the impactor and the substrate, (2) is dissipated by friction in between particles, (3) is retained by the impacting particle and results in particle rebound, and (4) is transferred to the substrate and results in particle ejection. We write the conversion of kinetic energy of the impactor to potential energy of the substrate as,

$$e_n^2 \frac{1}{2} m_i V_i^2 = N_e m_e g L, \tag{2.1}$$

where $0 < e_n < 1$ is a restitution coefficient that characterizes the kinetic energy fraction transferred to the ejected particles (energy lost from processes 1-3), m_e is the mass of each suspended particle, g is gravity, L is a characteristic length scale of suspension, and N_e is the number of ejected particles.

The diameter of the ejected particles, d_e, has been used as the characteristic length scale in other Splash Functions [41, 46–48]. However, [49] demonstrated that the number of suspended particles does not scale linearly with V_i^2. We propose that the relevant length

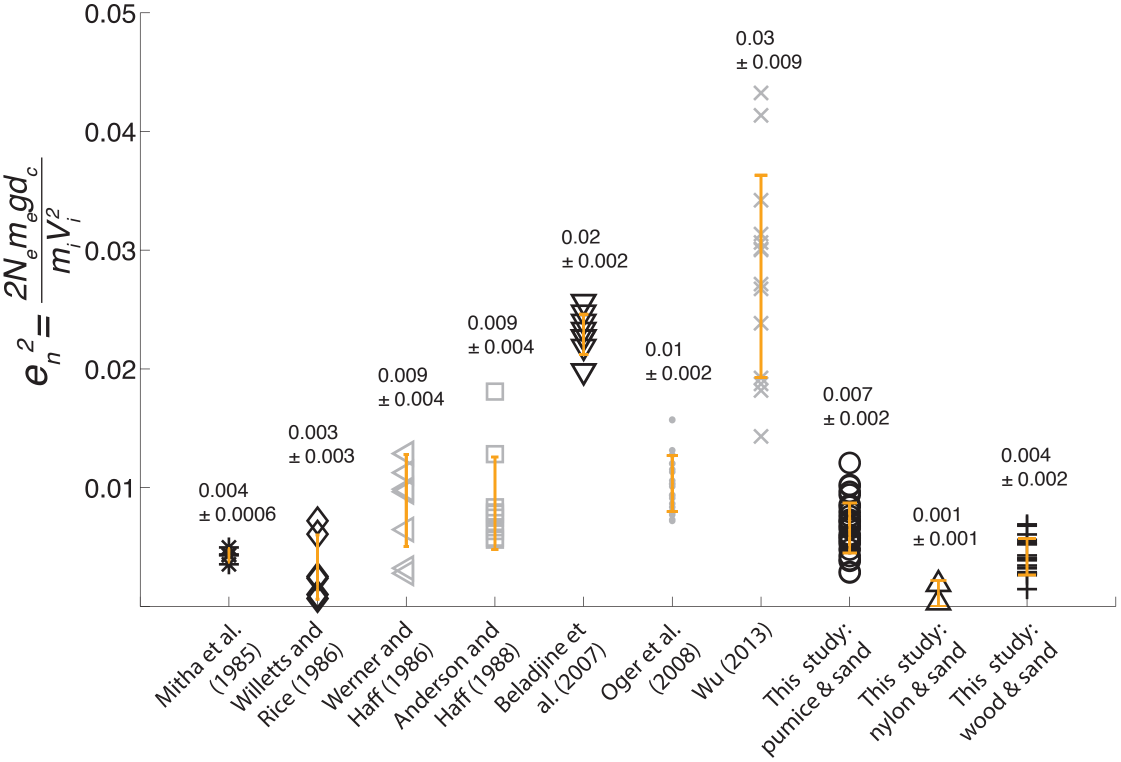

Figure 2.4: Measurements of particle splash from eight studies are plotted to solve for a mean restitution coefficient, e_n^2, which represents the fraction of energy retained during impact. The orange bars show the mean and standard deviation of the restitution coefficient for each study. For most studies, restitution coefficients fall within a small range. This demonstrates that the restitution coefficient is fairly constant for the range of materials, impact velocities, and angles used in each study. It is not surprising that e_n^2 varies between studies because different materials were used. Black symbols represent data from physical experiments, and gray symbols represent data from discrete element model (DEM) simulations.

scale for particle suspension is the depth of the crater that is formed during impact. While there many expressions for crater depth in dry granular media we use,

$$d_c = 0.14\mu^{-1}\sqrt{\frac{\rho_i}{\rho_e}}d_i^{\frac{2}{3}}h_i^{\frac{1}{3}}, \tag{2.2}$$

where μ is the tangent of the friction angle, ρ_i is the impactor density, ρ_e is the ejected particle density, d_i is the impactor diameter, and h_i is the height from which the impactor is dropped [50]. h_i can be related to V_i according to $h_i = \frac{V_i^2}{2g}$. We thereby propose a new Splash Function,

$$N_e = \frac{\frac{1}{2}e_n^2 m_i V_i^2}{0.14 m_e g \mu^{-1}\sqrt{\frac{\rho_i}{\rho_e}}d_i^{\frac{2}{3}}(\frac{V_i^2}{2g})^{\frac{1}{3}}}, \tag{2.3}$$

where $N_e \propto V_i^{\frac{4}{3}}$.

2.5.1 Splash Function validation

We test Equation (2.3) by comparing N_e predicted (Equation 2.3) to N_e observed. To do this, we use our experimental measurements as well as measurements from seven other studies [46, 48, 49, 51–54]. These studies allow us to validate our Splash Function against impactor velocities of 0.25-65 m s^{-1}, particles sizes of 0.2-20 mm, and impactor to subsrate mass ratios of 1-5000 (Table 2.5.1).

Because each study used different physical materials or numerical parameters, we expect e_n^2 in Equation (2.3) to be different for each study. We solve for e_n^2 by rearranging Equation (2.3) and using values reported by each study for $\frac{m_i}{m_e}$, V_i, $\frac{\rho_i}{\rho_e}$, d_i, and N_e; we assume $\mu = 0.5$. If Equation (2.3) is valid, e_n^2 should have a relatively constant value for each study. Figure 2.4 shows that each study reports a different restitution coefficient with small standard deviations. This suggests that Equation (2.3) fits the experimental data well.

We rearrange Equation (2.3) and plot $\frac{e_n^2 m_i V_i^2}{m_e}$ versus $2gN_e d_c$, using the e_n^2 values given in Figure 2.4 and where the other parameters were reported by each study (Figure 2.5). Figure 2.5 shows that Equation (2.3) matches observations of particle splash across a wide parameter range. Because fall velocities and particle sizes in dilute PDCs are generally within the parameter range for which equation (2.3) was validated, we feel confident that Equation (2.3) can be used in models of particle settling in dilute PDCs where the ejected particle is no larger than the impactor.

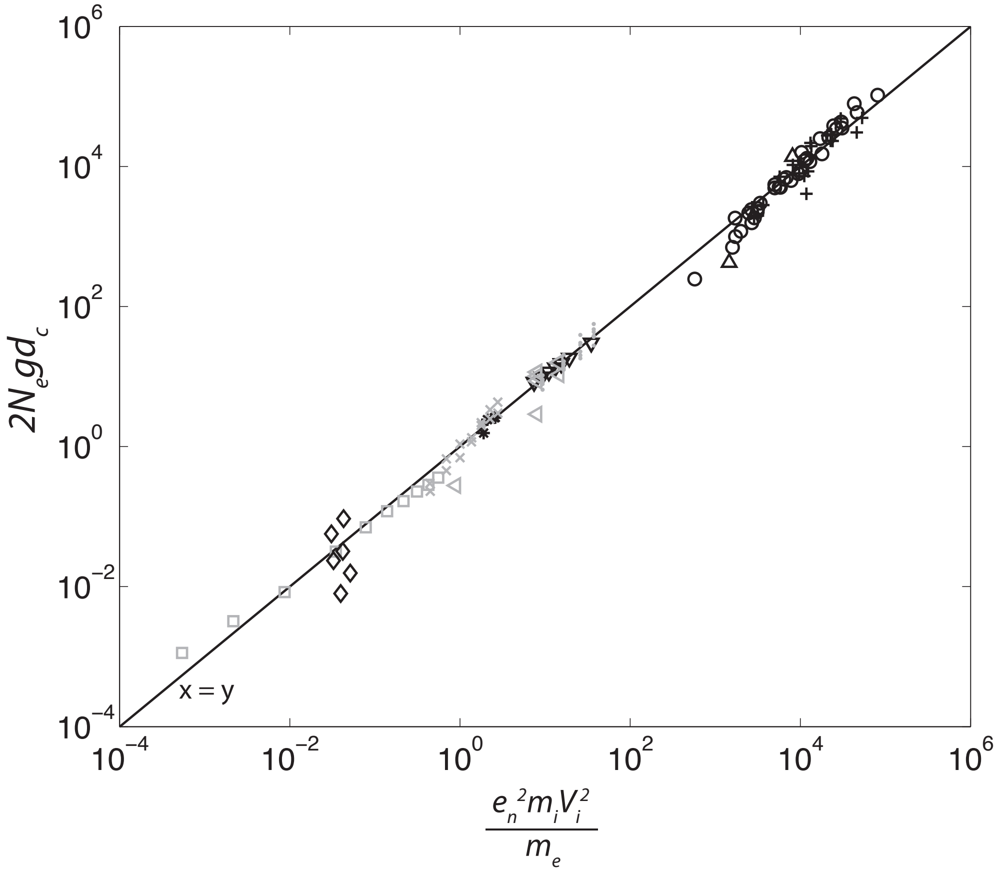

Figure 2.5: Equation (2.3) is tested by substituting measured values from eight studies into equation (2.3). Equation (2.3) holds (plots on a 1:1 line) across a large parameter space ($0.25 < V_i < 81$ m s^{1} and $0.02 < d_i < 2$ cm), suggesting that equation (2.3) is a valid Splash Function. Black symbols represent data from physical experiments, and gray symbols represent DEM simulations. The symbol shapes correspond to those in Figure 2.4.

study	method	impactor type and diameter	substrate type and diameter	$\frac{m_i}{m_e}$
Mitha et al. (1986)	experiments	4 mm steele BBs	4 mm steele BBs	1
Willetts and Rice (1986)	experiments	0.2 - 0.5 mm sand	0.2 - 0.5 mm sand	1
Werner and Haff (1986)	2D simulations	10; 20 mm	20 mm	0.25; 1
Anderson and Haff (1988)	2D simulations	1 mm	1 mm	1
Beladjine et al. (2007)	experiments	6 mm PVC plastic	6 mm PVC plastic	1
Oger et al. (2008)	2D and 3D simulations	6 mm	6 mm	1
Wu (2013)	3D simulations	0.3 mm	0.3 mm	1
This study	experiments	11 mm pumice, 12 mm wood, 13 mm nylon	0.56 mm sand	3600-5000

Table 2.1: Splash Function study comparison. N is the number of experiments for a given set of input parameters

2.6 One-dimensional model a dilute pyroclastic density current that entrains air and sediment

We examine PDC runout distance in a 1D model of a dilute (no frictional deceleration) and turbulent gravity current across a flat surface. A feature of this model is that we allow the fluid (air) in the PDC to be compressible such that thermal expansion of entrained air can change current density. We also model the effects of particle sedimentation and entrainment on PDC density. PDC density is critical to this model because we define runout distance as the location where the bulk current density is equal to the density of ambient air; this is where liftoff occurs. All quantities vary as a function of distance, x, travelled or equivalently as time, t. We do not explicitly highlight the spatial and temporal variability of the variables in the equations that follow.

Consider a dilute pyroclastic density current with three phases: an air phase with mass m_a [kg m^{-2}]; a small particle phase with mass m_{ϕ_1} [kg m^{-2}]; and a large particle phase with mass m_{ϕ_2} [kg m^{-2}]. Here mass, and later energy, are divided by the local basal area of the current, thus m is a bulk density multiplied by the current thickness. Let the initial temperature of the particles be T_i and the initial temperature of air in the current be the ambient temperature T_a. Furthermore, let us assume that heat transfer between air and particles is rapid such that the particles and air in the current rapidly obtain the mean PDC temperature [55]. The mean temperature of the PDC is

$$T_c = \frac{H}{C_p^a m_a + C_p^r (m_{\phi_1} + m_{\phi_2})}, \tag{2.4}$$

where C_p^a and C_p^r are the specific heat capacities of air and rock, respectively [J kg^{-1} K^{-1}], and H is the thermal energy in the current per unit area [J m^{-2}],

$$H = C_p^a T_a m_a + C_p^r T_i (m_{\phi_1} + m_{\phi_2}). \tag{2.5}$$

The height of the current, h, depends on the volume of air and particles in the current. We let air volume change due to thermal effects such that

$$h = \frac{m_a}{M}\frac{RT_c}{P} + \frac{m_{\phi_1}}{\rho_{\phi_1}} + \frac{m_{\phi_2}}{\rho_{\phi_2}}, \tag{2.6}$$

where M is the molar mass of air [kg mol^{-1}], R is the universal gas constant [J mol^{-1} K^{-1}], and P is pressure within the current [Pa], and ρ_{ϕ_1} and ρ_{ϕ_2} are the densities of the two particle size fractions [kg m^{-3}].Because the PDC is denser than the air in which it propagate, the pressure within the curent will be slightly higher than atmospheric. In the model, however, we assume that P is atmospheric pressure. The bulk density of the density current is thus

$$\rho_c = \frac{m_a + m_{\phi_1} + m_{\phi_2}}{h}. \tag{2.7}$$

We can now solve equations for conservation of mass, momentum, and energy in a current that entrains air, sediments particles, and entrains particles. Because turbulent gravity current motion across a flat surface is governed by a pressure gradient at the head of the current, momentum conservation can be written as [e.g., 20, 56]

$$u = \sqrt{2g'h}, \tag{2.8}$$

where Fr is Froude number (Fr $= \sqrt{2}$ when there is no energy loss, $g' = \frac{\rho_c - \rho_a}{\rho_a} g$, g is gravity, and h is the height of the current. Because fluid resistance causes energy loss, observed density current Froude numbers are generally slightly lower than $\sqrt{2}$, and we use Fr $= 1.2$ [57].

Mass within the current changes due to air entrainment, particle sedimentation, and particle entrainment. We write separate continuity equations for the air and particle fractions of the current. The continuity equation for air is

$$\frac{dm_a}{dt} = Eu\rho_a, \tag{2.9}$$

where E is the entrainment rate of air into the current, and ρ_a is the density of air at T_a. The right hand side of Equation (2.9) dictates that the mass of air in a PDC changes due to air entrainment where the velocity of air entering the current normal to the entraining edge is Eu. The continuity equations for the two particle size fractions are

$$\frac{dm_{\phi_1}}{dt} = \underbrace{\frac{-m_{\phi_1} V_{\phi_1}}{h}}_{settling} + \underbrace{\beta V_{\phi_1}^{4/3}}_{splash\ from\ m_{\phi_1}} + \underbrace{\beta V_{\phi_2}^{4/3}}_{splash\ from\ m_{\phi_2}}, \tag{2.10}$$

$$\frac{dm_{\phi_2}}{dt} = \underbrace{\frac{-m_{\phi_2} V_{\phi_2}}{h}}_{settling}, \tag{2.11}$$

where V_{ϕ_1} and V_{ϕ_2} are the settling velocities of the two particle size fractions, and $\beta = \frac{\frac{1}{2}e_n^2 m_i}{0.14 g\mu^{-1}\sqrt{\frac{\rho_i}{\rho_e}}\left(\frac{d_i^2}{2g}\right)^{\frac{1}{3}}}$, is a coefficient given by our Splash Function (Equation 2.3), and m_i is the total mass of the impactors, $\int \frac{m_\phi V_\phi}{h} dt$, for particle size fractions ϕ_1 and ϕ_2. The second and third expressions on the right hand side of Equation (2.10) show that we assume that the entrained particles have the same physical properties (size and density) as the small particle fraction. Furthermore, we assume that the settling particles are traveling at their terminal velocities when they settle from the current. We calculate settling velocities according to the framework presented by [37, Section 2.10.3].

Thermal energy within the current changes due to entrainment of air, entrainment of particles, and sedimentation of particles. We neglect the conversion of gravitational potential to heat and dissipation of kinetic energy to heat. We write conservation of thermal energy as,

$$\frac{dH}{dt} = \underbrace{\frac{dm_a}{dt}C_p^a T_a}_{airentrainment} - \underbrace{\Big(\frac{m_{\phi_2}V_{\phi_2}}{h} + \frac{m_{\phi_1}V_{\phi_1}}{h}\Big)C_p^r T_c}_{settling} + \underbrace{(\beta V_{\phi_1}^{4/3} + \beta V_{\phi_2}^{4/3})C_p^r T_e}_{splash}, \tag{2.12}$$

where T_e is the temperature of the particles entrained into the current. The first term on the right hand side of Equation (2.13) represents entrainment of ambient air into the current, the second term on the right hand side accounts for particle sedimentation, and the third term accounts for particle entrainment.

Equations (2.4 - 2.12) allow us determine the time, t_r, at which $\frac{\rho_c}{\rho_a} \leq 1$. Because $u = \frac{dx}{dt}$, runout distance L_r is,

$$L_r = \int_{t_o}^{t_r} u dt. \tag{2.13}$$

We use a first-order, forward-difference scheme to solve Equations (2.4) - (2.13) and determine runout distances for thermally expanding currents, noting that all quantities (m_a, m_{ϕ_1}, m_{ϕ_2}, T_c, H, h, ρ_c, u, V_{ϕ_1}, V_{ϕ_2})are functions of x and equivalently t. We compare runout distances for currents that don't sediment particles, sediment but don't entrain, and as well as entrain particles according to Equation (2.3). Furthermore, we vary the temperature of entrained particles, T_e.

2.6.1 1D PDC model results

We use the 1D model to explore how particle entrainment by splashing can affect PDC dynamics and runout distance. Figure 2.6 shows how density and temperature evolve in PDCs with different degrees of particle sedimentation and particle entrainment. For all model results plotted in Figure 2.6, $T_a = 20°C$, $T_i = 600°C$, and the initial values for m_a, m_{ϕ_1}, and m_{ϕ_2} are 30, 100, and 10 kg m^{-2}, respectively. The diameters and densities of the small and large particles are 0.1 and 10 mm and 2400 and 1000 kg respectively. We choose a small diameter for the small particle size fraction such that particles ejected into the current by splash can be assumed to be mixed within the current by turbulence. While particle settling velocities evolve as a function of PDC density and particle concentration (Section 2.10.1), the initial settling velocities for these two particle size fractions were 0.5 and 8.7 m s^{-1}, respectively. We let $E = 0.1$ [16] and the splash restitution coefficient equal the value we empirically determined for pumice impacting sand, $e_n^2 = 0.007$ (Figure 2.4). Cold particle entrainment refers to a PDC that entrains particles at temperature T_a while hot particle entrainment refers to entrainment of particles at the initial PDC mixture temperature.

Figure 2.6a shows how PDC densities evolve with distance. Density increases from 0 to 49 m for the current that entrains cold particles. Otherwise density decreases with distance for all the currents. The PDC that entrains cold particles has the highest density, followed by the current that entrains hot particles. This shows that particle splash can keep PDC

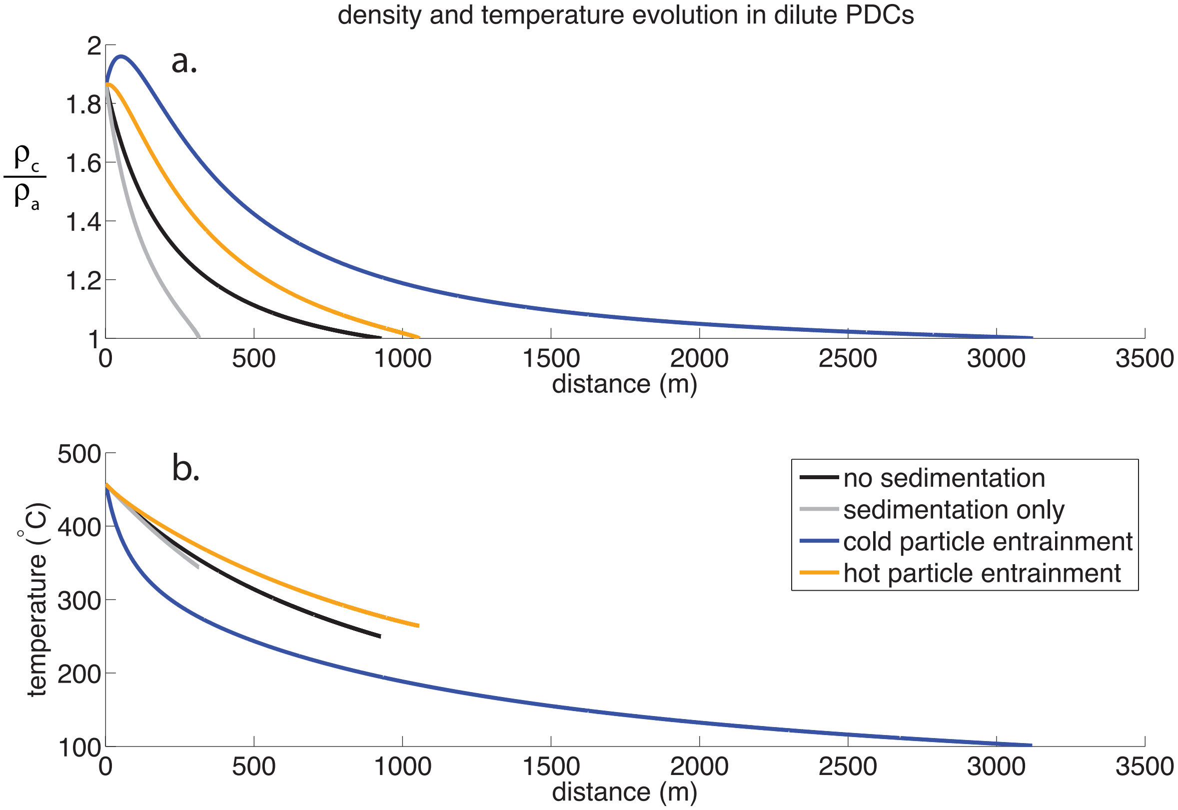

Figure 2.6: (a) Density and (b) temperature model results as a function of distance within currents with four different particle sedimentation and entrainment regimes. All currents had an initial particle temperature of 600°C and initial mean PDC temperature of 457°C. The PDC that entrains cold particles runs out the farthest and has the highest mean density and lowest internal temperature. The PDC that entrains hot particles runs out the second farthest and has the second highest mean density but maintains the highest internal temperature.

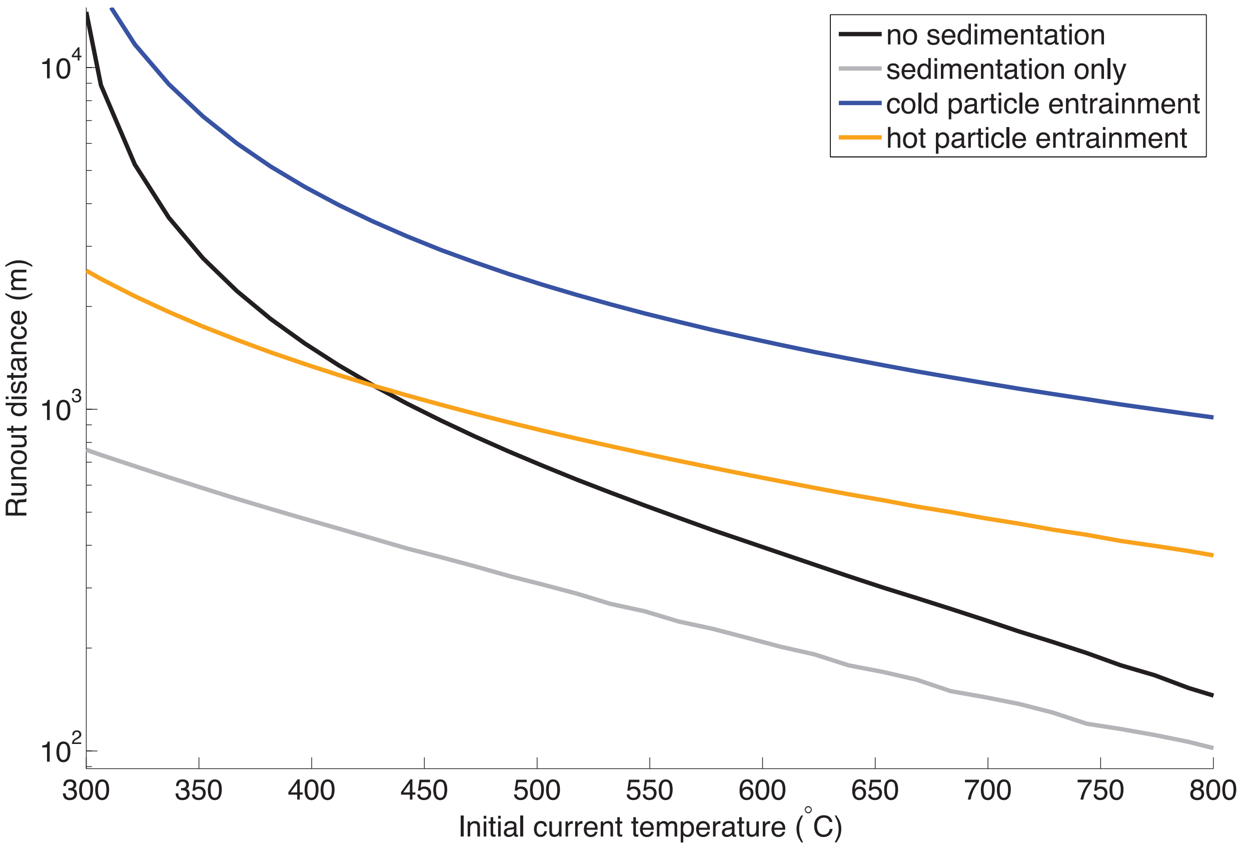

Figure 2.7: Runout distance model results. Runout decreases with initial temperature for all currents. The occurrence and temperature of particle entrainment have order of magnitude effects on runout distance. PDCs that entrain cold particles run out the farthest.

density elevated. Runout is shortest, and the density decline the steepest, for the current that sediments but does not entrain particles.

PDC mean temperature is plotted with distance in Figure 2.6b. Internal PDC temperature declines most rapidly for the PDC entraining cold particles. By comparison, PDC temperature remains the highest for the current entraining hot particles.

We examine the effects of entrainment on PDC runout distance over a range of initial mean PDC temperatures (Figure 2.7). Except for initial temperature (and therefore initial settling velocity), the parameters used in Figure 2.7 were the same as those listed for Figure 2.6. Runout distance is defined as the location where $\frac{\rho_c}{\rho_a} \leq 1$. Figure 2.7 shows that runout distance decreases with increasing initial PDC temperature. PDCs that do not sediment or entrain particles show the steepest decline in runout with temperature. This is because these currents have only one mechanism to lower density - the thermal expansion of entrained air, which is highly effective at high temperatures and less effective at low temperatures. By comparison, the sedimenting and sediment entraining currents can change density through particle exchange with the substrate.

It is useful to compare PDCs that entrain particles to PDCs that sediment, but do not entrain. Figure 2.7 shows that PDCs that entrain cold particles runout almost order of magnitude farther than PDCs that entrain hot particles, which runout a half an order of magnitude farther than PDCs that sediment only. This demonstrates that particle splash can be important for PDC runout distance and dynamics. We emphasize that splashed particle temperature is important - PDCs that entrain cold particles runout almost an order of magnitude farther than PDCs that entrain hot particles (Figure 2.7). Furthermore, the importance of sedimentation regime decreases with initial PDC temperature as thermal expansion becomes more important than sedimentation at high PDC initial temperatures.

2.7 Discussion

In section 1 we highlighted three open questions. We now address these in order, in light of our experiments and model results.

2.7.1 Quantification of particle entrainment

We quantified particle entrainment with a new splash function and found that the number of ejected particles scales with impact crater depth, equation (3). Unlike existing splash functions, we considered physical differences between the impactor and the ejected particles. We also demonstrated that our Splash Function applies across a broad parameter space and can describe the dynamics of sand or lapilli pumice impactors. Overall, splash can result in the net addition of particles to PDCs because the ejected mass can be greater than the projectile mass (Figure 2.2). In our model we assumed that splashed particles were fully mixed within the PDC and did not explicitly account for the splashed particle momentum flux. 3D multiphase models, however, could in principle consider the velocity distributions of ejected particles [e.g., 43].

2.7.2 The effect of particle entrainment on PDC runout distance

We used a 1D model to test the effects of particle splash on dilute PDC runout distance. We defined runout distance as the location where $\frac{\rho_c}{\rho_a} \leq 1$ and found that particle entrainment can increase runout by over an order of magnitude (Figure 2.7). This result implies that composition of the lower boundary of a PDC can have an important influence on runout distance. Where loose particles are available for splash, such as on a previous PDC deposit, PDCs may runout much farther because particle entrainment increases flow density. By comparison, if a particle source is not available - where the terrain is bedrock, water, or covered by vegetation - then splash driven particle entrainment is unlikely to occur and runout distances may be shorter.

The temperature of the entrained particles also greatly affects PDC runout distance and density evolution. This is because hot particles add more thermal energy to the flow and lower air density. Our results agree with those of [17] and imply that a dilute PDC overriding a hot substrate (such as a recent ignimbrite deposit) will not runout as far as one overriding a cold deposit.

We examined the effects of particle splash in the absence of a concentrated bed load region. It is possible, however, that dense basal layers of PDCs may inhibit particle splash by slowing falling particles and buggering the substrate. Indeed, entrainment mechanisms other than particle splash are likely inmportant in the bed load region (Roche et al., 2013a; Roche, 2015).

Particle splash, may however, provide a mechanism through which mass and momentum are exchanged between the dense and dilute regions of a PDC. While mobile bed loads are fundamentally different from static and concentrated granular substrates, we envisage that particles falling from the dilute region of a PDC onto a concentrated bed load region may be able to splash particles from the bed load into the dilute part of the a PDC. If splash on a granular flow is as efficient as splash on a static granular layer, then dilute PDCs overriding a hot and dense flow will have shorter runout distances than those on cold and static granular substrates.

The initial temperature of a PDC can greatly affect runout distance (Figure 2.6) NS air entrainment efficiency [58]. Air entrainment during collapse events has been invoked as the mechanism that cools PDCs to temperatures less than magmatic [e.g., 59]. Particle splash may be an additional mechanism for PDC cooling during or soon after PDC formation (Figure 2.5b). For that reason, models of PDC formation via collapse [e.g., 60] could examine how particle splash affects initial PDC temperature. Equally important, splash driven entrainment can be incorporated into 3D multiphase and multi-physics PDC simulations [e.g., 18, 58, 61–63] to test how entrainment affects not only runout, but concentration and concentration gradients, stratification, air entrainment, and thermal evolution within the flows. Three-dimensional multiphase models can also explore how particle splash modifies the momentum flux into the currents and examine how high bed load concentrations [e.g., 64, 65] affect the occurrence and efficiency of particle splash.

It would be interesting and informative to know how much of a PDC is comprised of primary versus entrained material. We do not report this kind of information in part because differentiating juvenile from entrained material is complex. Entrained particles can be lithics, part of older deposits, or can be sourced from recently deposited parts of the PDC itself. Individual particles may go through many cycles of deposition and resuspension before reaching their final fates in coignimbrite plumes or ignimbrite deposits.

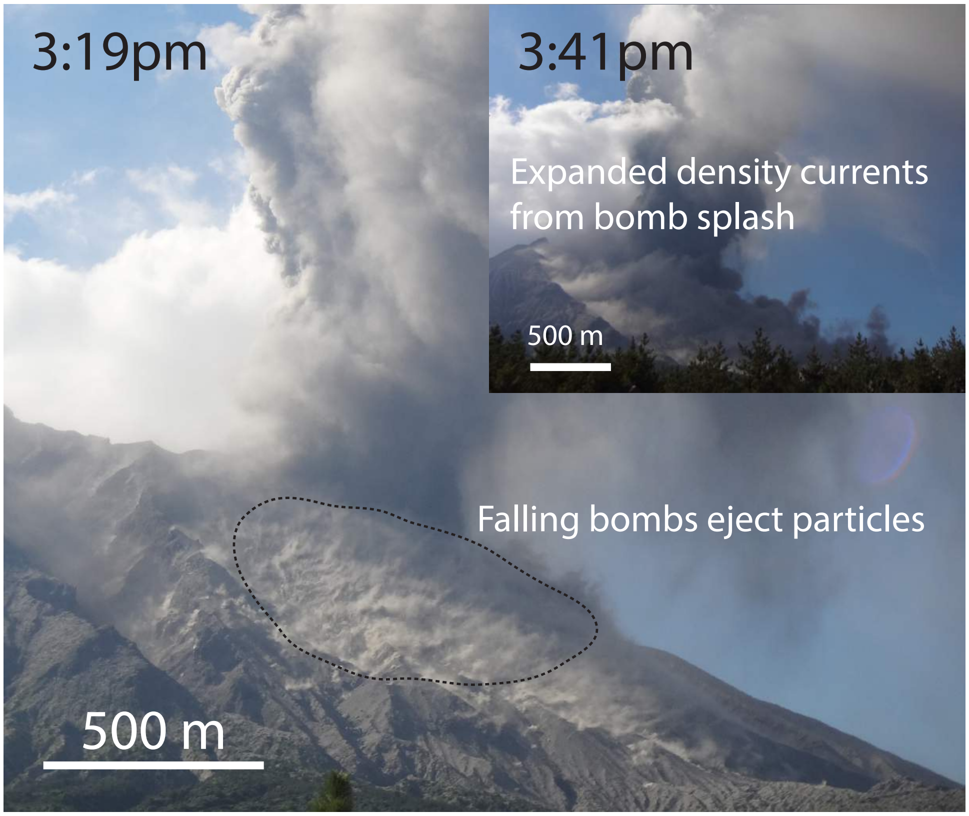

Figure 2.8: The impact of bombs on the flank of Sakurajima volcano, Japan, on 22 July 2013 generates small density currents during a Vulcanian eruption.

2.7.3 Entrainment processes in dilute PDCs

Here we've proposed that splash can drive particle entrainment in dilute PDCs. Indeed, particle saltation has been observed in large-scale physical models of dilute PDCs [66] and proposed as a mechanism to suspend particles in dilute PDCs [67]. [22] observed a pyroclastic surge deposit containing a layer of well-sorted angular pumice clasts and proposed that plinian fallout through a pyroclastic surge emplaced this layer and created a "locally gradational or erosional" boundary between the surge and fallout deposit. We hypothesize that this observation may be, at least partially, a signature of particle splash.

Alternatively, shear and the mobilization of particles by fluid drag may also drive particle entrainment in PDCs as it does in rivers and turbidity currents [e.g., 36, 65, 68]. Splash, however, dominates entrainment in flows where viscosity and density are low and gravity is high such as for wind-blown particle transport on Earth and Mars [42, 43, 47]. Because dilute PDCs are also dilute air-particle mixtures, it is likely that splash also dominates entrainment in these flows. Future work can: (1) look for evidence for splash in PDC models and deposits; and (2) use experimental, theoretical, and numerical techniques from the aeolian transport literature [43] to compare the magnitudes of shear and splash driven entrainment in PDCs.

Particle splash may not just be a mechanism for particle entrainment, but also for PDC generation [e.g., 69]. Bomb impacts may create small density currents and we observed this phenomena during a 22 July 2013 eruption from Showa crater, Sakurajima volcano, Japan, we observed particulate clouds and density currents immediately following the ejection of large bombs onto the flanks of Sakurajima (Figure 2.8). Our interpretation is that the bomb impacts ejected loose particles that expanded into a particulate cloud and density current. There are, however, alternative explanations for this ash cloud suspension such as its generation through strong ground vibrations caused by the eruption.

2.8 Conclusions

Pyroclastic density currents can be both erosional and depositional, yet we currently lack quantitative descriptions of erosional mechanisms [e.g., 4, 5]. In this study, we proposed that impacts from particles falling out of PDCs can eject or "splash" particles back into the currents. We used laboratory experiments to demonstrate that this happens at the particle-scale and to measure the number of particles ejected by impacts of pumice, wood, and nylon spheres. We found that the number of ejected particles increases with the kinetic energy of the impactor and developed a new quantitative expression for particle splash based on energy conservation (Equation 3). Unlike previously proposed Splash Functions, we found that the appropriate length scale for the suspended particles is the depth of the crater created during an impact.

We incorporated splash and Equation (2.3) into a 1-D model of a dilute, compressible density current to examine the effects of particle entrainment on PDC runout. We found that particle entrainment by splash can increase the runout of PDCs by up to an order of magnitude because entrainment by splash increases current density (Figures 2.6 and 2.7). The temperature of the entrained particles also has an important effect on PDC temperature evolution and runout (Figures 2.6 and 2.7). Currents that entrain cold particles runout farther than those that entrain hot particles because hot particles add more thermal energy to the flows and lower air density. Our results show that the temperature and composition of the lower boundary of PDCs can greatly influence PDC runout.

While it is difficult to observe splash in natural PDCs, we observed the creation of small density currents by bombs at Sakurajima volcano, Japan, and observations of erosion beneath fallout deposits within surge deposits suggest that splash can generate erosion. Future work can use experiments, models, and field observations to verify the occurrence of particle splash in PDCs. Splash Functions allow particle entrainment to be mechanistically incorporated into 3-D multiphase and multiphysics models to determine how entrainment affects PDC concentration, stratification, thermal evolution, air entrainment, and runout.

2.9 Acknowledgements

We thank Judy Webb for contributions that enabled this work. We are grateful for constructive comments and feedback from reviewers Olivier Roche and Jennie Gilbert and Editor Andre Revil, and we thank Olivier Roche for the suggestion in the last sentence of section 2.7.3. K.F. was supported by a NSF GRFP fellowship. Additional support was provided by NSFEAR1144198 and NSFEAR1447559. Data and code used in this study are available at https://vhub.org/resources/4068.

2.10 appendix

2.10.1 Splash Function comparison

Here we briefly present several studies of Splash Functions and compare them to experimental measurements. [42] found that

$$N_e = 3.36(0.00572V_i - 0.915)\sin\theta_i, \tag{2.14}$$

where N_e is the number of suspended particles, θ_i is the impact angle with respect to horizontal, V_i is the incidence velocity of the impactor, g is gravity. [49] proposed

$$N_e = 0.55(V_i - 40\sqrt{gd}), \tag{2.15}$$

and

$$N_e = 0.4(V_i - 4.0) + (V_i - 25)\sin\theta_i, \tag{2.16}$$

where d is the diameter of both the impacting and ejected particles. Particle splash has also been described with energy based models. [40] hypothesized that a portion of the kinetic energy of the impacting particle is transferred to the potential energy of the substrate such that $N_e \propto \frac{V_i^2}{gd}$. [41] extended this analysis and proposed

$$N_e = (\frac{d_i}{d_e})^3\frac{V_i^2}{gd_e}. \tag{2.17}$$

Similar energy based Splash Function models have been suggested by [47],

$$N_e = 0.3\frac{V_i^2}{a^2gd}, \tag{2.18}$$

where a is a scaling factor, and [48],

$$N_e = \frac{\beta {V_{in}}^2}{gd}, \tag{2.19}$$

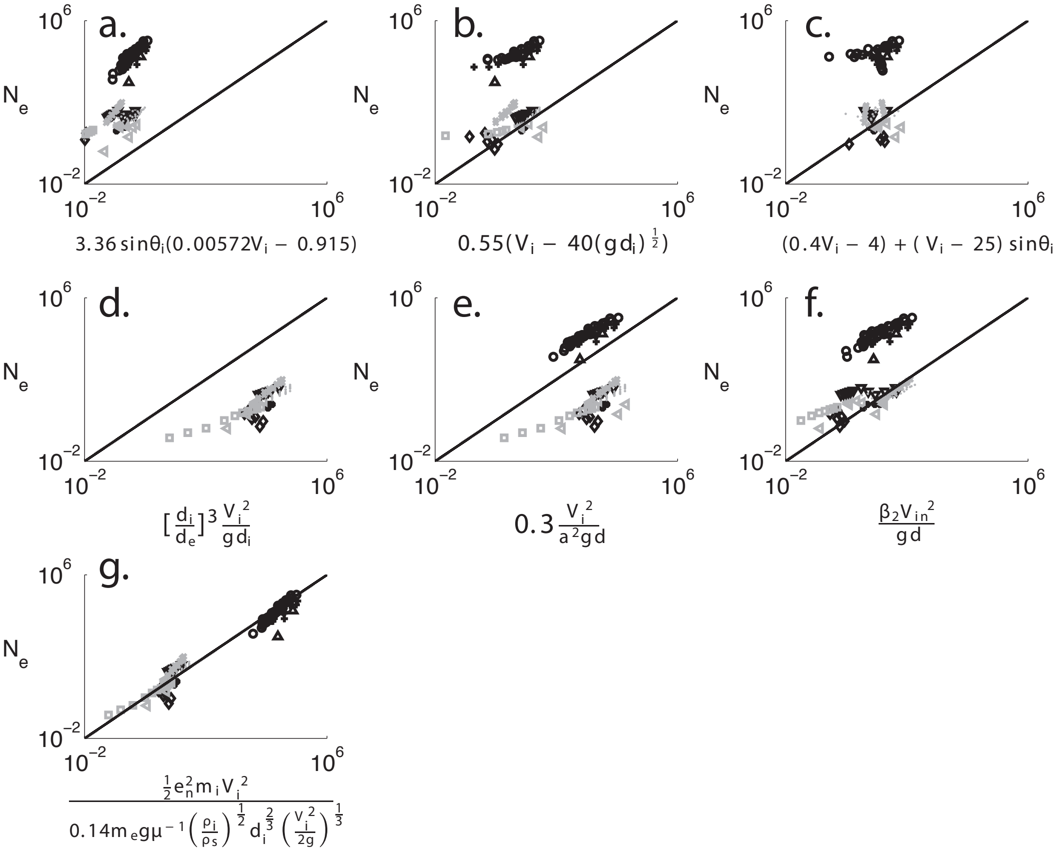

Figure 2.9: Splash Function predictions versus the observed number of ejected particles from eight studies (Table 1). The symbols correspond to those shown in Figure 2.4. Gray represents data from numerical studies, and black represents data from physical experiments. Where d was unspecified we let . (a) Werner [1990]; (b and c) Oger et al. [2008]; (d) Anderson [1987] where $a = 1$; (e) Andreotti [2004]; (f) Wu [2013] where $e_n^2 = 0.008$ and $\alpha = 1$; and (g) the Splash Function from this study, equation (3), where $e_n^2 = 0.008$ and $\mu = 0.5$. Figure A1g (our Splash Function) shows that predictions match observations.

	d_c	d_e
V_i	0.91	0.71
V_{in}	0.71	0.58

Table 2.2: p value model fit comparisons. A combination of d_c and V_i provides the p value closest to 1 and the best model fit

where $\beta = \frac{e_n^2}{2\alpha}$, V_{in} is the normal component of the impactor velocity, e_n is a restitution coefficient, and α is a correction coefficient.

All the expressions suggest that N_e should increase with V_i and Equations (2.14) - (2.19) suggest $N_e \propto \frac{V_i^2}{gL}$ where L is a length scale. However, only Equation (2.3) considers impactor and bed particles of different sizes. None of these expressions consider differing densities or elastic properties between impactor and bed particles.

We test Equations (2.14) - (2.19) against our experimental measurements as well as data from seven other studies (Table 2.5.1). Figure 2.9 shows that these existing Splash Functions do not fit the data. By comparison, Figure 2.9g shows our Splash Function (Equation 2.3) where $e_n^2 = 0.008$ fits the data fairly well.

2.10.2 Alternative Splash Functions

Figure A1 shows that existing Splash Functions are unsatisfactory across a wide parameter range. While section 3 proposed a single new Splash Function, we explore alternative Splash Functions of the form

$$N_e = \frac{e_n^2 \frac{1}{2} m_i V^2}{m_e g L} \tag{2.20}$$

where V can be either the magnitude of velocity, V_i, or the component normal to the bed, V_{in}, and L can be d_e or d_c. To test these alternative Splash Functions, we plot N_s predicted vs. N_s observed and fit a log-linear line to the trends. We let e_n be 0.08 for all trials. The slope of the log-linear line represents the power-law exponent, p, for $N_s^{observed} \propto \left(N_s^{calculated}\right)^p$. A p value close to one demonstrates a good model fit. Table A1 shows the outcome from these trials. Choosing $V = V_i$ and $L = d_c$, which was presented as Equation (2.3) in the main manuscript, provides the best fit.

2.10.3 Settling Velocities

We calculate settling velocities using the formulation in [37]. The change in settling velocity, V, of a particle is,

$$\frac{dV}{dt} = F_g + F_s + g\Big(\frac{2\rho_p - \rho_g}{2\rho_p + \rho_g}\Big), \tag{2.21}$$

where F_g is the force of gas on the particles F_s is the force of many small particles on larger particles, ρ_p is the particle density, and ρ_g is the gas density,. F_g is described through a drag term that is a function of the particle Reynolds number,

$$Re_p = \rho_g \frac{V_s d}{\mu_g}, \tag{2.22}$$

where μ_g is the dynamic viscosity of the gas and d is the particle diameter. The force of gas against a particle is,

$$F_g = \frac{f V_s}{\tau_p}(\frac{2\rho_p}{2\rho_p + \rho_g}), \tag{2.23}$$

where f if an empirical correction to the drag coefficient,

$$f = 1 + 0.15 {Re_p}^{0.687} + \frac{0.0175}{1 + 42500 {Re_p}^{-1.16}}, \tag{2.24}$$

and τ_p is the particle response time,

$$\tau_p = \frac{(\rho_p - \rho_g) d^2}{18\mu}. \tag{2.25}$$

F_s is the force imparted on large particles by small particles.

$$F_s = \left(\frac{6\alpha_1 \sqrt{\theta} g_o (d_1 + d_2)^2}{\sqrt{\pi} d_1^3}\right)\left(\frac{\rho_1 d_1^3 (1+e)(V_{s1} - V_{s2})}{\rho_1 d_1^3 + \rho_2 d_2^3}\right), \tag{2.26}$$

where α_1 is the volume fraction of small particles, θ is the granular temperature of the small particles that is assumed to be 10% of the mean vertical particle velocity, e is a restitution coefficient that is approximately 0.51 based on experiments by [37], g_o is a radial distribution function and we assume that it is approximately one because our current is very dilute. We use Equations 2.21-2.26 to solve for V where $\frac{dV}{dt} = 0$, or particle terminal velocity, in our model.

Table 2.3: Notation

e_n	Splash Function restitution coefficient.
N_e	number of ejected particles.
V_i	impactor velocity.
θ_i	incidence angle.
m_i	impactor mass.
m_e	mass of a suspended particle.
g	gravity.
L	characteristic length scale.
d_c	impact crater depth.
μ	tangent of the friction angle.
ρ_i	impactor density.
ρ_e	ejected particle density.
d_i	impactor diameter.
h_i	height from which the impactor is dropped.
m_a	mass of air per unit area.
$m_{\phi 1}$	mass per unit area of the small particle fraction.
$m_{\phi 2}$	mass per unit area of the large particle fraction.
T_i	initial temperature of particles in the PDC.
T_a	tmbient temperature.
T_c	bulk temperature of the PDC.
H	thermal energy per unit area.
C_p^a	heat capacity of air.
C_p^r	heat capacity of rock.
h	PDC height.
M	molar mass of air.
R	specific gas constant.
P	atmospheric pressure.
ρ_c	bulk PDC density.
u	depth-averaged PDC velocity.
g'	reduced gravity.
E	entrainment coefficient.
t	time.
V_{ϕ_1}	settling velocity of the small particle fraction.
β	Splash Function coefficient.
V_{ϕ_2}	settling velocity of the large particle fraction.
T_e	temperature of the entrained particles.
L_r	runout distance.
a	scaling factor.
ρ_p	particle density.
ρ_g	gas density.
μ_g	dynamic air viscosity.

Chapter 3

Pyroclast cooling and saturation in water

3.1 Summary

In the submarine setting pyroclast cooling and saturation, by controlling the buoyancy of individual clasts and surrounding fluid, exert fundamental controls on the dispersal and fate of volcanic material. In this study I use laboratory experiments to understand and quantify how hot and air-filled pyroclasts cool and saturate in liquid water. By measuring internal temperature and clast submerged weight in over thirty experiments, I find that pumice cools and saturates in two stages. I observe, furthermore, that the first stage is marked by much higher rates of cooling and saturation than the second stage, that the transition between stages is sharp, and that length of time until the stage transition increases with clast size and initial temperature. I propose conceptual and quantitative models for the stages of pyroclast cooling and saturation. Specifically I argue that ingested water accelerates cooling during the first stage, but that as hot pyroclasts convert ingested water to steam, heat loss is necessary to condense internal steam and drive further saturation. I test this idea with a modified Stefan model and conclude that heat loss, rather than permeability, controls the saturation of steam-filled pyroclasts. By comparison, I find that permeability matters for the saturation of clasts with initial temperatures below the boiling point. I propose that the transition time between stages represents the time at which all internal steam condenses and, based on a linear relationship between clast initial thermal energy and stage transition time, derive an empirical average pyroclast cooling rate of $q = 7.5 \pm 0.5$ W cm^{-2}. Last, I argue that the second stage of cooling and saturation is controlled by heat conduction and thermal contraction of trapped gas, respectively, and present quantitative models to test these interpretations. Collectively, these experiments demonstrate how pumice cooling and saturation are coupled, help us understand the timescales over which clasts remain hot and steam-filled, and provide measurements against which new models can be validated. While the scalings we present do not include all the physics relevant for submarine eruptions, they

may prove useful in submarine eruption models and for understanding submarine eruption dynamics.

3.2 Introduction

When pyroclasts erupt into or onto water they are known to at least partially saturate and cool. Experiments show that the water logging of hot lapilli-size pyroclasts can be rapid [e.g., 70–72] and pyroclast cooling, while not yet quantified in water, is thought to provide the buoyancy for submarine plumes [e.g., 11, 73]. In this study we use experiments to quantify how pumice cool and saturate in liquid water. Because cooling and saturation control buoyancy, a clast-scale understanding is central for testing and building models of submarine plumes and pyroclast dispersal.

In the subaerial environment, the fate of pyroclastic material depends on heat transfer, where heat loss from pyroclasts makes plumes buoyant and can control the runout of pyroclastic density currents. Clast-scale models for heat transfer [e.g., 74, 75] have therefore become foundational for multiphase models of subaerial volcanic flows [e.g., 38, 76, 77]. Clast-scale models for heat transfer in water are likewise necessary to understand, and build quantitative models for, submarine eruption dynamics. We expect, however, that pyroclast cooling in water may be complex because water is an effective coolant, porous pyroclasts can ingest water, and phase changes are possible.

In the submarine setting pyroclasts can also themselves be buoyant. Indeed it is known that submarine eruptions can generate rafts of floating pumice [e.g., 12, 13, 78]. Pumice can stay afloat for months to decades [e.g., 79] due to gas trapping and may eventually sink because of gas diffusion [80].

At the same time, experiments have demonstrated that hot (> 300°C) pumice can sink rapidly, often within several seconds, and that the tendency for pyroclasts to saturate increases with clast temperature [70–72]. Whitham and Sparks [1986] suggested that hot pyroclasts generate steam in their pore spaces as they ingest liquid water and that steam generation drives air out. Allen et al. [2008] further argued that the condensation and contraction of vapor drives the saturation of pyroclasts and that “pumice lapilli cool and adsorb water more readily than larger clasts.” These findings suggest that there is a direct connection between pyroclast cooling and saturation.

Conceptual models for submarine plumes often incorporate these observations that pumice can be both positively and negatively buoyant and that heat loss plays a role in dictating buoyancy. For example, Kano et al. [1986] envisions a submarine plume containing both rising and falling clasts and where “hot pumice clasts, especially large ones ... ascend in plume by buoyancy... [while] clasts of smaller sizes rapidly cool down in contact with water and begin to fall out from the plume.” Similarily, Allen and McPhi [2009] depict submarine eruptions where giant pumice can remain hot and buoyant long enough to reach the surface and Cashman and Fiske [1991] model how pumice density dictates clast rise and fallout behavior. The idea that pyroclasts from a single eruption can be sorted into floating and sinking components based, at least in part, on saturation and heat transfer dynamics is consistent with the recent observation that most, but not all, pyroclasts from the 2012 eruption of Havre submarine caldera formed a raft [14]. Work remains, however, to quantitatively test these and other conceptual models for submarine eruption dynamics and pumice rise to the ocean surface.

In this study I use laboratory experiments to quantify clast-scale cooling and saturation in water. I cool pyroclasts in water and we measure their internal temperature and submerged weight. I find that pyroclast cooling and saturation are coupled and occur in two stages. Pyroclasts first cool and saturate rapidly as they ingest water and then more slowly and through conduction once the flow of water into the clasts is reduced. Based on observations, I propose that hot clasts convert ingested water to steam within their pore space, that steam condensation further draws in liquid water, and that cooling controls saturation rather than permeability for very hot clasts. I test these interpretations with quantitative models and, where possible, provide scaling approximations for the different stages of cooling and saturation. Finally, I discuss how these results inform our understanding of submarine eruption dynamics.

3.3 Experimental Methods

I conduct laboratory experiments to examine how air-filled pumice cool and saturate in water using primarily clasts from Medicine Lake, California and also from Santa Maria Volcano, Guatemala and rafted pumice from Havre submarine volcano, Kermadec Arc (Table 3.1). I use subariel clasts because they are similar in vesicularity and macrotexture to the submarine counterparts [e.g., 81] and more readily available. I measure pumice submerged weight through time to calculate and quantify liquid saturation. At the same time, and to examine cooling, I measure pumice internal temperature at one or two locations within the clasts. I explore a parameter range that includes 2 to 9 cm diameter pumice and initial temperatures from ambient to 670°C (Tables 3.2 and 3.4).

To measure pumice internal temperature, we place K-type thermocouples (temperature range up to 1335°C) into 2 mm diameter drilled holes within the clasts. While I tried to center the thermocouple within the clast, irregular clast shapes made centering the thermocouple difficult. Table 3.2 gives $\frac{r}{r_o}$, the ratio of thermocouple location to clast sperhical equivalent diamter, for each clast. I use Al cement to secure and seal the space between the clast and thermocouple.

I heat clasts in one of two different ovens with the thermocouple/s adhered and the thermocouple sheathing bent to fit through gaps in the oven doors. Because one of our ovens has a temperature range less than 260°C and the other oven has a temperature range greater than 460°C, we do not conduct experiments within the 260-460°C range.

To initiate an experiment, I remove the clast from the oven and quickly submerge the clast 1 to 3 cm below the surface of a twelve liter and 20°C water bath (Figure 3.1). The water bath is large, as is the heat capacity of water, such that we expect temperature

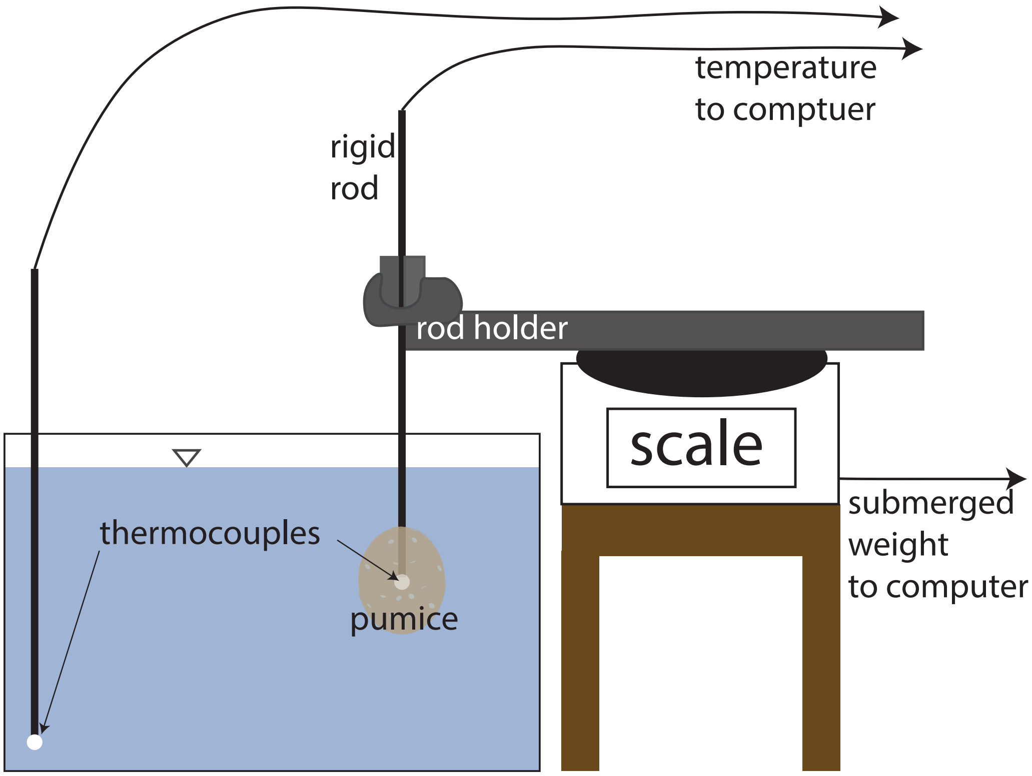

Figure 3.1: Experimental set-up. We measure the internal temperature and submerged weight of pumice clasts as they are cooled in a water bath.

gradients within the bath to be minimal. Indeed, we do not observe changes in background temperature as the clasts are cooled. Near the clast, water temperature may be elevated. Hydrostatic pressure gradients that drive water into the clast [e.g., 80, 82] are proportional to clast size rather than depth below the water surface.

As the clast is submerged, we record clast internal temperature and water bath temperature at 0.42 Hz. When two thermocouples are present in a clast, we are able to observe temperature gradients in a single clast. We do not assume that temperature is uniform within a clast.

We measure clast submerged weight at 1 Hz by connecting a rigid rod extending from the thermocouple(s) to the scale (Figure 3.1). Because the pumice enter the water before the rigid rod is placed on the scale, there is a 1-2 second delay between the time the clast is submerged and the time when we begin measuring submerged weight. Submerged weight increases as the pumice become saturated because the downward force exerted on the scale is proportional to pumice density, which increases as the pumice saturates. Clasts are often

Table 3.1: Pumice clast characteristics: characteristic radius, r_o, is estimated by assuming a spherical geometry and * refers to values calculated by assuming porosities (70% for Pum08 and 80% for HRaft01). n refers to the number of experiments conducted on each clast. $\frac{r_t}{r_o}$ refers to the thermocouple position relative to clast radius, $\frac{r_t}{r_o} = 1$ implies that the thermocouple is at the center of the clast. Uncertainties are calculated as the standard deviation of a set of measurements. We do not report uncertainties where only one measurement was made or if multiple measurements report the same values.

clast name	source	mass (g)	volume (cm^3)	porosity	r_o (cm)	$\frac{r_t}{r_o}$	n	Bi	H ($\frac{\mathrm{W}}{\mathrm{m^2K}}$)
ML01	Medicine Lake, CA	7.7	11.1	0.70	1.4	0.73	9	3.6±0.6	194±35
ML02	Medicine Lake, CA	38.9	50.5	0.67	2.3	0.65	9	9.9±3.6	314±115
ML03	Medicine Lake, CA	7.9	11.6	0.70	1.4	0.71 & 0.35	4	4.3±0.5	223±29
Pum06	unknown	5.7	6.8	0.64	1.2	0.68	2	5.5±0.5	359±33
SM16	Santa Maria, Guatemala	4.3	7.0	0.74	1.2	0.67	1	4	240
Pum07	Medicine Lake, CA	63.8	83.2	0.67	2.7	0.70	2	6	167
Pum08	Medicine Lake, CA	302.2	*403.0	*0.70	*4.6	*0.87	1	2	33
HRaft01	Havre 2012 raft	60.7	*121.4	*0.80	*3.0	*0.98	1	1	20

initially buoyant, however the rigid rod forces the clasts below the water surface. Buoyant clasts push up against the rigid rod such that their buoyance is reflected in the submerged weight measurement.

Pumice submerged weight is the clast out-of-water weight, M_T, less the displaced water weight,

$$M_S = M_T - \rho_l V_T, \tag{3.1}$$

where V_T is the pumice volume. I determine pumice volume, V_T, by separately measuring the submerged weight of a dry clast [83]. In our experiments I directly measure M_S.

I relate the change in submerged weight, M_S, to the change in the volume change of liquid water within the pumice, V_l, according to

$$\Delta M_S = \rho_l \Delta V_l, \tag{3.2}$$

where ρ_l is liquid water density. We calculate the flux of liquid water into the pumice from M_S according to

$$Q_l = \frac{dM_S}{dt}, \tag{3.3}$$

where t is time, and Q_l has units of grams per second. We report Q_l and ΔM_S rather than M_S because the weight of the thermocouple wire added uncertainty (±3 g) to M_S but did not affect the accuracy of ΔM_S.

I record video (60 frames per second) of some experiments to examine gas escape and look for surface boiling. A complete list of experiments is in Table 3.4.

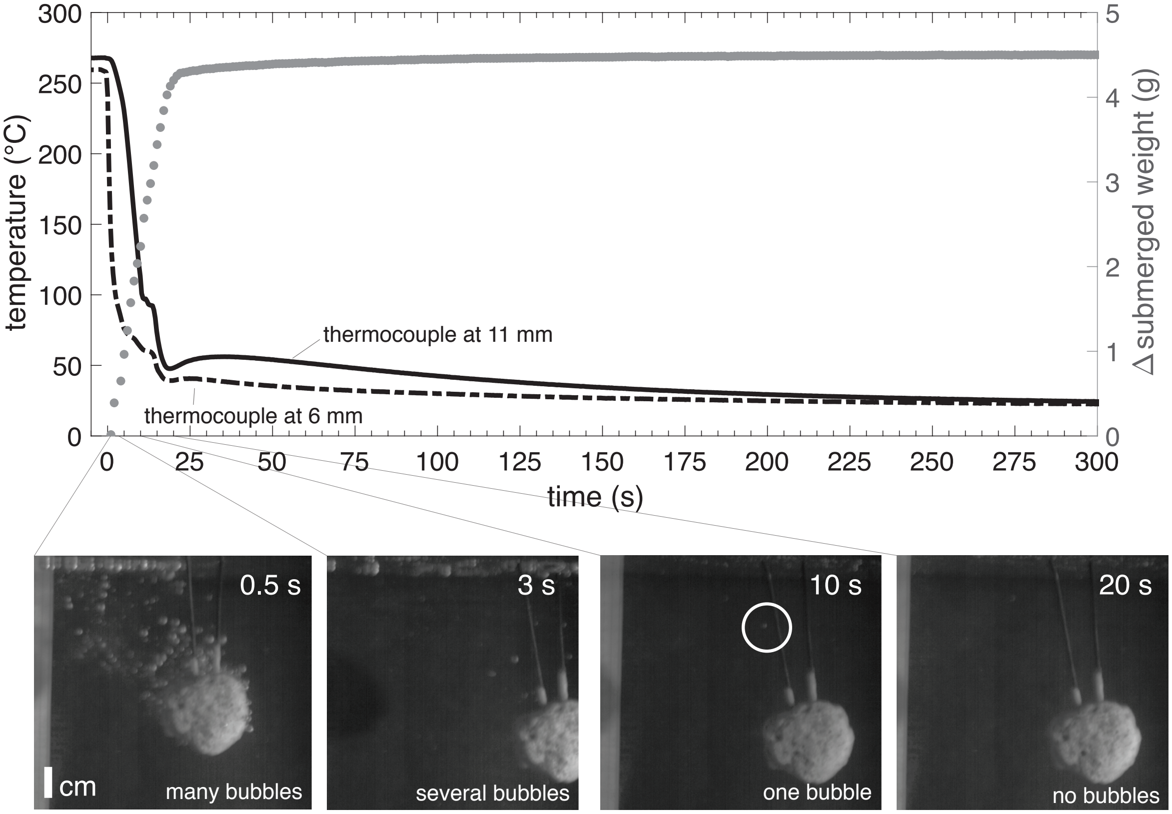

Figure 3.2: Cooling and saturation of 7.9 g Medicine Lake clast ML03 from an initial temperature of 265°C. I measure internal temperature at two locations within the clast: 6 and 11 mm from the clast edge. I find that submerged weight increases and internal temperatures drop rapidly in the first 19 seconds following submersion. I observe bubbles flowing in the first $3 - 5$ seconds following submersion. I find that ΔM_S plateaus at the same time (≈19 s) internal temperatures reach local minima.

3.4 Results

I first describe observations of cooling and saturation of a single and representative pyroclast. I then describe how cooling and saturation depend on clast initial temperature. Finally, I identify several general sets of behavior that occur as pumice cool in liquid water.

3.4.1 Cooling and saturation of a representative clast

Here I describe the cooling and saturation of a representative 7.9 g clast from Medicine Lake, Calfornia (ML03) from an initial temperature of 265°C (Figure 3.2). I placed thermocouples at two locations within ML03, 6 and 11 mm from the edge, and report change in submerged weight as $\Delta M_S = M_S(t) - M_S(t=0)$.

I find that the submerged weight of ML03 increases immediately following submersion and gas bubbles vigorously flow out (Figure 3.2). Internal clast temperature drops more than 150°C within the first 10 seconds following submersion.

The rate of visible gas bubble escape slows within the first several seconds following submersion, yet clast submerged weight continues to increase. At 10 s, the temperature recorded by the 11 mm thermocouple plateaus near 100°C before falling rapidly.

At 19 seconds, I observe an inflection point in submerged weight, indicating a decline in liquid flux into the clast. At $\approx$ 19 seconds, I also observe local minima in temperature at both thermocouples, after-which temperature increases at both thermocouples before declining again.

Experiments on other clasts and at other initial temperatures exhibit similar behavior. Specifically, I find that clasts with initial temperatures greater than the boiling point (100°C at 1 atm) exhibit a sharp transition between high initial liquid flux stage and second low liquid flux stage (Figure 3.2).

At the time of this high-to-low liquid flux transition, we observe corresponding changes in temperature. In some clasts (e.g., Figure 3.2) we observe local minima in the temperature and in others we see an inflection point (e.g., Figure 3.14). Regardless of the specificities of observed temperature time series, we find that internal clast temperature is always $\leq$100°C at the high-to-low liquid flux transition.

3.4.2 Initial temperature effects

To determine how clast initial temperature and thermal energy affect cooling and saturation, I conducted experiments where I varied the initial temperatures of two clasts from Medicine Lake, ML01 (7.70 g) and ML02 (38.90 g). Figure 3.3a shows how the temperature 10 mm within clast ML01 changes during the first sixty seconds of the experiments. Figure 3.3b shows liquid flux (Equation 3.3) as a function of time.

Several trends are apparent in Figure 3.3. First, liquid flux declines sharply in experiments where the initial temperature is greater than 100°C. In this study, I manually mark the time, t^*, at which these high-to-low liquid flux transitions occur with stars. Mathematically, one could define t^* as the time at which the second temporal derivative of submerged weight reaches a minimum

$$t^* = \min(\frac{d^2 M_S}{dt^2}) \tag{3.4}$$

While I do not employ this mathematical definition here and identify t^* by eye, I find that t^* increases with clast initial temperature as illustrated in the inset to Figure 3.3b. I find, furthermore, that clast internal temperatures are less than 100°C at t^*.

Second, I find that the initial flux of liquid into the clast is highest for initial temperatures of 139 and 170°C, second highest for initial temperatures of 205 and 257°C, and third highest for initial temperatures $\geq$ 458C°. We observe, however, that the initial liquid flux is the same in experiments with initial temperatures $\geq$ 458°C. Similar results from clast ML02 are

Table 3.2: Cooling and saturation stages

Stage and Interpretation	Observations	Scaling
(1a) Gas escape controlled: Gas flows out of clasts and liquid water enters. Heat is transferred to ingested water.	Submerged weight increases and clast internal temperature declines. Visible bubble flow out of the pyroclasts.	For initial temperatures < 100°C: $Q_l \propto e^{-\xi t}$
(1b) Heat conduction and steam condensation controlled: Heat loss causes condensation of internal water vapor which further drives liquid infiltration and cooling. Stage 1b ends when all the steam within the clast has condensed and the liquid flux into the clast is small. A clast can be partially saturated at the end of stage 1 due to the trapping on non-condensable gas.	We observe few bubbles escaping from the clast. Internal temperatures plateau at 100°C. Liquid flux is lower for very hot clasts compared to warm clasts. (Figure 3.3)	$q = 7.5 \pm 0.5$ W cm^{-2} $\frac{Q_l}{S_a} = \frac{q}{\phi L}$
(2) Heat conduction controlled: Clast cooling by convective heat loss and conduction. Slow liquid saturation results from thermal contraction of non-condensable gas bubbles. Internal clasts temperatures can increase at the beginning of stage 2 due to temperature heterogeneities at the onset of stage 2	Submerged weight increases gradually and internal temperatures slowly approach ambient	$\ln \frac{T(r,t)-T_\infty}{T_i-T_\infty} \propto t$ $Q_l \propto \frac{dT}{dt}$

shown in Figure 3.15. I repeated experiments on the same clast at the same temperature to demonstrate that the the experimental results were repeatable (Table 3.9.4).

The observation that clasts with initial temperatures between 139 and 267°C have higher initial liquid fluxes than clasts with initital temperatures ≥ 458°C, suggests that clast thermal energy can impede clast liquid saturation. The observation that liquid flux does not vary with clast initial temperature for temperatures ≥ 458°C suggests that, for these conditions, the pressure gradients driving liquid flow are the same. We note that we cannot observe behaviors of clasts with initial temperatures from $\approx 260 - 460$°C because our ovens do not operate in this range.

3.4.3 Conceptual models for pumice cooling and saturation

Here I identify several general behaviors that occur as pumice cools and we outline these as stages in Table 3.2 and Figure 3.4. I define stage 1 as the stage between pumice

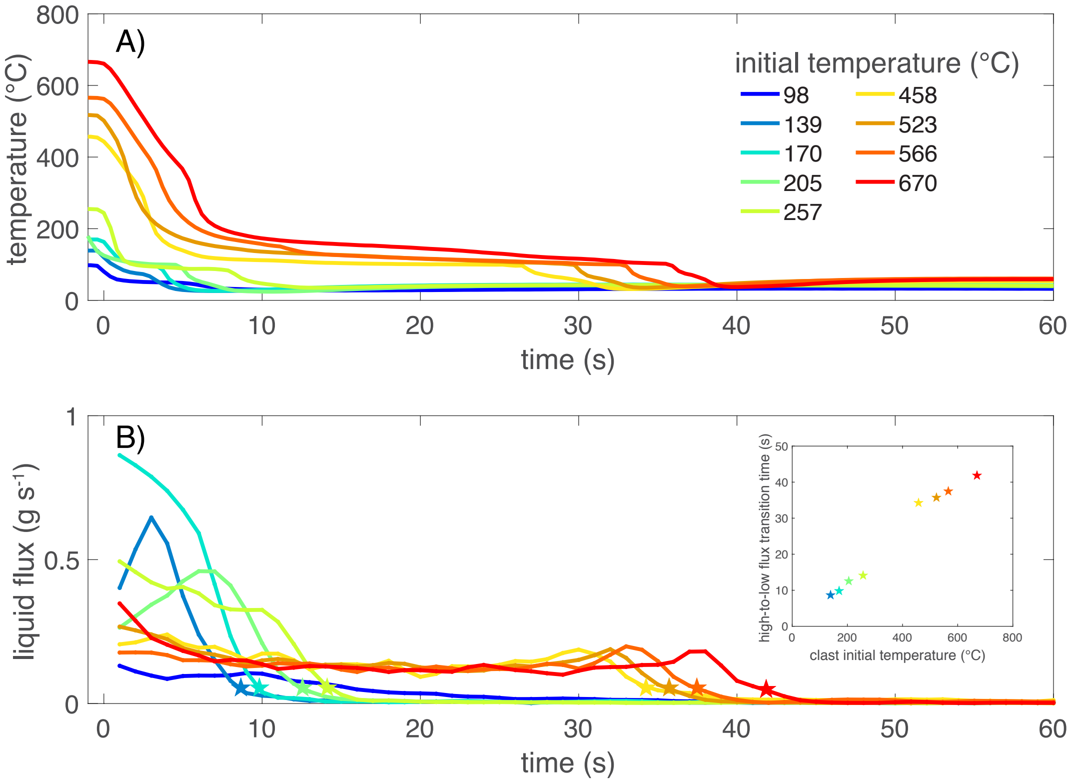

Figure 3.3: Effects of initial temperature on cooling and saturation. (A) Internal temperature of clast ML01 as a function of time. Clast internal temperature declines rapidly, then plateaus near 100°C, and finally drops quickly below 100°C. Initially hotter clasts take longer to cool below 100°C. (B) Liquid flux (g s^{-1}) into the clasts as a function of time. Clasts with initial temperatures below 100°C exhibit the lowest liquid fluxes. Otherwise, initial liquid flux decreases with increasing initial clast temperature. All clasts with initial temperatures above 100°C exhibit sharp high-to-low liquid flux transitions (marked with stars). The inset shows how the timing of the high-to-low liquid flux transition increases with clast initial temperature.

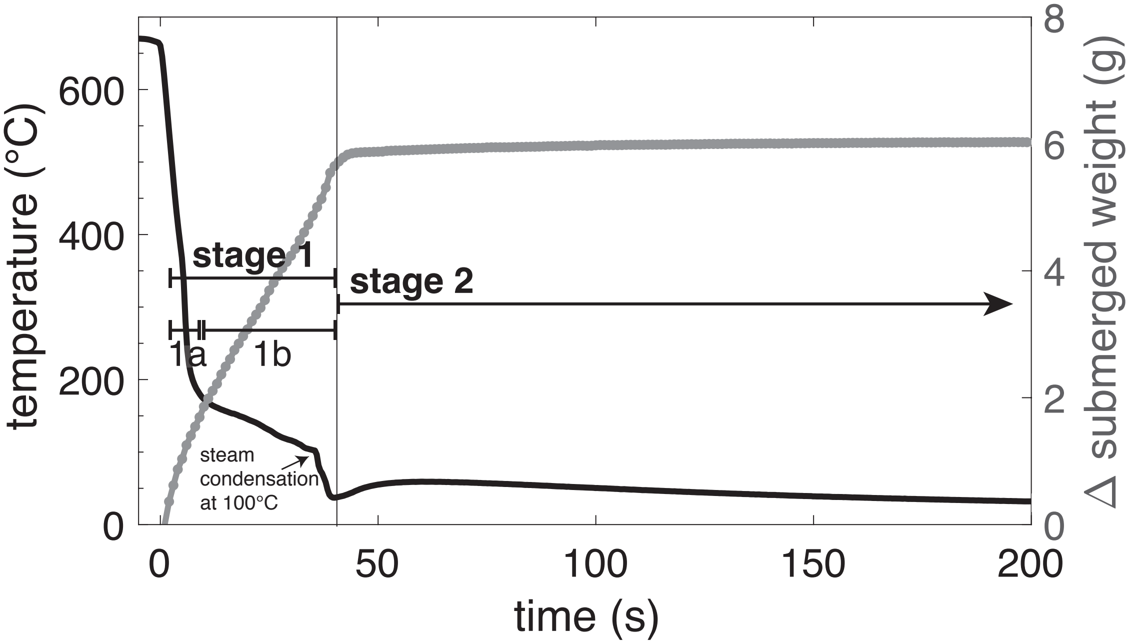

Figure 3.4: Cooling and saturation stages of representative clast ML01. We propose that cooling and saturation takes place in several stages and over which different processes dominate. Stage 1a: Water enters the clast as air flows out. Stage 1b: Ingested water is heated and converted to steam. As the clasts cool, internal steam condenses and generates a pressure gradient that draws in liquid water. Stage 1 ends once all internal steam has condensed. Stage 2: We propose that cooling occurs through conduction and saturation is controlled by the thermal contraction of trapped non-condensable gas.

submergence and t^*, the high-to-low liquid flux transition (Figure 3.4). Stage 2 follows stage 1 and is the time over which the liquid fluxes become small and internal temperatures approach ambient. The majority of cooling and saturation occur during stage 1 and I suggest, based on temperature measurements and video observations, that stage 1 consists of two substages. In this section I describe the processes we hypothesize are important in each stage and substage. In section 3.5 I test these hypotheses against quantitative models.

I define stage 1a as the time over which we observe vigorous bubble escape from the clasts (Figure 3.2). I do not see steam generation at the clast surface, rather we observe air flowing out of the clasts. I typically find that vigorous the bubbling ceases within seconds to tens of seconds following submersion (Figure 3.2). Internal temperatures fall rapidly during this time and I propose that this is due to rapid heat transfer between thin pumice walls and ingested water (e.g., Figures 3.2 – 3.4). Mechanisms that may draw in water and drive out air include hydrostatic pressures and capillary forces [e.g., 82], thermal contraction [e.g., 71], and hydrodynamic instabilities [e.g., 18].

I propose that clasts can be hot enough to convert ingested water to steam. I define stage 1b as the time over which there is appreciable steam within the clasts (Table 3.2). I further propose that clast cooling causes water vapor condensation and that the associated volume change draws in liquid water. Allen et al. [2008] and Whitham and Sparks [1986] proposed a similar connection between pumice cooling and saturation where, "as the pumice cools below 100°C the steam will condense leading to water vapor being adsorbed." Stage 1b may therefore be useful for understanding the behavior of initially steam-filled clasts.

Several experimental observations support the hypothesis that water vapor condensation leads to saturation including: (1) the absence of visible gas escape as submerged weight increases; (2) the observation that the rate of cooling with time increases immediately after internal temperatures fall below 100°C (Figure 3.4) - consistent with a condensation-associated volume change drawing cooler water to the thermocouple; and (3) the observation that very hot > 458°C pumice saturate more slowly than lower temperature pumice (Figure 3.3) - suggesting that heat loss impedes saturation.

I suggest that Stage 1b ends when all steam within the clast has condensed. I recognize the end of stage 1, t^*, as the time when liquid flux becomes small. I note that clasts with initial temperatures < 100°C do not exhibit an abrupt change in liquid flux, possibly because cool clasts cannot generate steam.

Stage 2 begins when the flux of liquid water into the clasts becomes small. During stage 2 I expect that clasts contain only liquid water and, possibly, non-condensable gas such as trapped air [80]. I hypothesize that heat conduction controls stage 2 cooling and saturation through the thermal contraction of trapped non-condensable gas.

3.5 Quantitative models of pumice cooling and saturation

Here I discuss the pumice cooling and saturation stages identified in Table 3.2 and propose quantitative models for most stages.

3.5.1 Stage 1a: Saturation of pumice, $T_i < 100$°C

I find that the flux of liquid water into clasts (Equation 3.3) decreases exponentially with time for clasts with initial temperatures less than the boiling point such that

$$Q_l(t) = Q_o \exp(-\xi t), \tag{3.5}$$

where Q_o is the initial flux of liquid into the clast, ξ is a fitted coefficient, and t is time (Figure 3.5). The exponential decline in Q_l is consistent with a Darcy model for flow in

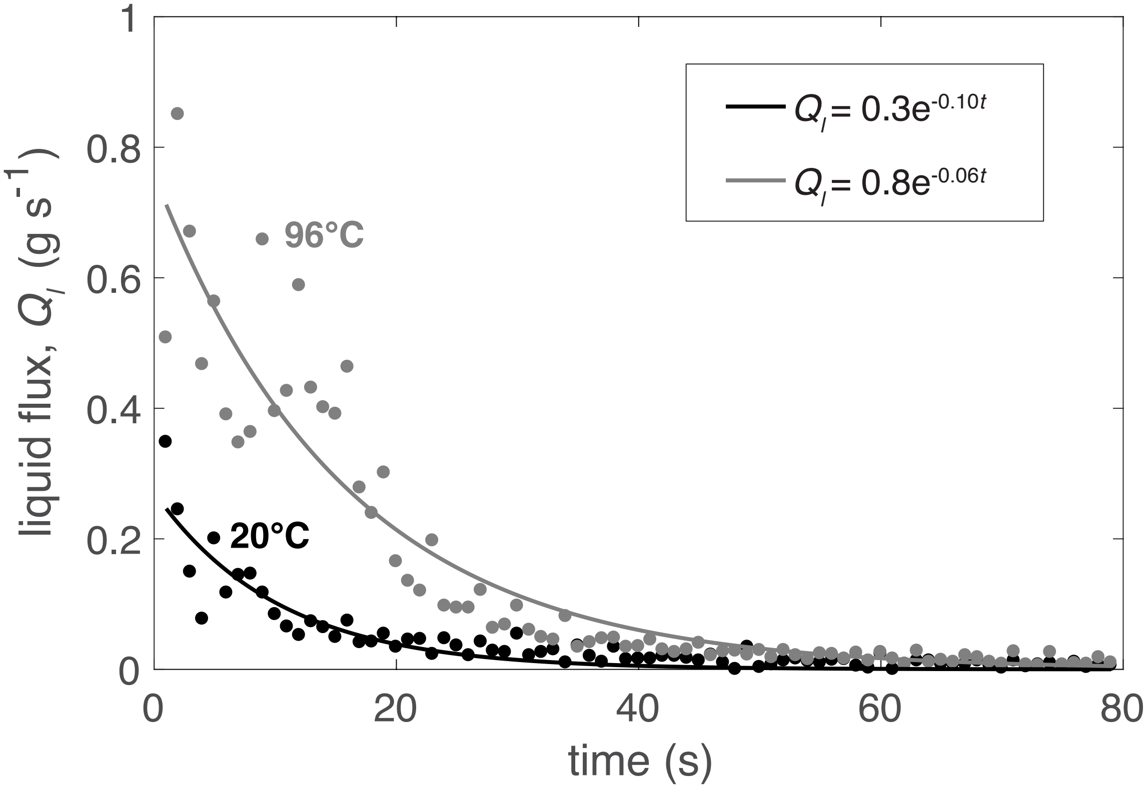

Figure 3.5: Flow declines exponentially with time for clasts with initial temperatures < 100°C. I fit Equation 3.5 to measurements of liquid flux from clast ML02 and find that liquid flux increases with clast initial temperature.

which pressure gradients are generated by hydrostatic pressure and capillary suction [84, 85]. Vella and Huppert [2007] modeled pumice saturation as a Darcy flow problem. I find that for the same clast, initial liquid flux increases with initial clast temperature (Figure 3.5) and I hypothesize that this is because thermal contraction adds to the pressure gradient drawing water into the clast.

3.5.2 Stage 1a: Saturation of pumice $T_i > 100°$C

When the initial temperature of a clast is greater than the boiling point, I observe that the initial saturation and cooling of the clast are rapid (e.g., Figure 3.3). I attribute the rapid cooling and saturation to the escape of non-condensable gas and infiltration of liquid water into the clast accelerated by thermal contraction of air and hydrodynamic instabilities [e.g., 18, 71]. While stage 1a liquid flux is high, I do not yet have a quantitative model to predict cooling and saturation during this phase.

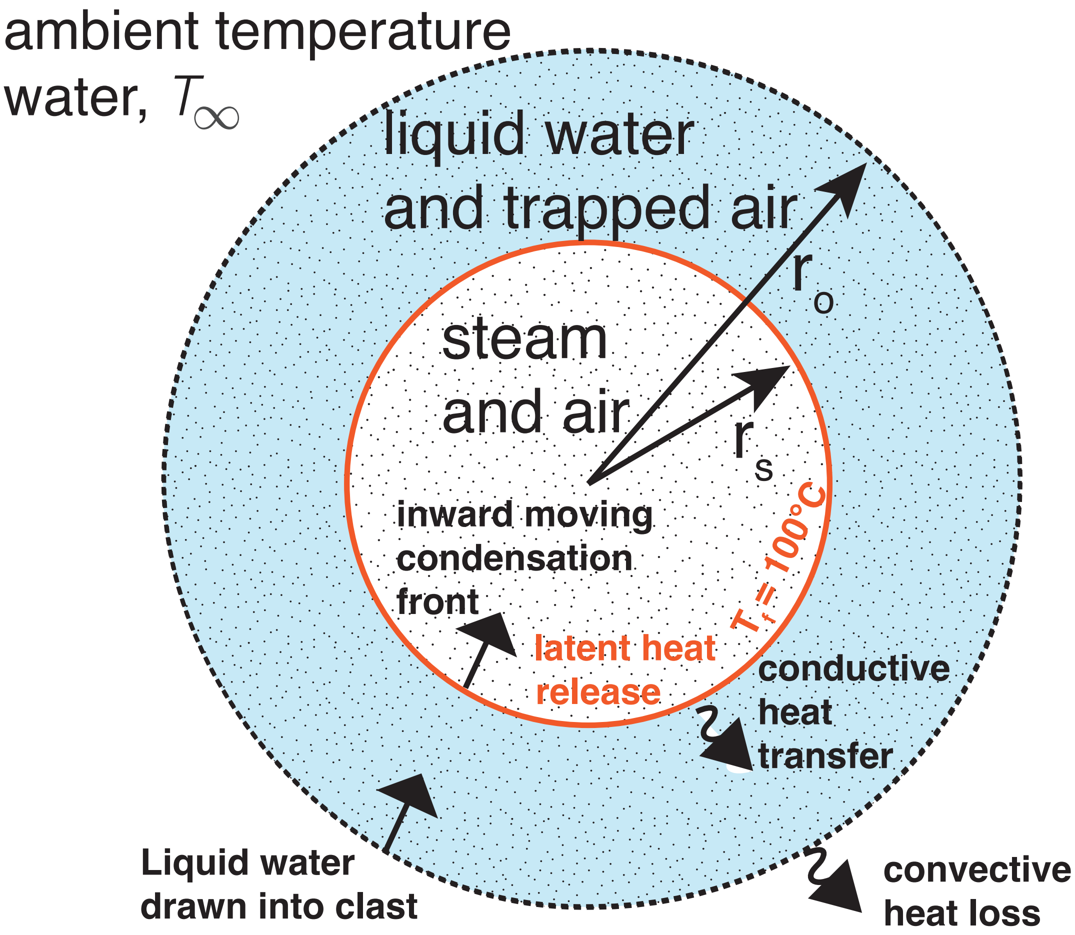

Figure 3.6: Conceptual model of stage 1b cooling and saturation. Clasts contain steam in their interiors that cools and condenses as heat is conducted out of the clast. The production of latent heat from steam condensation balances outward heat conduction at the interface. Liquid water is drawn in at the velocity at which the condensation interface moves inward. The mathematical details of this model are given in Section 3.9.2.

3.5.3 Stage 1b: Steam condensation drives saturation (why saturation is controlled by heat transfer)

Stage 1a transitions to stage 1b when clasts contain enough thermal energy to heat and convert ingested water to steam. I envision that stage 1b is dominated by an inward moving condensation front, where clast centers contain steam that condenses as the clasts cool by

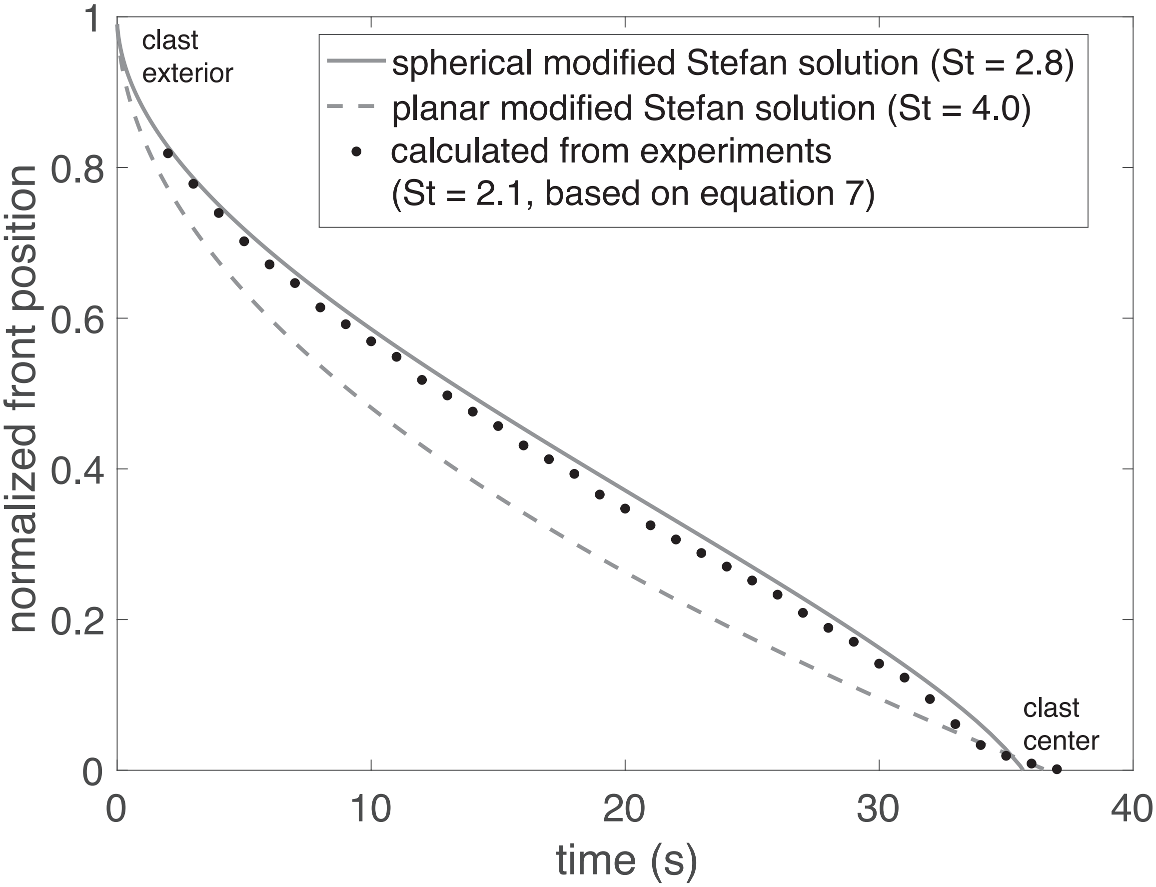

Figure 3.7: Dimensionless liquid infiltration front location as a function of time. We use our experimental measurements to calculate the condensation front position (Equation 3.9 with $C_1 = 2.6$, black circles). I compare calculated front position to solutions from a modified Stefan model in spherical and planar geometries (Section 3.9.2). I find that, using similar Stefan numbers, the modified Stefan model matches our experimental measurements, lending support to the conceptual model for stage 1b depicted in Figure 3.6.

conduction (Table 3.2). In this model, the volume-change associated with condensation creates a pressure gradient that draws in liquid water (Figure 3.6). Because steam must condense for the clasts to saturate, I argue that saturation is limited by heat loss rather than permeability. Here I calculate the dimensionless Peclet number, Pe, the ratio of advective heat transfer to conductive heat transfer rates. Saturation is limited by the slowest process (either advection or diffusion) such that a large Peclet number implies that saturation is heat diffusion limited.

To estimate Pe, I calculate a lower bound for the velocity of liquid water entering a clast and driven by hydrostatic and capillary forces $v = \frac{\kappa}{\mu\phi}(\rho_l g(2r_o) + \frac{2\gamma}{d})$, where κ is permeability, μ is liquid viscosity, ϕ is porosity, ρ_l is water density, g is gravity, r_o is clast radius, $\gamma = 0.072$ N m^{-1} is surface tension, and d is a characteristic pore radius. Taking clast diameter, $2r_o$, as a characteristic length scale, I therefore write

$$\mathrm{Pe} = \frac{v(2r_o)}{D_{eff}}, \tag{3.6}$$

where D_{eff} is an effective thermal diffusion coefficient [e.g., 86]. Equation 3.6 shows that Pe increases with clast size (i.e., Pe $\propto {r_o}^2$ where $v \propto r_o$). A large Peclet number implies, furthermore, that saturation is limited by heat diffusion rather than advection. For a 1 cm and 1 m clast we estimate Pe = 0.83 and 137, respectively. In these calculations I assume $\kappa \approx 10^{-12}$ m^2 [e.g., 87–95], $\phi = 0.70$, $d = 10^{-5}$ m. I also account for porosity such that $D_{eff} = D_w\phi + D_r(1-\phi) \approx 2.5 \times 10^{-7}$ m^2 s^{-1} for $\phi = 0.7$ and where D_w is the diffusivity of liquid water D_r is the diffusivity of glass [e.g., 96]. I find that permeability would have to be less than 7×10^{-15} m^2 s^{-1} to influence the dynamics of a meter size clast and less than 10^{-13} m^2 s^{-1} to influence the dynamics of a 10 cm size clast. Because Pe is large for large clasts, we neglect permeability in our stage 1b model for clast saturation.

To test a steam-filled and heat conduction limited conceptual model for stage 1b (Figure 3.6), I compare measurements of liquid flux to a modified Stefan model, where the outward conduction of heat is balanced by latent heat production at a condensation interface [e.g., 97, 98]. Section 3.9.2 gives the modified Stefan model equations that I solve numerically. Briefly, I add an advective term to 1-D Stefan problems to account for the liquid water that is ingested as a result of the volume change associated with condensation. I assume that the liquid infiltration velocity is the same as the velocity of the moving steam condensation interface. Latent heat release at the condensation interface balances heat conduction at the interface. I also assume that a constant heat transfer coefficient can describe heat loss at the clast's outer boundary and that the clast's steam-filled interior is at a constant temperature of 100°C [e.g., 98]. I solve the modified Stefan problem numerically for both a planar and spherical geometries (Section 3.9.2).

The ratio of sensible to latent heat in the clast is key to the modified Stefan model dynamics and can be expressed by the Stefan number, St. Estimating the Stefan number for our experiments is complicated because all heat begins as sensible heat and a portion of a clast's initial thermal energy is converted to latent heat as ingested water flashes to steam. To determine how much heat is partitioned into latent heat, consider the initial heat content of a clast, H_r at initial temperature T_i and entirely filled with liquid water at ambient temperature, $H_r = T_i c_{pr}(1-\phi)\rho_r V_T + T_\infty c_{pl}\phi\rho_l V_T$, where c_{pr} is the heat capacity of the glass phase, ρ_r is the density of the glass phase, c_{pl} is the heat capacity of the liquid phase, and ρ_l is the density of the liquid phase [e.g., 86, 96]. Now I estimate the temperature of the clast and water assuming that the clast and water inside instantly equilibrate to the same temperature.

$$T_{eq} = \frac{T_i c_{pr}(1-\phi)\rho_r + T_\infty c_{pl}\phi\rho_l}{c_{pr}(1-\phi)\rho_r + c_{pl}\phi\rho_l}. \tag{3.7}$$

To determine St, I assume that all heat that brings clast temperature, T_{eq}, above 100°C, is partitioned into latent heat such that

$$\mathrm{St} = \frac{T_f}{T_{eq} - T_f}, \tag{3.8}$$

where T_f is the condensation temperature, 100°C at 1 atm. Equations 3.7 and 3.8 demonstrate how, as clast initial temperature increases, more heat is partitioned into latent heat and the Stefan number decreases. For 70 percent porosity clasts with initial temperatures of 400 and 700°C, I calculate Stefan numbers of 6 and 1, respectively. Equations 3.7 and 3.8 do not include the effects of trapped gas. I expect latent heat to be even more important for clasts that are initially filled with steam, such as those in submarine eruptions, and suggest that a Stefan number can be estimated for initially steam-filled clasts according to $\mathrm{St}_{steam} = \frac{T_f}{T_i - T_f}$.

I compare our experimental measurements of liquid flux to the modified Stefan model solution for an inward moving condensation front in Figure 3.7. To relate our experimental measurements of liquid flux to the position of a condensation front I assume pumice saturation can be modeled as saturation of a series of parallel tubes where the surface area over which saturation occurs does not change with time. I therefore calculate

$$\frac{dr_s}{dt} \propto \frac{Q_l(t)}{\phi S_a^c}, \tag{3.9}$$

where r_s is the location of the condensation front, $S_a^c = \frac{1}{C_1} 4\phi\pi {r_o}^2$ is the surface area of the condensation front, C_1 is an empirically determined constant, ϕ is porosity, and $Q_l(t)$ is the calculated liquid flux (Equation 3.3).

Figure 3.7 shows how condensation fronts move inward with time for both a representative experiment (ML01 with $T_i = 523$°C) and from the numerical solutions to the modified 1-D modified Stefan problem. From Equation 3.8 I estimate St = 2.1 for the experiment shown in Figure 3.7. I find that numerical solutions to the modified Stefan problem in spherical and planar coordinates, and with respective Stefan numbers of 2.8 and 4, fit the experimental measurements well (Figure 3.7).

I propose that stage 1b ends when all steam within the clast has condensed to water and the condensation front has reached the center of the clast. Because steam is often the primary magmatic gas within pyroclasts, a modified Stefan model may be appropriate for modeling

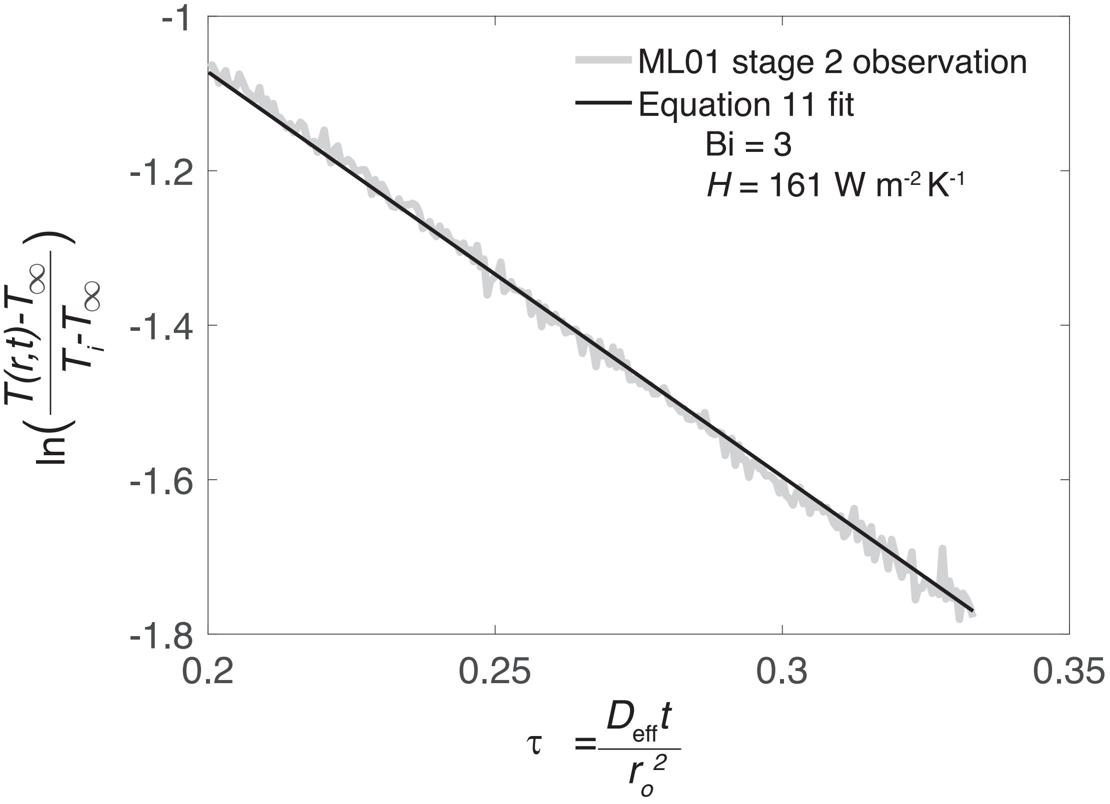

Figure 3.8: Stage 2 temperature as a function of dimensionless time, τ. I find that dimensionless temperature scales with $e^{-\tau}$, supporting the concept that clasts cool through conduction during stage 2. I fit conduction model solutions on a sphere (black line) to the experimental measurements to estimate Biot numbers and heat transfer coefficients. See Table 3.1 for a list of fitted Bi and H values.

the cooling and saturation of submarine pyroclasts. Stefan models explicitly demonstrate how cooling and saturation are coupled and, because cooling and saturation are limited by conduction, demonstrates why pyroclasts may stay stay hot and potentially buoyant for long times.

3.5.4 Stage 2: Conductive Cooling

The beginning of stage 2 is marked by an abrupt decline in liquid flux (e.g., Figure 3.3) and I propose that heat is loss is dominated by conduction, rather than advection, during stage 2. To test this hypothesis, I compare stage 2 temperature measurements to solutions of a heat conduction model on a sphere (Section 3.9.1). To model stage 2 cooling

I assume: (1) pumice is spherical; (2) the clast has a uniform initial temperature, T_i; (3) clast internal structure is uniform; (4) the clast's convective heat flux is uniform with heat transfer coefficient, H; (5) the water bath has constant temperature T_∞; (6) all pumice pores are filled with liquid water; and (7) heat is transferred by conduction inside the clast.

The Biot number expresses the ratio of internal to external resistance to heat transfer and is

$$\mathrm{Bi} = \frac{H r_o}{k_{eff}}, \tag{3.10}$$

where H is the heat transfer coefficient, r_o is the clast radius and k_{eff} is effective thermal conductivity. A Biot number ≤ 0.1 implies that heat loss is limited by external heat transfer and the temperature within the clast is approximately uniform. Because I find that clast internal temperatures are spatially variable during stage 2 (e.g., Figure 3.2) I expect that $\mathrm{Bi} \geq 0.1$ and therefore a lumped capacitance model is not suitable.

The exact solution for the time dependent non-dimensionalized radial temperature distribution (Section 3.9.1), $\theta(r,t) = \frac{(T(r,t)-T_\infty)}{(T_i-T_\infty)}$, across a conductive sphere with a convective boundary layer is,

$$\theta(r,t) = \frac{(T(r,t)-T_\infty)}{(T_i - T_\infty)} = \sum_{n=1}^{\infty} A_n \exp(-\lambda_n^2 \tau) \frac{\sin \lambda_n \frac{r}{r_o}}{\lambda_n \frac{r}{r_o}}, \tag{3.11}$$

where r is clast radial position, $\tau = \frac{D_{eff} t}{r_o^2}$ is non-dimensionalized time and D_{eff} is effective thermal diffusivity, $A_n = \frac{4(\sin\lambda_n - \lambda_n \cos\lambda_n)}{2\lambda_n - \sin 2\lambda_n}$ and the values for λ_n are the positive roots of the transcendental equation $\mathrm{Bi} = 1 - \lambda_n \cot(\lambda_n)$ [e.g., 99].

The solution to Equation 3.11 can be approximated with the first term of the series for $\tau > 0.2$ [99] such that

$$\theta(r,t) = \frac{(T(r,t)-T_\infty)}{(T_i - T_\infty)} = A_1 \exp(-\lambda_1^2 \tau) \frac{\sin \lambda_1 \frac{r}{r_o}}{\lambda_1 \frac{r}{r_o}}, \tag{3.12}$$

where A_1 and λ_1 are determined for different Biot numbers [100]. Equation 3.12 shows that the time dependence of temperature is the same at any radial position in the clast such that $ln(\theta(r,t)) \propto \tau$. Figure 3.8 demonstrates how Equation 3.12 scaling matches stage 2 temperature measurements.

I fit Equation 3.12 to our experimental measurements to determine Bi and H (e.g., Figure 3.8. To fit our data I approximate $r_o = (\frac{4}{3\pi} V_T)^{\frac{1}{3}}$, where V_T is the clast volume. I estimate r from the depth of the hole drilled for each thermocouple (Table 3.1). I use the maximum temperature measured during stage 2 to estimate T_i and to set the temporal location where $\tau = 0$. I neglect the temperature dependence of thermal diffusivity and conductivity and calculate effective thermal diffusivity as in section 3.5.4. Similarly, I estimate effective thermal conductivity according to $k_{eff} = k_w \phi + k_r(1-\phi) \approx 0.7$ W m^{-1}K^{-1}, where k_w is water thermal conductivity and k_r is rock thermal conductivity.

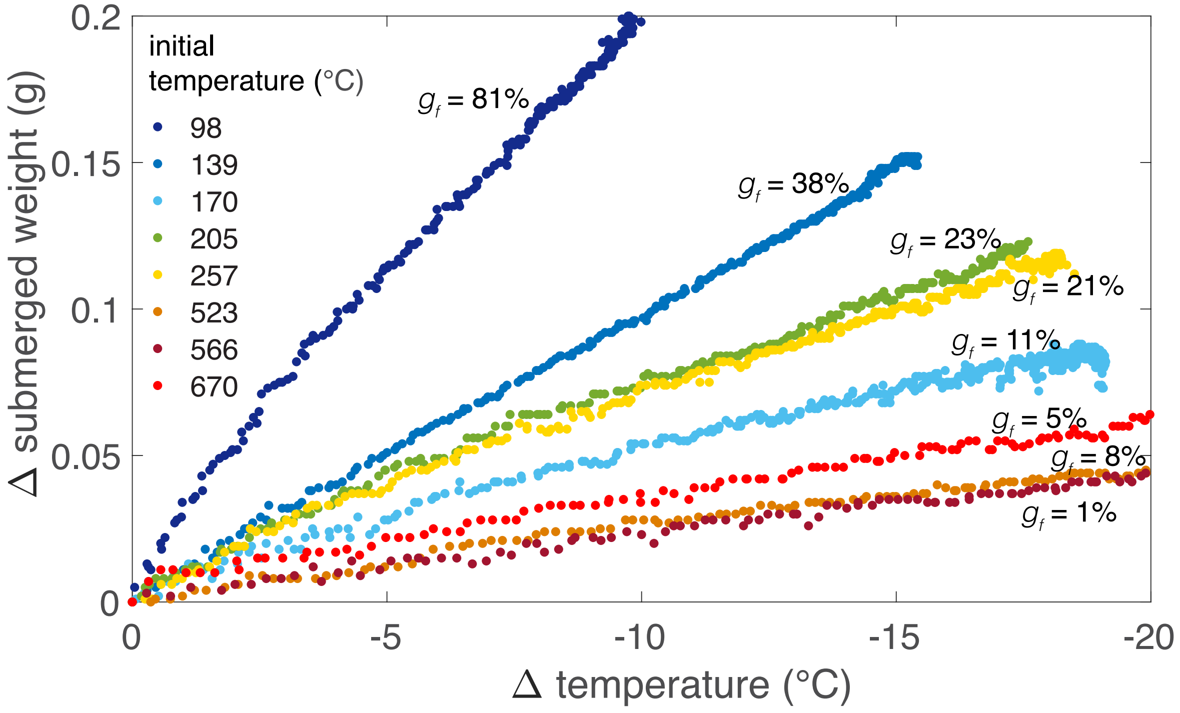

Figure 3.9: Stage 2 saturation of clast ML01. Submerged weight increases linearly as temperature declines during stage 2. The linear relationships between submerged weight and temperature indicate that the clast saturates as thermal contraction draws in liquid water during stage 2. I propose that $\frac{\Delta M_S}{\Delta T_r}$ increases with trapped gas content and use Equation 3.15 to solve for trapped gas content, g_f. I find that trapped gas content generally decreases as clast initial temperature increases.

I iteratively find the Biot number that fits Equation 3.12 to our temperature measurements for $\tau > 0.2$. Figure 3.8 shows how Equation 3.12 matches measurements of temperature as a function of time. Based on the fit between Equation 3.12 and our measurements, I estimate Bi and H (Table 3.1). I find Biot numbers and heat transfer coefficients in the range of $1 - 10$ and $20 - 350$ W m^{-2}K^{-1}, respectively (Table 3.1). By comparison, typical heat transfer coefficients are lower for pyroclasts cooling in air, ≈ 15 W m^{-2}K^{-1} [75] and much higher for steel, nickel, aluminum, and copper cooling in water, $\approx 10^3 - 10^4$ W m^{-2}K^{-1}, with H decreasing with the surface temperature of the metal [101].

3.5.5 Stage 2: Saturation

During stage 2 I find that clast submerged weight changes linearly with temperature (Figure 3.9). I propose that the linear relationship in Figure 3.9 reflects thermal contraction of internal fluids (primarily trapped air) and consequent ingestion of liquid water. That is, the total amount of trapped gas is conserved and the amount of liquid water increases as water fills the space made available by thermal contraction.

At constant pressure, the volumetric coefficient of thermal expansion

$$\alpha = \frac{1}{V_f}\frac{dV_f}{dT}, \tag{3.13}$$

demonstrates that fluid volume changes linearly with temperature, where V_f is fluid volume. Because the thermal expansion coefficient of air is an order of magnitude greater than that of water, I predict that clasts that contain more trapped air will contract more and ingest more water more per degree of cooling such that

$$\frac{dM_T}{dT_r} \propto g_f, \tag{3.14}$$

where T_r is the internal temperature at any radial position and $g_f = \frac{V_g}{\phi V_T}$ is the fraction of trapped gas within the pore space [80]. In Section 3.9.3 I derive a quantitative relation for the dependence of submerged weight with temperature on trapped gas volume

$$\frac{dM_T}{dT_r} = -V_T\phi\rho_l(\alpha_l - g_f\alpha_l + g_f\alpha_g), \tag{3.15}$$

where α_l and α_g are the thermal expansion coefficients for liquid water and air, respectively. Equation 3.15 includes effects from both liquid water and air contraction.

Figure 3.9 demonstrates how clast submerged weight scales linearly with temperature during stage 2. In Figure 3.9 I define $\Delta M_S = M_S(t) - M_S(t_{S2})$ and $\Delta T_r = T_r(t) - T_r(t_{S2})$ where t_{S2} is a time soon after the beginning of stage 2 (specifically t_{S2} is thirty seconds after the observed temperature maximum in stage 2).

I find that $\frac{dM_T}{dT_r}$, and thus trapped gas fraction g_f generally decrease with increasing clast initial temperature. The observation that that initially hotter clasts trap less gas is consistent with previous work which shows that trapped gas fraction decreases with increasing clast initial temperature [71, 80].

3.5.6 Estimating a stage 1 average cooling rate

Observations of liquid flux as a function of time show that the length of time until the stage 1 to stage 2 transition, t^*, increases as clast initial temperature increases (Figure 3.3). Here, based on results from all experiments, I propose that t^* increases linearly with clasts' initial thermal energy (Figure 3.10). An increase in t^* with clast initial thermal energy is consistent with the idea that clasts must cool below the boiling point to condense all internal steam and transition to stage 2.

I plot t^* as a function of clast initial thermal energy divided by clast surface area in Figure 3.10. Figure 3.10 shows a linear relationship that can be approximated by

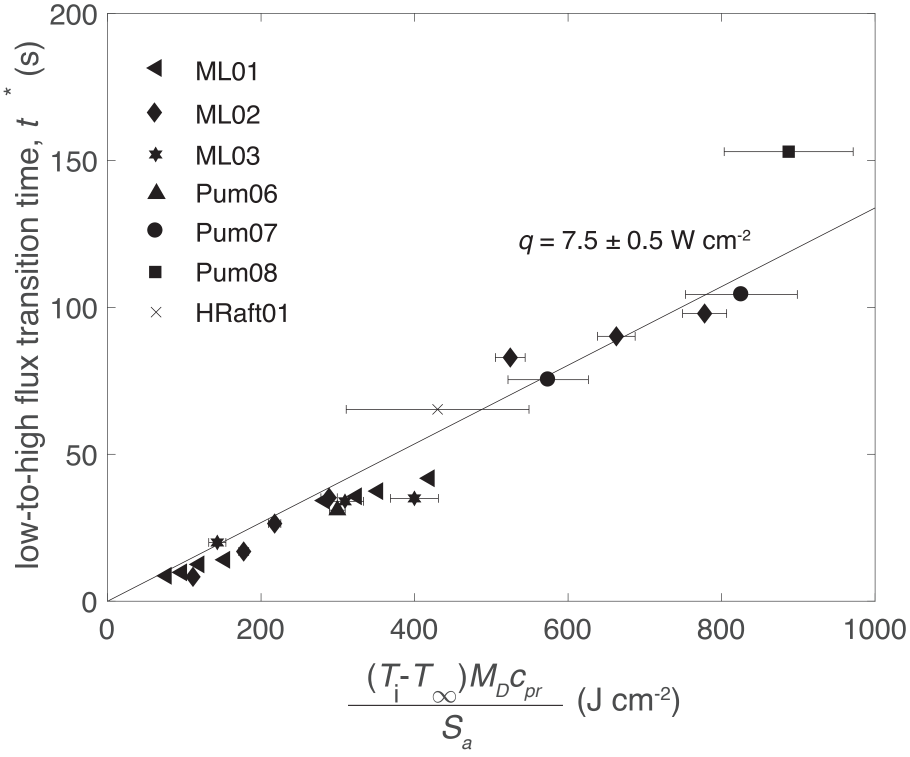

Figure 3.10: High-to-low liquid flux transition, t^*, as a function of clast initial thermal energy and surface area. Consistent with the concept that clasts must lose a sufficient amount of thermal energy to condense all internal steam and reach t^*, the linear relationship indicates that clasts experience the same time-integrated average rate of heat loss, $q = 7.5 \pm 0.5$ W cm^{-2}.

$$\underbrace{t^*}_{cooling\ time} = \underbrace{\frac{1}{q}}_{average\ heat\ flux} \underbrace{\frac{(T_i - T_\infty)c_{pr}M_D}{S_a}}_{initial\ heat\ content}, \tag{3.16}$$

where q is a fitted coefficient that represents heat flux in W cm^{-2}, c_{pr} is the heat capacity of the glass phase, M_D is clast dry mass, and S_a is clast surface area. The linear scaling in Equation 3.16 implies that the stage 1 to 2 transition occurs when a sufficient amount of heat has been lost and suggests that the clasts of different sizes, porosities, and initial temperatures, experience the same average heat flux during stage 1 such that q is the same for different clasts. From Figure 3.10, we estimate $q = 7.5 \pm 0.5$ W cm^{-2}.

Because I could not measure the submerged weight of very large clasts, we used high speed video and temperature measurements to determine t^* for these clasts (Pum07, Pum08, and HRaft01). Specifically, I determine the time at which clasts where submerged below water using the video. I use the temperature measurements to determine the time, t^*, based on the observation that local minima in internal temperature coincide with t^*. Uncertainty in the surface area of the clasts generates the largest uncertainty in the right side of Equation 3.16 and therefore q. I approximate surface area by letting S_a be the average of the spherical equivalent surface area and the elliptical equivalent surface area, $S_a^{ellipsoid} = 4\pi[\frac{(r_1r_2)^{1.6}+(r_2r_3)^{1.6}+(r_2r_3)^{1.6}}{3}]^{\frac{1}{1.6}}$, where r_1, r_2, and r_3 are the axes dimensions that I measure on each clast (Figure 3.16).

The t^* timescale is significant because it represents the time over which a clast is at least partially above the boiling point and contains steam. Our result that different clasts have the same average heat flux value during stage 1 is useful because this constant q value can be applied in models of pyroclast dispersal and plume dynamics.

3.5.7 Estimating an average stage 1 liquid flux

I observe that liquid flows into clasts at the same average rate for very hot clasts (Figure 3.3). That is, water enters clasts at the same rate during different experiments conducted on the same clast and the liquid flux rate is relatively constant through time (Figure 3.3). Here I propose a method to estimate the average stage 1 liquid flux, Q_l, based on our findings that saturation is governed by heat loss and that there is an average rate of heat loss, q. Specifically I propose

$$\frac{Q_l}{S_a} = \frac{q}{\phi L}, \tag{3.17}$$

where S_a is clast surface area, and L is the latent heat of condensation. Equation 3.17 reflects a balance between the rate of liquid flow coming into the clast and the rate of condensation. Equation 3.17 does not include thermal contraction effects or account for the presence of non-condensable gas. Equation 3.17 applies when the initial thermal energy of a clast is high enough ($T_{eq} > 100°\text{C}$) such that, after ingesting water through all of its pore space, a clast must conduct heat out in order to condense water vapor (e.g., Equation 3.7).

I compare Equation 3.17 to average stage 1 saturation rates (measured for clasts with initial temperatures $> 458°\text{C}$) in Figure 3.11. I do not report saturation rates for our largest clasts (Pum 07, Pum08, and HRaft01), because these clasts were too buoyant in water to measure their submerged weight with our set-up.

I find that Equation 3.17, where I use $q = 7.5\pm0.5$ W cm^{-2} and S_a as described in section 3.5.6, matches the average stage 1 saturation rates measured in our experiments. While I do not validate Equation 3.17 for larger clasts, Equations 3.16 and 3.17 may prove useful in models of submarine pyroclast dispersal because they provide a way to estimate average saturation and cooling rates based on measurable quantities such as clast porosity, size, and initial temperature.

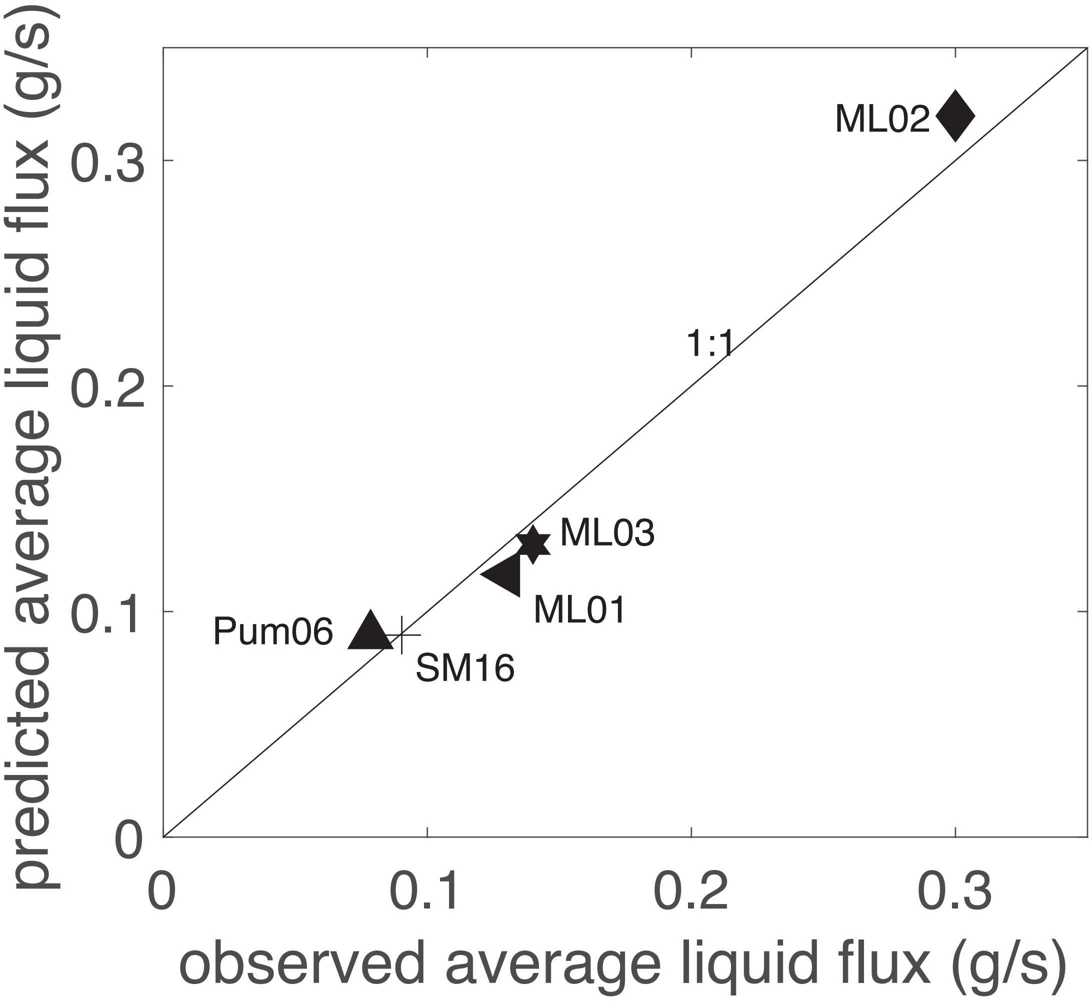

Figure 3.11: Observed time-averaged liquid flux versus modeled time-averaged liquid flux (Equation 3.17). I propose that, because model Q_l predictions match observed values, that I can use Equation 3.17 to estimate average rates of liquid flow into clasts and where liquid flow balances steam condensation. The line is 1:1.

3.6 Discussion

In the preceding sections I presented observations of, and quantitative models for, pumice cooling and saturation. I found that hot pumice cools in two-stages. In stage 1, water ingestion both accelerates, and is limited by, clast cooling. I argued that during stage 1b heat transfer, rather than permeability, controls saturation and fit a modified Stefan model to observations of pumice saturation. I proposed that stage 2 cooling and saturation is controlled by conduction and thermal contraction, respectively. Finally, I argued that the stage 1 to stage 2 transition occurs when sufficient thermal energy is lost and proposed a model to estimate the transition timescale, t^*, as well as average rates of heat loss, q, and liquid water saturation, Q_l.

Here I discuss how our experimental results and models can be applied to submarine eruptions and the limitations associated with extrapolation to parameter spaces not explored in this study but that are relevant for the submarine environment.

3.6.1 Experimental and model limitations

Submarine eruptions can differ from the experiments presented here in many important ways. Submarine clasts experience changes in pressure as they rise or fall through the water column leading to further exsolution, expansion or contraction of the vapor, and changes in the water phase change temperature. Clasts may continue to vesiculate in the water column and therefore clast permeability and vesicularity may not be static. Liquid water infiltration may not be uniform as assumed in our 1-D models and we did not explicitly consider multiphase effects such as liquid and vapor counter flows. The vapor within submarine clasts may be entirely condensable such that clasts must rise to the ocean surface to exchange gas with the atmosphere to be able to float after cooling. Conversely, I did not explicitly model the time-varying and heterogeneous distribution of non-condensable gases. While I estimated average heat and saturation fluxes for pyroclasts (sections 3.5.6 and 3.5.7), these fluxes are likely not constant over time. Finally, I examined the dynamics of initially air-filled pyroclasts while most submarine pyroclasts are filled with condensable water vapor. Nevertheless, because I argue hot pyroclasts convert ingested water to steam, many of these results can be extrapolated to the steam-filled case (e.g., stage 1b). This extrapolation should be taken with caution, however; for example Equation 3.16 should be modified to take the thermal energy of the water vapor into account. Our experimental set-up precluded the examination of the processes listed and they were not explicitly accounted for in our models. Consideration of these and other processes is needed, however, to model submarine eruption dynamics [11] and efforts are underway to couple pumice buoyancy evolution to clast vesiculation and an ascent model [102]. The present experimental data may prove useful to validate such numerical models.

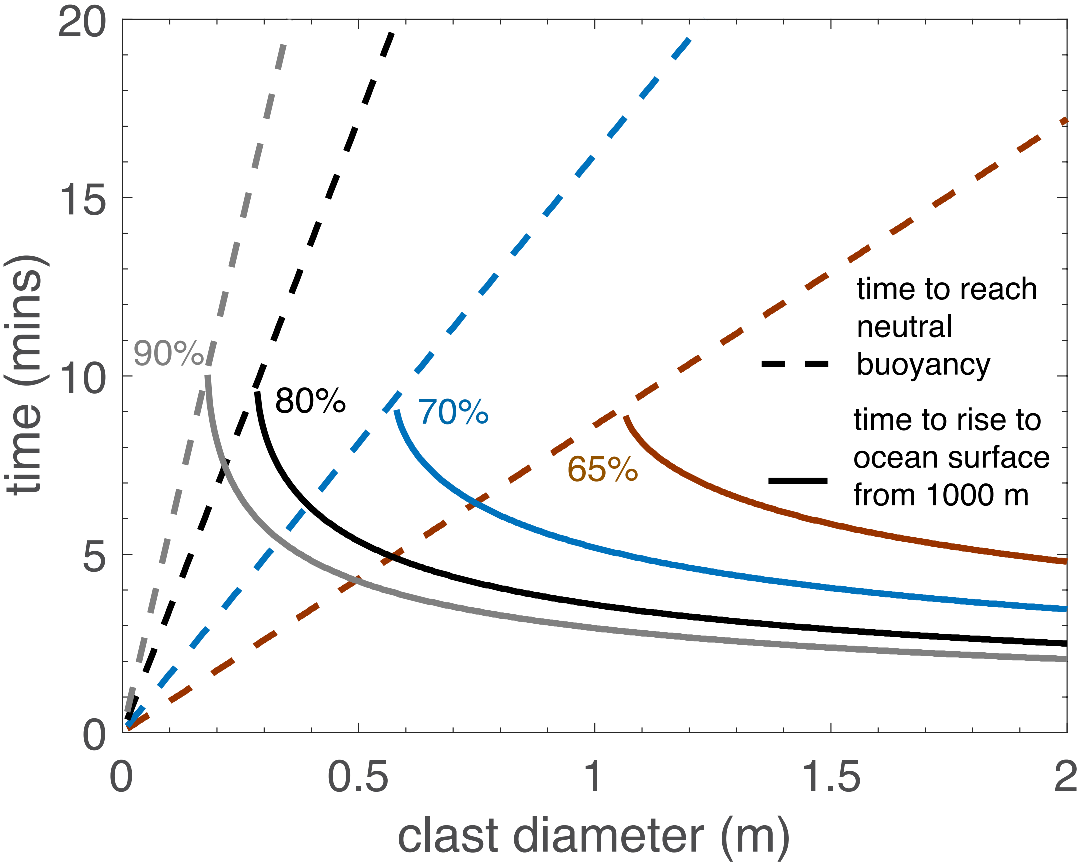

Figure 3.12: Time for a clast to reach neutral buoyancy (dashed lines) and time to rise to the ocean surface from 1000 meter depth (solid lines) as functions of clast size and porosity. We model clast saturation as a function of heat loss and steam condensation (Equations $3.17 - 3.19$). We estimate clast rise times using Equation $(3.19 - 3.21)$. From this figure, we can estimate how long a water-vapor filled clast will remain buoyant (excluding the effects of decompression and vapor expansion) and minimum clast sizes required to reach the surface (intercepts of dashed and solid lines). Porosities are listed in percent.

3.6.2 Application to submarine eruptions

These observations of pyroclast cooling and saturation can inform our understanding of submarine eruption dynamics. For example, submarine eruptions are known to produce giant (> 1 m diameter) pumice [e.g., 12, 14, 103, 104]. Depsite observations that hot lapilli-size clasts often sink quickly in water [e.g., 70–72], it has been proposed that pumice, particularly large pumice, can remain buoyant long enough to reach the ocean surface [e.g., 105–107]. When clasts do become water-logged, it is thought that clasts sink slowly to the seafloor such that they may sort based on clast size, be dispersed far from their vent of origin, and reach the seafloor without breaking [e.g., 108, 109]. Here we use Equation 3.17 to estimate how long steam-filled pumice can remain buoyant and test the idea that clasts can rise far above the seafloor.

I assume that clasts saturate as a result of heat loss, do not contain non-condensable gases, do not experience decompression leading to expansion of internal vapor, and begin with vapor in all of their pore space. To determine the time until neutral buoyancy I first calculate the fraction of pore space filled with liquid water, ω, as a function of time

$$\omega(t) = \frac{Q_l t}{\phi V_T}, \tag{3.18}$$

where I use Equation 3.17 to estimate Q_l. I calculate clast density, ρ_c according to

$$\rho_c(t) = (1-\phi)\rho_r + \phi\omega(t)\rho_l \tag{3.19}$$

and determine the water saturation, ω^*, at which clasts reach neutral buoyancy such that $\rho_c = \rho_l$ (Figure 3.12). Figure 3.12 shows how buoyancy time increases with clast size and porosity. For example, I find that a 0.5 m and 80 percent porosity clast will remain buoyant for ≈ 20 minutes and 1 m diameter and 70 percent porosity clast will remain buoyant for ≈ 16 minutes. Because Equations $3.17 - 3.19$ do not include the effects of vapor expansion associated with decompression, I expect that the buoyancy times plotted in Figure 3.12 represent lower bounds on the longevity of clast rise through the water column.

I compare clast buoyancy times to clast rise times to the ocean surface from a depth of 1000 m (Figure 3.12). I estimate clast rise velocities, u, according to

$$u = \sqrt{\frac{8(\rho_l - \rho_c(t))g r_o}{3\rho_l C_d}}, \tag{3.20}$$

and rise distance as

$$L^{rise} = \int u dt, \tag{3.21}$$

where ρ_c is clast density, ρ_l is liquid water density, g is gravity, r_o is clast radius, and $C_d = 0.3$ is a drag coefficient batchelor1970. By combining Equations $3.19 - 3.21$ I determine the time at which a clast saturating at rate, Q_l would reach the surface from 1000 m depth (Figure 3.12).

Figure 3.12 shows how, based on Equations 3.18 – 3.21, I can determine minimum clast sizes required to reach the surface from a depth of 1000 m: 1.1, 0.6, 0.3, and 0.2 m diameter for pyroclast porosities of 0.65, 0.7, 0.8, and 0.9, respectively (intercepts of dashed and solid lines). Regardless of clast size and porosity, a clast can rise from a depth of 1000 m for $\approx 9 - 10$ minutes before either reaching the surface or starting to sink (Figure 3.12)

Once pyroclasts reach the surface they can float and form pumice rafts as a result of non-condensable gas trapping [80] and thus have the potential to be dispersed long distances. When clasts reach the surface full of steam, floatation requires that air replaces steam in clast pore spaces before the clasts are cool [e.g., 110]. Our models not only support the arguments that large clasts are able to reach the surface [e.g., 105, 111, 112] but also provide quantitative constraints on that timing. The recent 2012 eruption of Havre submarine volcano demonstrates how porous volcanic material can be partitioned into both floating and sinking components [14] and our models may be useful for understanding those sorting processes.

Conceptual models have also attributed the buoyancy of pyroclasts to steam sheathes that develop around their exteriors. I did not observe, however, steam sheathes in any of our experiments because liquid water can enter the pores and cool the surface below the boiling temperature. Rather, I propose that steam occupies the clast interiors - the warmest regions of the clasts.

Together, my experimental results and models suggest that, because saturation is limited by cooling and condensation, pyroclasts often remain hot and buoyant long-enough to reach the surface. My clast-scale cooling and saturation models provide tools for understanding the eruption dynamics of events such as the 2012 eruption of Havre volcano - noting that additional physics, such as the effects of pressure changes, should be better resolved to fully understand the evolution of clast buoyancy.

3.7 Conclusions

Pyroclast cooling and saturation are important for understanding submarine eruption dynamics and pyroclast dispersal. In this study I used laboratory experiments to examine, and develop models for, clast-scale cooling and saturation.

I found that hot pumice cools in several stages (Figure 3.4). At first (stage 1a), gas bubbles flow out as water enters the clasts. I found that the saturation of clasts with initial temperatures below the boiling point fits a Darcy model for flow where permeability matters (section 3.5.1). By comparison, I proposed that hot clasts convert ingested water to vapor (stage 1b) and that saturation continues as clasts cool, condense steam, and thereby generates a pressure gradient to draw in liquid water. As a result, I argued that heat loss, rather than permeability, controls the saturation of very hot clasts. I tested this interpretation by comparing our experimental data to a modified Stefan model in section 3.5.3.

I observed that there are abrupt transitions in the rate of liquid water flow into the clasts that corresponds to inflection points in temperature (Figure 3.4). I argue that these shifts represent changes in processes and proposed that heat conduction controls stage 2 cooling and the thermal contraction of non-condensable vapor controls stage 2 saturation. I tested our interpretations for stage 2 processes with quantitative models in sections 3.5.4 and 3.5.5.

The stage 1 to stage 2 transition is defined by a shift from a high-to-low liquid flux into the clasts and I argued that this transition is indicative of the time at which all internal water vapor has condensed within the clasts. Based on a linear scaling between stage transition time, t^*, and initial thermal energy of each clast, I proposed that t^* occurs when clasts lose sufficient thermal energy and that clasts lose heat at the same time-averaged rate of $q = 7.5 \pm 0.5$ W cm^{-2}.

Building from the finding that clasts lose heat an average rate, q, and my arguments that the rate of liquid flow into clasts balances the rate of condensation during stage 1b, I estimated time-averaged rates of liquid flow into clasts (Equation 3.17). I found that predicted values for average liquid flux, Q_l match experimentally measured values (Figure 3.11). As a result, I used our average liquid flux model (Equation 3.17) to estimate the time it takes water-vapor filled pyroclasts to reach neutral buoyancy due to heat loss and as a function of clast size and porosity (Figure 3.12). I found that pyroclasts containing water-vapor can stay buoyant for minutes to hours, often long enough to rise far above the ocean floor.

While these experiments and models do not include many processes relevant for submarine eruptions, such as decompression effects, they can provide insight into submarine eruption dynamics. For example, the finding that pyroclast saturation depends on heat loss, rather than permeability, informs our understanding of pyroclast dispersal and partitioning into floating and sinking components. The assessments of time-averaged heat and liquid flux values may be useful in submarine plume models. Furthermore, these experimental results may help validate models that include important processes neglected in this study. In general, the study results support what was already acknowledged - that large and hot pyroclasts saturate slowly as they cool [e.g., 11, 105, 108, 110–112]. The models and data presented here provide a quantitative framework, however, for understanding the mechanics of cooling and saturation and demonstrate that high porosities and phase-changes lead to complex behaviors.

3.8 Acknowledgements

This study was inspired, in part, by observations of Havre submarine volcano made during the MESH cruise (https://web.whoi.edu/mesh/). I specifically thank James White who has emphasized the importance of understanding eruptive heat transfer and who has shared insights into submarine volcanic processes. I am grateful to Ryan Cahalan and Joe Dufek for the informative discussions on pyroclast cooling and saturation in water and for conversing with me with the goal to use experiments to validate numerical models currently in development. Support for this study was provided by the US EAR 1447559. Finally, I thank Barbara Tripoli, Aaron Tran, and Stephen Breen for their assistance with the experimental

Table 3.3: Notation

M_S	submerged pumice weight	M_T	total pumice mass
M_D	dry pumice mass	V_T	total pumice volume
V_l	liquid water volume	V_f	internal fluid volume
V_g	non-condensable gas volume	Q_l	liquid flux
Q_o	initial liquid flux	v	liquid infiltration velocity
t	time	t^*	high-to-low liquid flux transition time
t_{adv}	advective timescale	t_{cond}	diffusive timescale
ρ_l	liquid water density	ρ_r	glass density
ρ_c	clast density	T	temperature
T_i	initial temperature	T_f	condensation temperature
T_{eq}	equilibrated temperature	T_∞	fluid bath temperature
H_r	thermal mass	$\theta(r,t)$	dimensionless temperature
ξ	water saturation coefficient	c_p	heat capacity
c_{pr}	heat capacity of glass	c_{pl}	heat capacity of liquid water
L	latent heat of condensation	ϕ	porosity
γ	surface tension	κ	permeability
μ	viscosity	r_o	clast radius
r_s	condensation front position	r	radial position
r_t	thermocouple radial positin	S_a	surface area
S_a^c	condensation front surface area	$S_a^{ellipsoid}$	ellipsoid equivalent surface area
d	pore throat diameter	Bi	Biot number
St	Stefan number	Pe	Peclet number
H	heat transfer coefficient	k_{eff}	effective thermal conductivity
k_w	liquid water thermal conductivity	k_r	glass thermal conductivity
τ	non-dimensionalized time	τ^*	non-dimensionalized time
D_{eff}	effective thermal diffusivity	D_w	water diffusivity
D_r	glass diffusivity	A_n	coefficient
C_1	coefficient	λ_n	transcendental equation roots
α	thermal expansion coefficient	α_g	thermal expansion coefficient of gas
α_l	thermal expansion coefficient of liquid	g_f	fraction of trapped gas within the pore space
q	average heat flux	w	pore fraction filled with liquid water
C_d	drag coefficient	g	gravity
L^{rise}	rise distance	u	clast rise speed
R	dimensionless radial position	R^*	dimensionless radial position
S	dimensionless interface position	N	number of grid points

set-up and Melissa Rotella and Colin Wilson for providing the Havre raft samples. Data and code used in this study will be made available on Vhub.

3.9 Appendix

3.9.1 Conductive Cooling on a Sphere

Consider a radially symmetric sphere that cools by conduction and convective heat transfer at its outer edge. To determine the temperature distribution $T(r,t)$ inside a sphere I write the 1-D heat equation in spherical coordinates and specify initial and boundary conditions:

$$\frac{\partial T}{\partial t} = D_{eff}[\frac{2}{r}\frac{\partial T}{\partial r} + \frac{\partial^2 T}{\partial r^2}]|_{0<r<r_o} \tag{3.22}$$

$$\frac{\partial T}{\partial r} = 0|_{r=0} \tag{3.23}$$

$$-k_{eff}\frac{\partial T}{\partial r} = H(T - T_\infty)|_{r=r_o} \tag{3.24}$$

$$T(r,0) = T_i \tag{3.25}$$

where T_∞ is background temperature, T_i is initial temperature, t is time, r is radial position, r_o is sphere radius, k_{eff} is effective thermal conductivity, D_{eff} is effective thermal diffusivity, and H is the heat transfer coefficient. The governing equations can be non-dimensionalized by defining $R = \frac{r}{r_o}$ to be dimensionless radius, $\tau = \frac{D_{eff}t}{r_o^2}$ to be dimensionless time, $\theta(r,t) = \frac{(T(r,t)-T_\infty)}{(T_i-T_\infty)}$ to be dimensionless temperature, and by recalling that $\mathrm{Bi} = \frac{Hr_o}{k_{eff}}$,

$$\frac{\partial \theta}{\partial \tau} = \frac{1}{R}\frac{\partial}{\partial R}(R\frac{\partial \theta}{\partial R})|_{0<R<1} \tag{3.26}$$

$$\frac{\partial \theta}{\partial R} = 0|_{R=0} \tag{3.27}$$

$$\frac{\partial \theta}{\partial R} + \mathrm{Bi}\theta = 0|_{R=1} \tag{3.28}$$

$$\theta(R,0) = 0. \tag{3.29}$$

The exact solution to Equations $3.26 - 3.29$ is given by Equation 3.11 and an approximate solution is given by Equation 3.12. In section 3 I compare measurements of clast internal temperature to solutions to Equations $3.26 - 3.29$ to determine stage 2 heat transfer coefficients.

3.9.2 Modified Stefan Problem

Here I write the governing equations for the inward propagation of a condensation front in a conductively cooling sphere [e.g., 97, 98, 113] and we add an advective term to account for water flow into the clasts. Consider a sphere of radius r_o composed of a homogeneous fluid with initial temperature T_f, where T_f is the phase change temperature, and surrounded by a bath of subcooled fluid of constant temperature T_∞ (Figure 3.6). I write 1-dimensional equations that govern sphere cooling by conduction and advection and propagation of an internal condensation front as:

$$\frac{\partial T}{\partial t} = D_{eff}[\frac{2}{r}\frac{\partial T}{\partial r} + \frac{\partial^2 T}{\partial r^2}] - \frac{\partial r_s}{\partial t}\frac{\partial T}{\partial r}|_{r_s<r<r_o} \tag{3.30}$$

$$-k_{eff}\frac{\partial T}{\partial r} = \rho\phi L\frac{\partial r}{\partial t}|_{r=r_s} \tag{3.31}$$

$$T = T_f|_{r<r_s} \tag{3.32}$$

$$-k_{eff}\frac{\partial T}{\partial r} = H(T - T_\infty)|_{r=r_o} \tag{3.33}$$

$$T(r,0) = T_f \tag{3.34}$$

where k_{eff} is effective thermal conductivity, $r_s(t)$ is the position of the phase change front, L is latent heat, and H is the heat transfer coefficient. By defining the following dimensionless variables $\tau = \frac{D_{eff}t}{r_o^2}$, $R^* = 1 - \frac{r}{r_o}$, $S = 1 - \frac{r_s}{r_o}$, $\theta(r,t) = \frac{(T(r,t)-T_\infty)}{(T_i-T_\infty)}$, $St = \frac{c_p(T_f-T_\infty)}{\phi L}$, and $Bi = \frac{Hr_o}{k_{eff}}$, I can write the model equations as

$$\frac{\partial \theta}{\partial \tau} = \frac{2}{R^*-1}\frac{\partial \theta}{\partial R^*} + \frac{\partial^2 \theta}{\partial R^{*2}}] - \frac{\partial S}{\partial \tau}\frac{\partial \theta}{\partial R^*}|_{0<R^*<S} \tag{3.35}$$

$$St\frac{\partial \theta}{\partial R^*} = \frac{\partial R^*}{\partial \tau}|_{R^*=S} \tag{3.36}$$

$$\frac{\partial \theta}{\partial R^*} = \mathrm{Bi}\theta|_{R^*=0} \tag{3.37}$$

$$\theta = 1|_{S<R^*<1} \tag{3.38}$$

$$\theta(r,0) = 1 \tag{3.39}$$

I solve Equations $3.35 - 3.39$ numerically and using a finite difference approximation and moving grid approach. We adopt the stability condition used by [98]

$$\frac{\tau N^2}{R_N^*} \leq \frac{1}{2}, \tag{3.40}$$

where N is the number of points in the grid. I let $n = 0$ at $R^* = 0$ and $n = N$ at $R^* = S$, where S is the position of the condensation front. I use a grid with ≈ 25 grid points as did [98].

I test this model by comparing the solution (without advection) to an analytical solution by [97]. I also write out and solve a similar set of equations for a planar geometry and compare those solutions to our data as well. While this model includes cooling effects from fluid flow, I do not explicitly include the effects of heat transfer among multiple phases and we assume that steam in the clast interior is at the boiling temperature. I use values derived in section 3.5.4 to estimate H.

3.9.3 Derivation of equation for trapped gas content

Here I derive an equation that relates change in mass with temperature to changes in fluid fractions within a clast. I can write the total mass of a partially saturated pumice as,

$$M_T = M_P + \rho_g V_g + \rho_l V_l, \tag{3.41}$$

where M_P is the mass of the rock phase (pumice dry mass), ρ_g is the gas density, V_g is the gas volume in the pumice, ρ_l is the liquid density, V_l is the liquid volume with the pumice clast. Because pumice internal volume is conserved, $V_T\phi = V_l + V_g$, where V_T is the total pumice volume and ϕ is porosity. If the mass of non-condensable gas within a pumice doesn't change during stage II due to gas trapping and by writing $V_l = (V_T\phi - V_g)$ then the derivative of Equation 3.41 with respect to temperature is

$$\frac{dM_T}{dT} = \frac{d(\rho_l(V_T\phi - V_g))}{dT}. \tag{3.42}$$

The definition of thermal expansion coefficients (Equation 3.13) can be combined with Equation 3.42 such that

$$\frac{dM_T}{dT} = (V_T\phi - V_g)(-\rho_l\alpha_l) + \rho_l(-\alpha_g V_g). \tag{3.43}$$

Equation 3.43 can be further simplified by letting $g_f = \frac{V_g}{\phi V_T}$ be the fraction of trapped gas within the pore space such that

$$\frac{dM_T}{dT_r} = -V_T\phi\rho_l(\alpha_l - g_f\alpha_l + g_f\alpha_g), \tag{3.44}$$

where T_r is the temperature at any radial position. I can estimate $\frac{dM_T}{dT}$ by fitting a linear slope to plots of temperature versus submerged weight and then use Equation 3.44 to estimate trapped gas fraction (Figure 3.9). I can use temperature from any radial position, T_r, because in a conductively cooling body the time dependence of internal temperature at any radial position is the same as that at the center point [99].

3.9.4 Supplement

Table 3.4: Description of Experiments

Date	**clast name**	**approx. initial temperature °C**	**coolant**
03/09/17	SM16	500	water
03/20/17	Pum06	500	water
06/23/17	Pum06	500	water
06/30/17	ML02	500	water
06/30/17	ML01	500	water
3/07/2017	ML02	200	water
07/03/17	ML01	200	water
07/05/17	ML02	90	water
07/05/17	ML01	90	water
07/06/17	ML02	700	water
07/06/17	ML01	700	water
07/10/17	ML01	260	water
07/11/17	ML02	65	air
07/12/17	ML02	20 (ambient)	water
07/31/17	ML02	600	water
07/31/17	ML01	600	water
08/03/17	ML02	150	water
08/03/17	ML01	150	water
08/05/17	ML02	120	water
08/05/17	ML01	120	water
08/28/17	ML01	20 (ambient)	water
08/28/17	ML02	500	air
08/28/17	ML02	260	water
08/29/17	ML01	500	air
08/29/17	ML01	550	water
08/30/17	ML03	260	water
08/31/17	ML03	550	water
10/5/17	ML03	620	water
10/17/17	Pum07	720	water
10/17/17	ML03	720	water
10/20/17	Pum08	530	water
10/20/17	Pum07	530	water
10/23/17	Hraft01	530	water

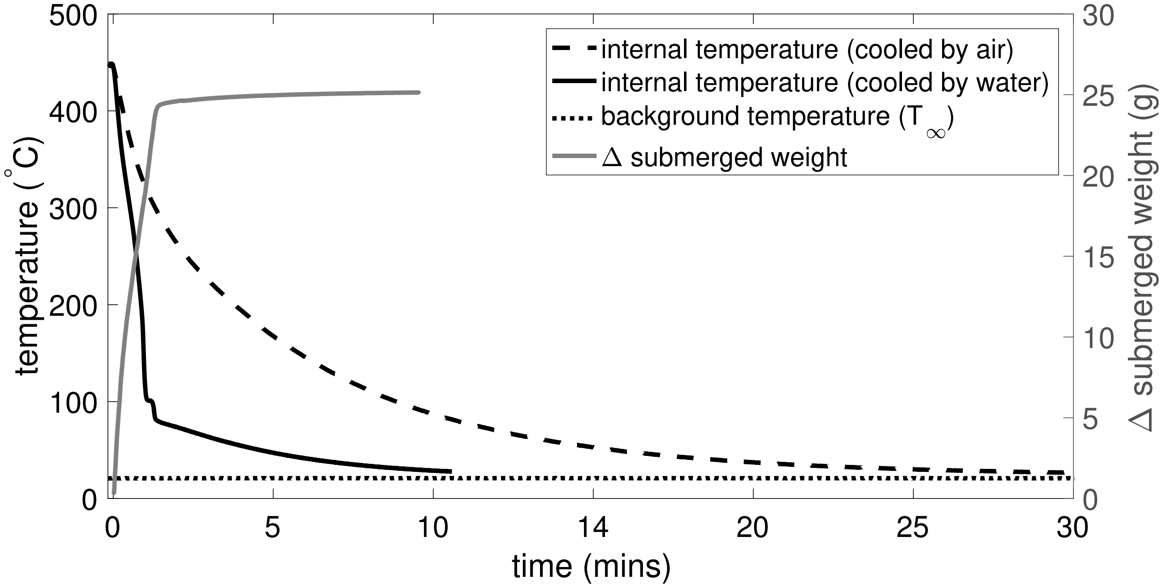

Figure 3.13: Comparison between pumice cooling in water versus air. Representative clast ML02 cools faster in water compared to air. I also plot ΔM_S that corresponds to the temperature measurements taken in water.

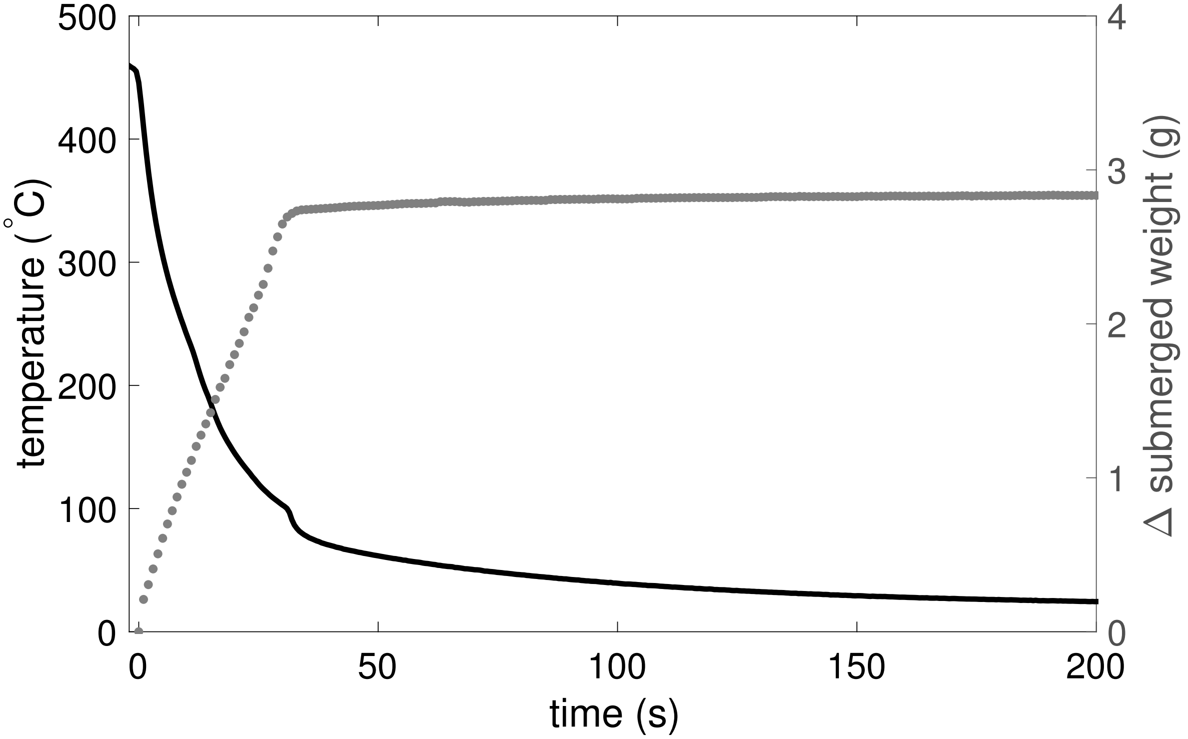

Figure 3.14: Cooling and saturation of clast Pum06 in water. I observe an inflection point in internal temperature when $T = 100°\text{C}$.

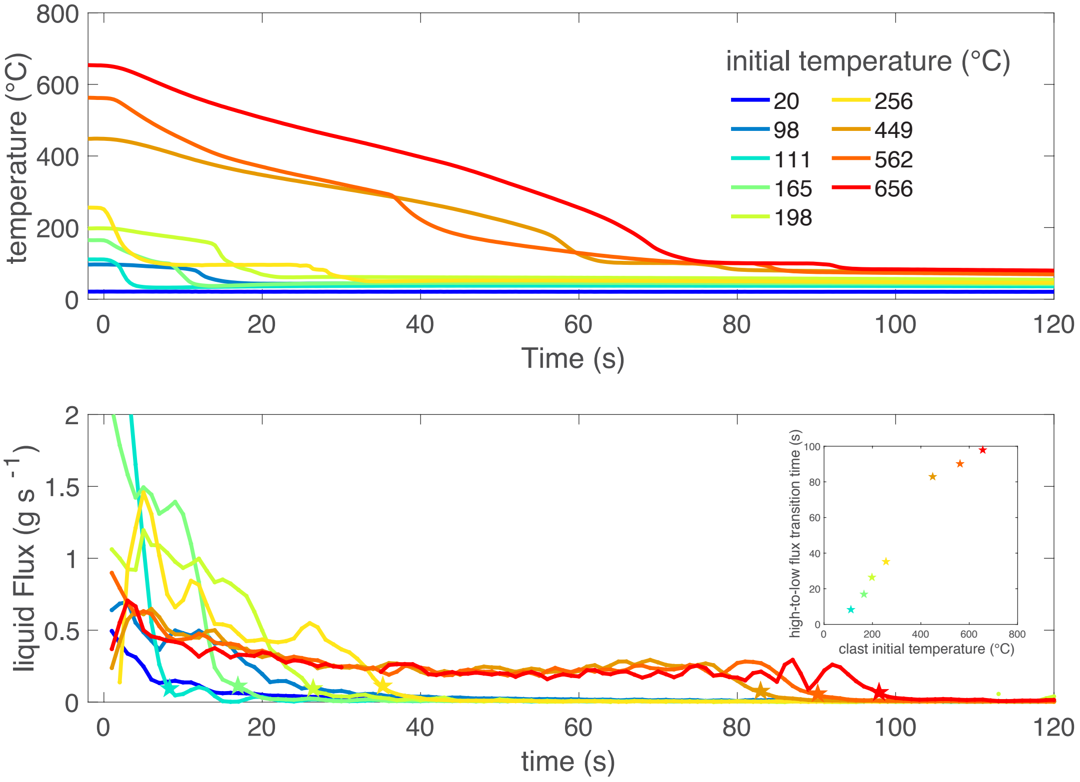

Figure 3.15: Effects of initial temperature on cooling and saturation. (A) Internal temperature of clast ML02 as a function of time. (B) Liquid flux (g s^{-1}) into the clasts as a function of time. Clasts with initial temperatures below 100°C exhibit the lowest liquid fluxes. Otherwise, initial liquid flux decreases with increasing initial clast temperature. All clasts with initial temperatures above 100°C exhibit sharp high-to-low liquid flux transitions (marked with stars). The inset shows how the timing of the high-to-low liquid flux transition increases with clast initial temperature.

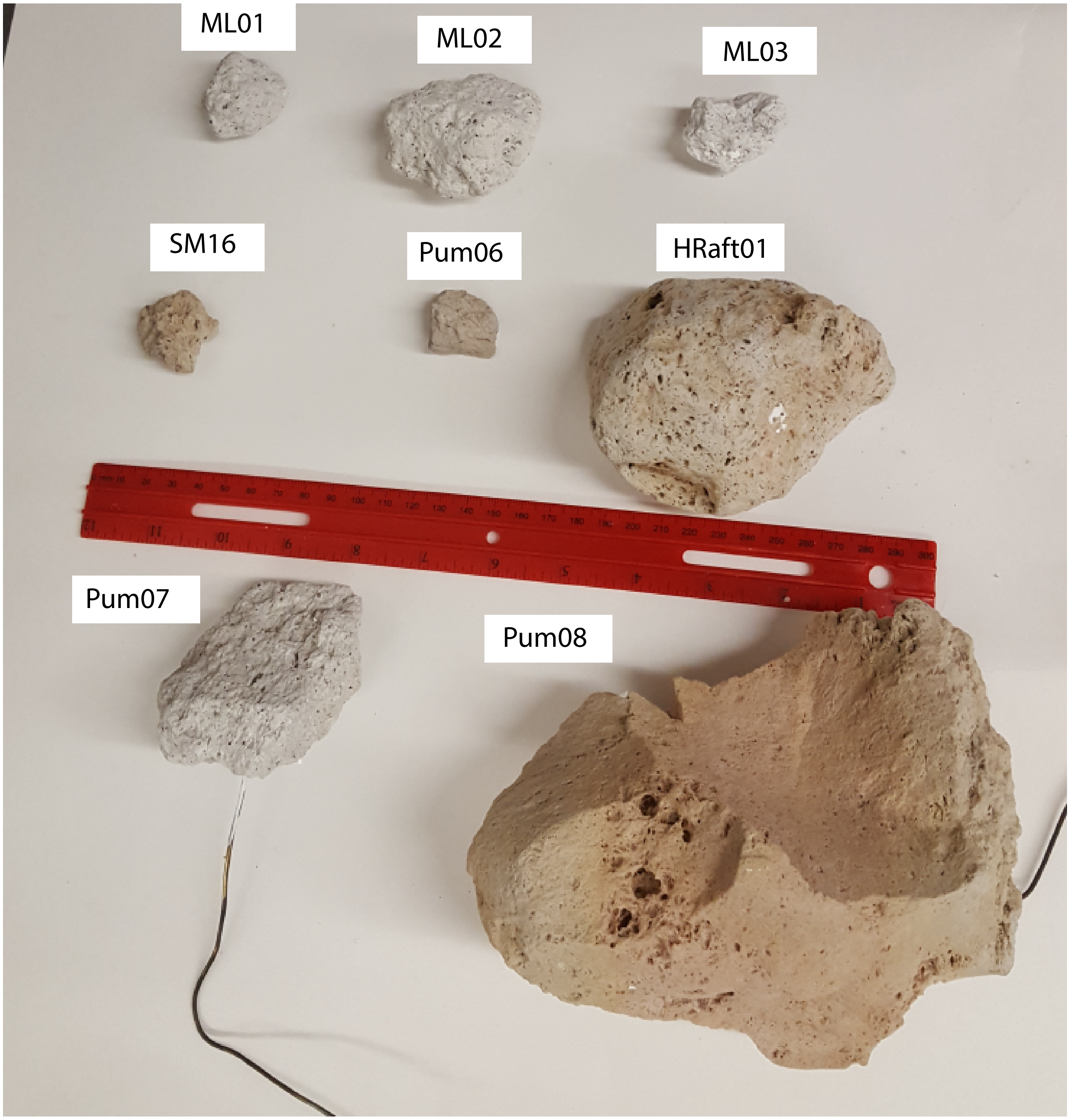

Figure 3.16: Pyroclasts used in this study

Chapter 4

Trapped bubbles keep pumice afloat and gas diffusion makes pumice sink

This chapter was previously published in Fauria, K.E., Manga, M., and Wei, Z., *Earth and Planetary Science Letters* **460**, 50 –59, (2017). doi:10.1016/j.epsl.2016.11.055

4.1 Summary

Pumice can float on water for months to years long enough for pumice to travel across oceans and facilitate the spread of species. Long-lived pumice floatation is unexpected, however, because pumice pores are highly connected and water wets volcanic glass. As a result, observations of long floating times have not been reconciled with predictions of rapid sinking. We propose a mechanism to resolve this paradox the trapping of gas bubbles by water within the pumice. Gas trapping refers to the isolation of gas by water within pore throats such that the gas becomes disconnected from the atmosphere and unable to escape. We use X-ray microtomography to image partially saturated pumice and demonstrate that non-condensable gas trapping occurs in both ambient temperature and hot (500°C) pumice. Furthermore, we show that the size distribution of trapped gas clusters matches predictions of percolation theory. Finally, we propose that diffusion of trapped gas determines pumice floatation time. Experimental measurements of pumice floatation support a diffusion control on pumice buoyancy and we find that floatation time τ scales as $\tau \propto \frac{L^2}{D\theta^2}$ where L is the characteristic length of pumice, D is the gaswater diffusion coefficient, and θ is pumice water saturation. A mechanistic understanding of pumice floatation is a step towards understanding how pumice is partitioned into floating and sinking components and provides an estimate for the lifetime of pumice rafts in the ocean.

4.2 Introduction

Pumice is a highly vesicular volcanic rock with a porosity high enough that it can float. Rafts of volcanic pumice can transit lakes and oceans and circle the globe [e.g., 78, 114–116]. For example, pumice from the 1952 eruption of Volcn Barcena on Isla San Benedicto, 600 km west of Mexico, floated for at least 560 days and drifted over 8700 km [114]. The 2012 eruption of Havre submarine volcano created a 1.5 km^3 pumice raft that spread over 550,000 km^2 within three months [12, 13]. Pumice rafts have been shown to facilitate the dispersal of species such as barnacles, corals, algae, and gastropods [117] because marine organisms grow on, and ocean currents advect, pumice [78, 114, 118]. While pumice rafts are relatively common and it is well known that ambient temperature pumice can float for long periods of time, the enduring buoyancy of pumice is surprising because pumice pores are almost entirely connected and water wets pumice [70, 82]. Quantitative models for pumice saturation predict that ambient temperature pumice should sink orders of magnitude more rapidly than is observed [82]. The floatation time discrepancy between observations and the Vella and Huppert [2007] model suggests that simple gas displacement by an infiltrating water front is not sufficient to explain why ambient temperature pumice can float for years.

By comparison to ambient temperature pumice, hot pumice (e.g., > 300°C) sinks almost immediately and the tendency for air-filled pumice to sink increases with pumice temperature [18, 70–72]. Rapid water ingestion by hot pumice has been attributed to cooling-induced gas contraction [70, 71, 108] and hydrodynamic instabilities due to steam generation [18]. Air-filled hot pumice placed in water does not, however, completely saturate even at high (500°C) temperatures [71]. As a result, we wish to understand how gas remains within initially hot pumice and what differences and similarities exist between saturation of ambient temperature and hot non-condensable gas filled pumice.

Pumice, with porosities of 50 to > 90 percent, is a porous medium. Water saturation of pumice is an example of two-phase flow in porous media and requires the replacement of a defending fluid (air or magmatic gases) with an invading fluid (liquid water). Two-phase flow in porous media has been widely studied in the context of the vadose zone, oil recovery, CO_2 sequestration, and gas sparging. In addition, water infiltration of pumice is a manifestation of a particular type of two-phase flow, imbibition, because water is the wetting phase. During imbibition the arrangement of fluid, or wetting pattern, can range from one where nearly all the pores are filled with the invading fluid to one where the defending fluid remains trapped in clusters [e.g., 119]. Trapped gas clusters (Figure 4.1), pockets of non-wetting fluid that are surrounded by the wetting fluid, are not only characteristic of two-phase flow in porous media but are very difficult to mobilize because of surface tension. Indeed, gas trapping is a mechanism employed for long term CO_2 sequestration [e.g., 120, 121].

We hypothesize that pumice floats for long periods of time because of the occurrence of gas trapping (either air or non-condensable magmatic gases) in isolated gas clusters during water infiltration. We use X-ray microtomography to test the hypotheses that gas trapping occurs in both hot and ambient temperature pumice, that gas trapping can result in a high enough residual gas saturations to keep pumice afloat, and that percolation theory can describe gas trapping in pumice. While trapped gas may buoy pumice, we hypothesize that the outward diffusion of gas trapped in bubbles eventually causes pumice to sink. We test this gas diffusion hypothesis by conducting experiments where we measure the floatation time of dry and ambient temperature pumice on artificial seawater in a controlled laboratory setting. We then compare our results and pumice floatation times from four other studies with a prediction for pumice floatation time based on gas-diffusion out of a porous medium.

4.2.1 Gas trapping in porous media

Gas trapping has been observed in experiments, dictates wetting patterns, and controls residual saturation of porous media [e.g., 122–124]. A key element of gas trapping and the models that will be described is that the invading fluid is advancing at a constant and very slow rate such that capillary forces dominate over viscous forces. In other words, the Capillary number,

$$Ca = \frac{v\mu}{\gamma} \tag{4.1}$$

where v is the characteristic velocity, μ is the wetting fluid viscosity, and γ is surface tension on the interface between the two fluids, is very low (Ca $< 10^{-6}$) [119, 122, 125].

We calculate a Capillary number for water infiltration into pumice, where $\mu = 10^{-3}$ Pa s is the viscosity of water at room temperature and $\gamma = 0.072$ N m^{-1} is surface tension at the air-water interface, by estimating the velocity, v, of water infiltrating pumice first by using Darcy's law. For pumice floating on water, the maximum head gradient is set by the hydrostatic pressure at the bottom edge of the pumice and the capillary pressure. By assuming a constant pore radius and a hemispherical gas-water meniscus we can write the liquid velocity as

$$v = \frac{\kappa}{\mu\phi}(\rho g h + \frac{2\gamma}{R}) \tag{4.2}$$

where κ is permeability, ϕ is connected porosity, ρ is water density, g is gravity, h is the height of pumice in water, and R is pore throat radius. Pumice porosities can vary widely, but typical values are 50 to 90 percent (pumice must have porosity of at least 58 percent to initially float). Pumice permeabilities are more difficult to estimate, but measured values range from $10^{-10} - 10^{-14}$ m^2 [87–89, 91, 92, 126–129]. We note that permeability may also be a function of saturation, i.e., relative permeability is not unity. From these input parameters, $1.5 \times 10^{-12} <$ Ca $< 2.3 \times 10^{-7}$, which is in the range for gas trapping.

We also use pumice saturation measurements from [70] to estimate water infiltration velocities according to,

$$v = \frac{\Delta V_w}{\Delta t S_a \phi} \tag{4.3}$$

where V_w is the volume of absorbed water, t is time, S_a is pumice surface area, and is porosity. We estimate S_a by assuming the pumice are spherical. Fourteen pumice saturation measurements by [70] reveal average initial infiltration velocities over the first five minutes of

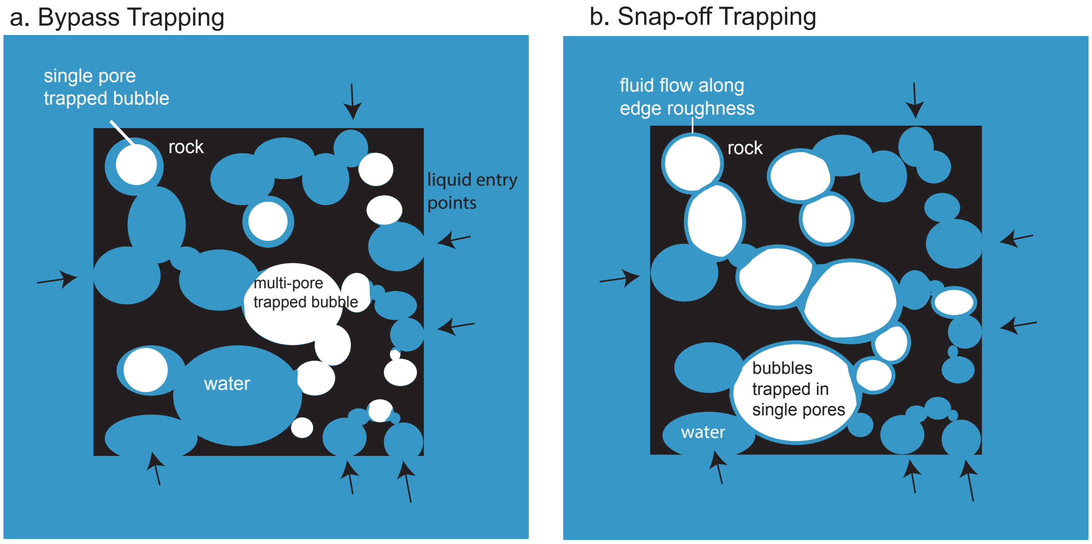

Figure 4.1: Mechanisms of gas trapping. Illustrations of gas trapping by (a) bypass and (b) snap-off trapping in pumice with connected pores. In both cases capillary forces draw water into pores such that water completely surrounds the gas phase and the gas is unable to escape.

water exposure of $2.74 \pm 0.97 \times 10^{-2}$ cm hr^{-1} and Capillary numbers of $7.62 \pm -2.69 \times 10^{-8}$. These Ca estimates indicate that gas trapping may occur in pumice. In the next sections we introduce two mechanisms that allow gas trapping to occur, the percolation models that simulate them, and the gas-trapping predictions percolation theory makes.

4.2.1.1 Bypass trapping

Bypass trapping causes trapping through the sequential filling of pore throats such that the defending fluid becomes surrounded by the invading fluid before it can escape (Figure 4.1a) [e.g., 130]. Invasion percolation models simulate bypass trapping by 1) representing the porous medium as a network of spheres (pores) and cylinders (pore throats); 2) prescribing a capillary entry pressure is for each throat and pore; and 3) filling throats and pores from highest to lowest pressure. As a result, a pore or series of pores with low capillary pressures may be completely surrounded before being filled and thus become trapped (but may contract or expand if compressible).

4.2.1.2 Snap-off trapping

Snap-off trapping occurs because for very low flow rates (or capillary numbers) the wetting fluid can flow along edges of the porous walls due to surface roughness [e.g., 119]. This thin film can swell as the wetting fluid invades. As the film swells in the smallest throats, it completely displaces the nonwetting phase and can disconnect the nonwetting phase from any neighbors (Figure 4.1b). Snap-off trapping is simulated by Bond percolation. When snap-off and bypass trapping are both possible, bypass trapping is favored because it is prescribed by a higher capillary pressure.

4.2.1.3 Percolation Model Predictions

Both invasion and bond percolation theory make predictions about the size distribution of residual trapped gas clusters. Because percolation systems are scale invariant at the critical point (when fully percolated), the number of occurrences, $n(s)$, of trapped gas clusters containing s sites/pores scales according to a power-law,

$$n(s) \propto s^{-\beta} \tag{4.4}$$

where $\beta = \frac{a+f}{f}$ and a is the spatial dimension and f is the fractal dimension of the cluster. In 3D: $a = 3$, $f = 2.52$, and $\beta = 2.19$ [131, 132]. The maximum size of the trapped gas cluster is limited by the samples size, L, $s_{max} \propto L^f$, [133]. Examining the size distribution of trapped gas bubbles in a natural system, such as pumice, can therefore help distinguish if percolation theory (either Bond or Invasion) applies.

4.3 X-ray microtomography

X-ray microtomography (μXRT) allows us to see both the internal structure of pumice and, when multiple fluids are present within the pores, the distribution of those fluids. We use μXRT to: (1) test the hypothesis that gas trapping occurs in pumice; (2) determine if percolation theory can describe the size distribution of trapped gas; (3) examine the size distribution of trapped gas for insights into the mechanisms (bypass or snap-off trapping) that occurs in pumice.

4.3.1 Experimental Set-Up

We used μXRT to image the internal distribution of liquid and air in six uncut pumice clasts. Before the μXRT, we conducted saturation experiments on ambient temperature and hot (500°C) pumice from Santa Maria, Guatemala and Medicine Lake, California (Table 4.1). We set ambient temperature pumice on a 13 wt percent solution of potassium iodide (KI) for ≈20 hours such that the pumice could adsorb the liquid. KI, a common chemical dopant, increases contrast of the μXRT images (greatly improves the segmentation of air and water in the images), while maintaining a surface tension within 1 percent of water [134, 135].

We heated two of the pumice samples (SM04 and SM05) to 500°C, quenched these pumice clasts in the KI dopant, and allowed them to stay in the solution for ≈10 minutes. All pumice pores were filled with air at the time of KI exposure. To preserve the internal fluid distributions for μXRT imaging, we then rapidly removed and encased the pumice in wax.

We carried out the μXRT imaging at the Lawrence Berkeley National Lab Advanced Light Source on beamline 8.3.2. We conducted the scans using 30 kev monochromatic X-Rays and a 5X lens (resolution of 1.22 μm/pixel). We used the TomoPy gridrec algorithm to reconstruct the 3D image stacks [136].

To minimize ring artifacts, we selected a subvolume from each data set of either 0.37 or 0.94 mm^3 for data processing. We used Fiji's Trainable Weka Segmentation plugin - which employs multiple machine learning algorithms - to segment air, water, and rock within each image sequence [137]. To train classifiers for each image sequence, we manually outlined vesicles and trapped air on fifty different images. After checking and retraining the classifiers as necessary, we applied the trained classifiers across the images sequences to segment air and rock (thereby creating two sets of binarized image sequences for each sample).

We also made the image sequences binary by applying a greyscale threshold in Fiji, but determined that the machine learning method reduced the effect of annular ring artifacts and better preserved thin glass walls compared to the traditional threshold based binarization method. Despite the advantages of the machine learning method, two image sets (SM02 and SM05) had glass walls that were too thin to resolve and we do not report porosities or vesicle size distributions for these samples.

After we segmented each data set, we loaded the binary images into Avizo where we identified and quantified the volume, surface area, and orientation of individual bubbles and vesicles. Here we refer to the pores of the pumice (that can be filled with either gas or liquid) as vesicles and areas where the gas phase is present as bubbles. Because most samples had highly interconnected porosities, we separated connected vesicles using a watershed algorithm before measuring vesicles sizes and orientations (supplementary information). No separation was applied to the gas bubbles. As a result, any observed and reported gas bubbles were truly isolated. We note, however, that some gas bubbles may appear connected (by one or two voxels) when they are not if glass walls are thinner than one pixel. To correct for very thin glass walls we use a neighborhood value of six in the Avizo labeling module such that bubbles must share at least one voxel face to be considered connected.

Errors in generating the bubble and vesicle size distributions stem from two main sources: (1) ring artifacts in the original greyscale image and (2) vesicle walls that are thinner than the voxel resolution and that may also lead to overestimates of connected porosity. Through examination of twenty 2D images from each dataset, we estimate that ring artifacts result in the mischaracterization of gas or water in <1 volume percent of each pumice. While the machine learning method for image segmentation reduced the effects of ring artifacts compared to threshold based segmentation, it introduced a number of very small (artifact) bubbles and vesicles that do not contribute to the total volume fraction of pores or trapped

Sample name	SM01	SM02	SM04	SM05	ML01	ML02
Pumice mass (g)	0.07	0.19	0.13	0.04	0.15	0.76
Pumice dimensions (mm^3)	9 x 4.5 x 4	11 x 7 x 4.5	11 x 6 x 5	6.5 x 3 x 3	9.5 x 5 x5	5 x 5 x 4
Temperature	ambient	ambient	500°C	500°C	ambient	ambient
Ending buoyancy	floating	nuetrally buoyant	not floating	not floating	not floating	barely floating
Porosity	0.70	NA	0.73	NA	0.63	0.67
Connected porosity	0.70	NA	0.73	NA	0.55	0.65
Liquid volume/total volume	0.30	NA	0.56	NA	0.13	0.31
Gas volume/total volume	0.40	0.36	0.17	0.13	0.50	0.36
Liquid volume/pore volume	0.43	NA	0.77	NA	0.21	0.46
Calculated wet density/KI density	0.86	NA	1.07	NA	0.83	0.93
Trapped gas bubble number density (cm^{-3})	$9.6x10^5$	$3x10^6$	$4.4x10^6$	$4.2x10^6$	$7.2x10^6$	$2.3x10^6$
Vescicle number density (cm^{-3})	$8.3x10^6$	NA	$1.5x10^7$	NA	$9.6x10^6$	$5.3x10^6$
β: Power law exponent	2.02	1.90	1.95	2.10	1.83	1.51
Smallest bubble fit to power law (mm^3)	$5.9x10^{-5}$	$1.3x10^{-5}$	$2.3x10^{-5}$	$3.1x10^{-6}$	$1.3x10^{-4}$	1.0^{-6}
p:Bubble volume to surface area exponent	0.82	0.82	0.77	0.76	0.75	0.83
Size of analyzed volume (mm^3)	0.94	0.37	0.37	0.94	0.94	0.37

Table 4.1: While μXRT analysis is done on subvolumes of larger clasts, we expect the subvolumes to be representative of the larger pumice in part because the pumice are relatively small (i.e., < 1 g). Furthermore, the selected pumice samples do not have bread crust textures such that we expect differences between rim an internal porosities to be minimal.

gas. As a result, we filtered the data to exclude any bubbles or vesicles with less than a 4 pixel radius or smaller than 10^{-6} mm^3.

4.3.2 X-ray microtomography results

We find trapped gas clusters in all pumice we imaged (Figures 4.2 and 4.3). Trapped gas cluster size varies and gas clusters fill part of, single, and multiple vesicles (Figures 4.2 and 4.3). Because connected porosities for most samples are close to or equal to the total porosity, isolated gas pockets are due to trapping by liquid instead of isolation by rock (Table 4.1). Furthermore, we found that ambient temperature pumice contain larger volume percentages of trapped gas (36 - 50 percent) than the hot pumice (13 and 17 percent) (Table 4.1).

We use μXRT measurements of phase (liquid and water) saturations to estimate pumice buoyancy, assuming glass densities of 2.4 g cm^{-3}, and find that the observed trapped gas saturations are high enough to allow pumice to float. These density calculations match our observation that many of the pumice clasts were floating or neutrally buoyant when we encased them in wax. Our density calculation of ML01, however, does not match our observation that ML01 was not floating (Table 4.1). Discrepancies between observations and density estimates suggest that gas and liquid saturation within pumice is likely heterogeneous. Indeed, we visually observed areas of more and less gas saturation within μXRT images.

The size distributions of both trapped gas (black) and segmented pores (grey) are shown in Figure 4.4. For the majority of samples (ML02, SM01, SM02, and SM05) at least a third of the trapped gas is contained within one large cluster. These clusters, in cases where the vesicle size distributions are known (SM01 and ML02), greatly exceed the maximum vesicle

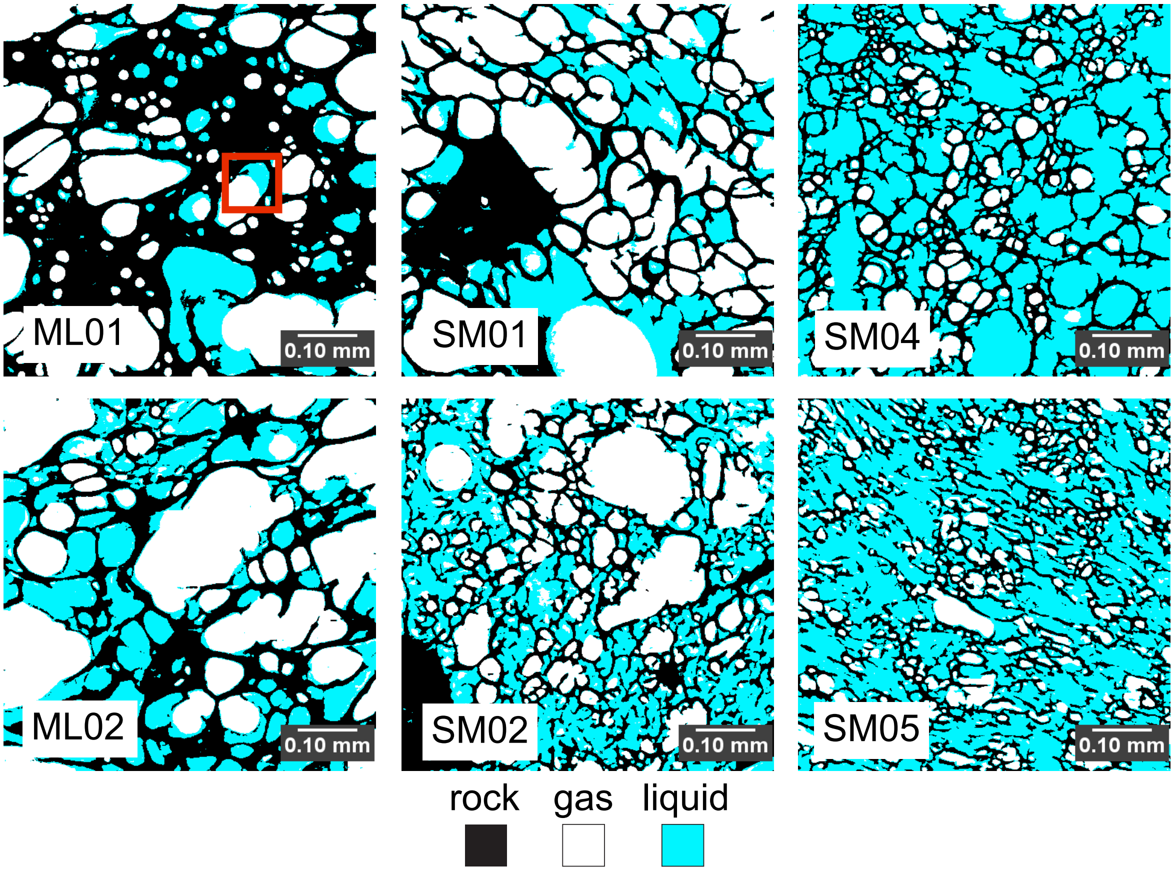

Figure 4.2: X-ray microtomography images. 2D slices through μXRT images of pumice containing water and trapped gas. While hot pumice (SM04 and SM05) contain trapped gas, they hold smaller volume percentages compared to ambient temperature pumice. Contacts between rock, liquid, and gas demonstrate that the liquid is the wetting fluid (see red box). While glass walls are too thin to resolve in places (particularly in SM02 and SM05), we do not see any evidence in the μXRT that the thin glass walls in pumice are broken or damaged due to cleaning in an ultrasonic bath. (For interpretation of the references to color in this figure legend, the reader is referred to the web version of this article.)

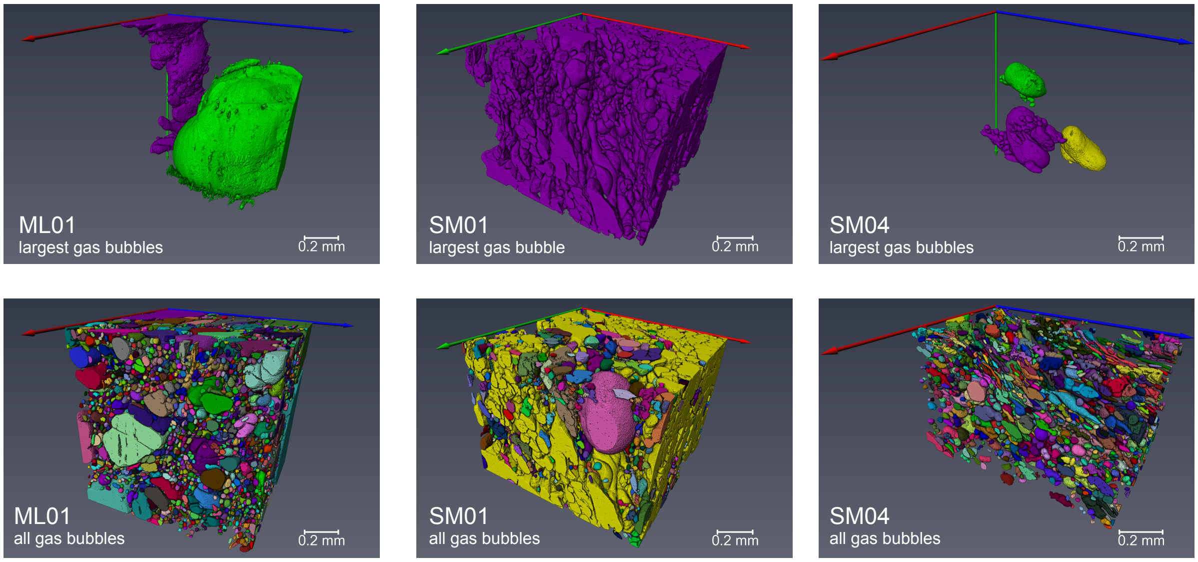

Figure 4.3: Shapes of trapped gas bubbles. 3D μXRT images of trapped gas bubbles within pumice. Colors in this figure are chosen at random to identify separate gas bubbles. The top rows show the largest gas bubbles and the bottom row shows all gas bubbles within a single pumice. A single interconnected gas bubbles extends throughout many pores in pumice SM01. (For interpretation of the references to color in this figure legend, the reader is referred to the web version of this article.)

size and Figure 4.3 shows how these largest trapped bubbles can extend throughout multiple vesicles. The trapped bubble size distributions, however, show that there are multiple modes of trapped bubbles sizes. In sample ML01, the trapped bubble size distribution mirrors the vesicle size distribution.

4.3.3 Comparison to percolation theories

Here we test the hypothesis that percolation theory can describe gas trapping in pumice by fitting Equation 4.4 to the observed distribution of trapped gas clusters using the maximum likelihood method [138, 139]. We find that Equation 4.4 fits the observed distributions well and that fitted power-law coefficients range from 1.51 - 2.10, which (other than the coefficient for ML01) are close to the value predicted by percolation theory ($\beta = 2.19$) (Figure 4.5; Table 4.1). These power-law fits lend support to a percolation theory treatment of pumice saturation.

Percolation theory also predicts $A \propto V^p$, where A is the surface area of the trapped clusters, and V is the volume of the trapped clusters [131]. From our data sets, we empirically find $p = 0.75 - 0.83$ and the R^2 values for these fits are $0.95 - 0.99$ (Table 4.1). Values of p

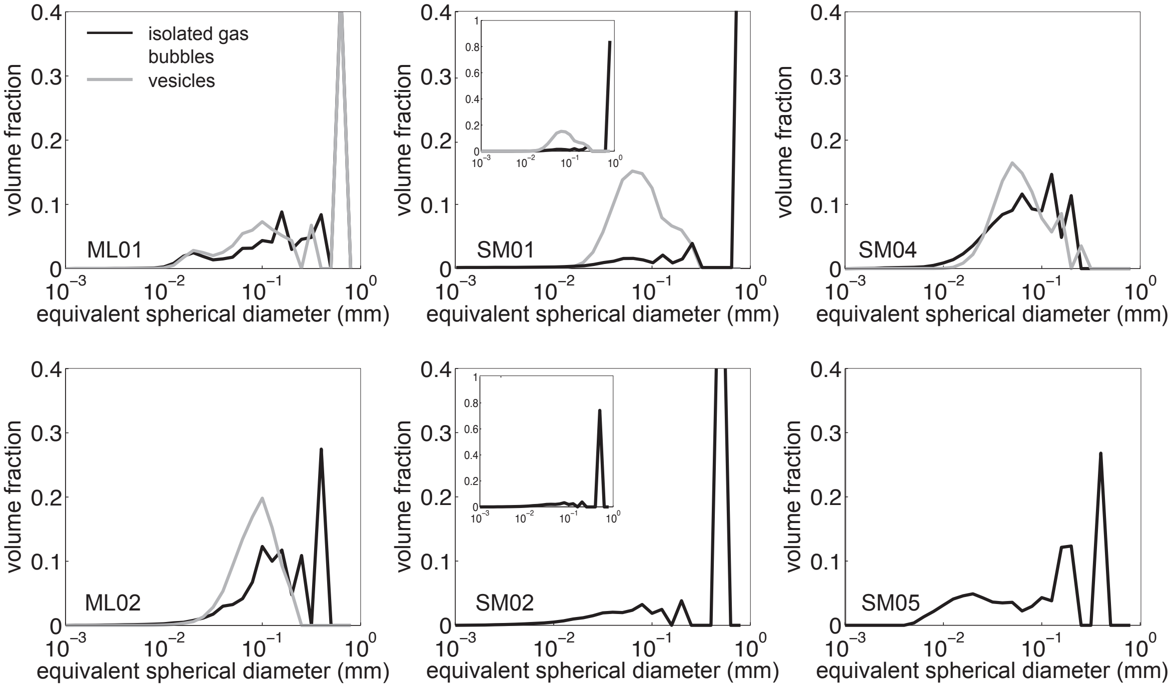

Figure 4.4: Bubble and vesicle size distributions. Trapped gas bubbles, locations where only the gas is present, are shown in black, and vesicles, pumice pores that can be filled with liquid or gas, are in grey. At least a third of the trapped gas is contained with a single large bubble for most of samples. The existence of large trapped bubbles, in combination with the vesicle size distribution, demonstrates that at least the largest gas clusters often extend through multiple pores. Bubbles and vesicles are binned into fifty logarithmically spaced bins and each bin is divided by the total volume of air or vesicles. Volume fraction is not weighted by bin width such that the sum of all bins equals one.

greater than 2/3 demonstrates that the gas bubbles are non-spherical.

4.4 Mechanisms that cause pumice to sink

The previous sections demonstrated that gas trapping occurs in pumice, that ambient temperature pumice traps more gas than hot (500°C) pumice, that gas trapping can lead to high enough residual gas saturations to allow pumice to float, and that percolation theory can describe the distribution of trapped gas clusters. The occurrence of gas trapping does not, however, explain why pumice, after floating for days or months, eventually sinks.

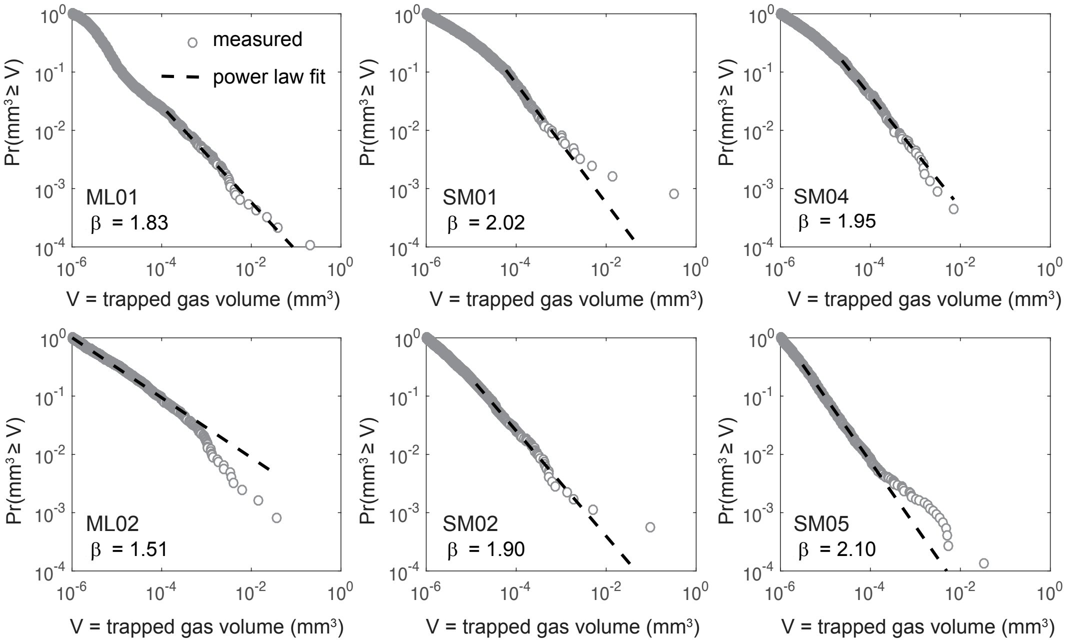

Figure 4.5: Power-law fits of bubble-size distributions. Measured distributions of trapped bubble volume (grey circles) and the fitted power-law distributions (dashed lines). The y-axis shows the probability that a bubble is larger than a given volume, V. With the exception of ML02, the fitted power-law coefficients, β, are consistent with the value predicted from percolation theory, $\beta = 2.19$. Because our machine learning segmentation method generated very small (artifact) bubbles, we removed bubbles smaller than 10^6 mm^3 before fitting a power-law coefficient.

4.4.1 Pumice floatation experiments

To examine why pumice sinks, we conducted pumice floatation experiments using pumice from the 1902 plinian eruption of Santa Maria Volcano, Guatemala. We placed the pumice in artificial seawater and measured the time it took for the pumice to sink. Before the experiments, we cleaned the pumice in an ultrasonicator for four hours and dried the pumice in an oven at 65°C for 12 hours. We specifically chose a temperature lower than 100°C to ensure that we did not break pumice walls during the drying process and used μXRT to confirm that the pumice was dry prior to experiments. Table 4.2 shows the pumice weights, sizes, and characteristics. While we did not measure the volume of each pumice clast, we estimated volume by assuming porosities of 80 percent and glass densities of 2.4 g cm^{-3}.

To initiate the floatation experiments, we dropped the pumice from a height of 4 cm into individual containers of artificial seawater. These containers were covered to prevent evaporation and contamination. We monitored the pumice with a time lapse camera that could determine when each clast sank to the nearest minute.

4.4.2 Pumice floatation timescale

Here we propose that the diffusion of trapped gas bubbles out of the pumice (and eventually to the atmosphere) causes pumice containing trapped gas clusters to sink. We envisage that the diffusion process is analogous to Ostwald ripening where small (and thus higher pressure) trapped gas clusters diffuse into larger clusters and eventually to the atmosphere. If gas diffusion does control pumice buoyancy through time, then pumice floatation time should scale like a diffusive process where

$$\tau \propto \frac{L^2}{D_{eff}} \tag{4.5}$$

and where L is the mean diameter of the pumice, and D_{eff} is the effective diffusion coefficient. The effective diffusion coefficient for trapped gas in pumice, as in other porous media, is not just the gas-liquid diffusion coefficient, but should be weighted by the connectivity of the porous media (i.e., porosity and partial saturation). From [140] we write effective diffusivity as $D_{eff} = D\theta^2$, where θ is water saturation (fraction of pore space filled by water) and D is the liquid-gas diffusion coefficient, such that

$$\tau \propto \frac{L^2}{D\theta^2}. \tag{4.6}$$

We test the hypothesis that diffusion of trapped gas out of pumice allows pumice to sink by comparing experimental measurements of pumice floatation time and volume [70, 115, 141, 142] with Equation 4.6 and where $L \approx V^{2/3}$ (Figure 4.6). Because we do not know θ for any individual pumice, and because, if our hypothesis is correct, θ changes through time, we consider Equation 4.6 with a range of saturation values (8 - 80 percent).

4.4.3 Pumice floatation results and model comparison

Figure 4.6 shows measurements of floatation time and volume (this study and four others) against predictions from Equation 4.6 and where $D = 1.9 \times 10^{-5}$ cm^2 s^{-1} is the air-water diffusion coefficient at room temperature. Experimental measurements of pumice floatation times generally match predictions from Equation 4.6 (Figure 4.6). We also list pumice floatation times from our experiments in Table 4.2.

It is worth noting, however, that if pumice are highly non-spherical, then we overestimate the effective length scale (shortest pumice axis). Furthermore, the timescale for pumice floatation may depend strongly on θ, not only because θ affects the diffusivity, but also because more diffusion must occur to sink a pumice with an initially high trapped gas content.

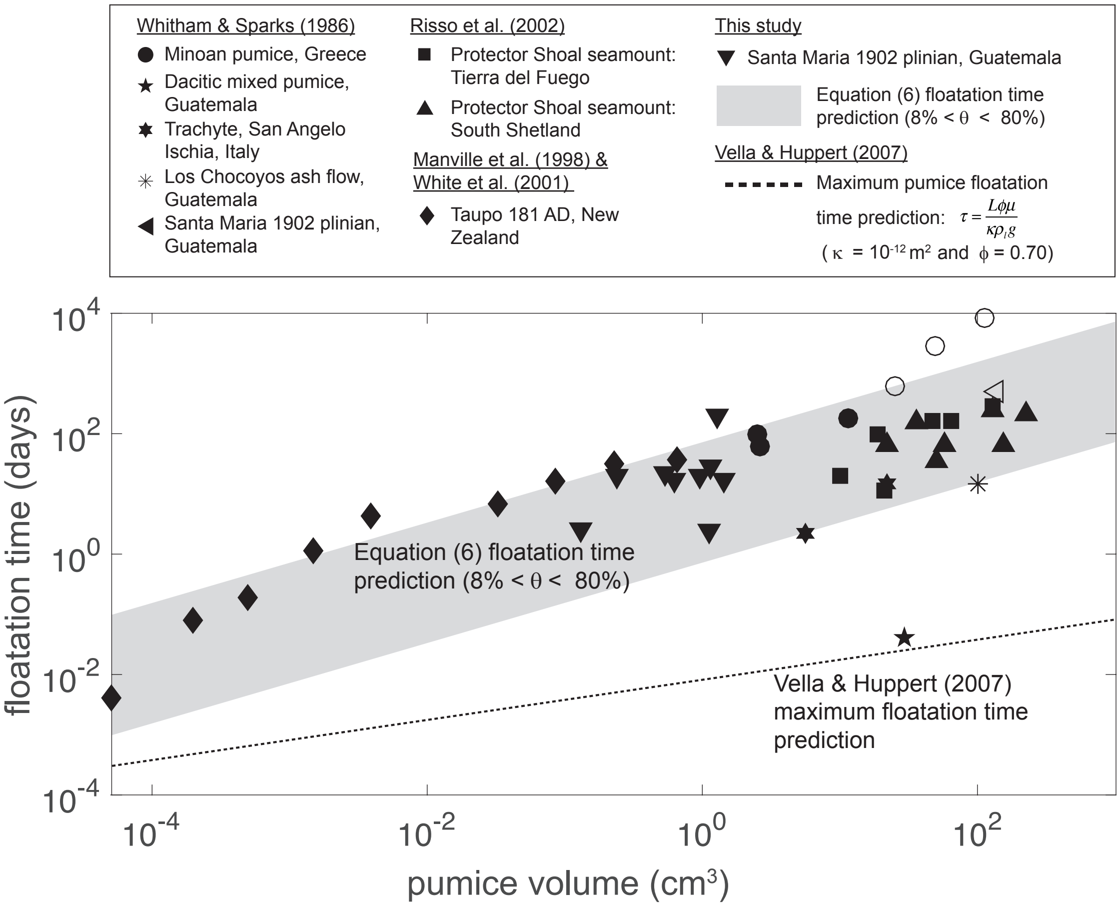

Figure 4.6: Floatation time as a function of pumice volume. Measurements of pumice floatation from this study, [70], [141], [115], and [142]. Pumice floatation time predictions from this study (Equation 4.6) and [82] are also shown. Measured floatation times fit the trend predicted by Equation 4.6 (grey bar). Filled symbols represent measured sinking times while open symbols represent projected sinking times.

While we are not the first to recognize that pumice floatation time scales like a diffusive process [141], diffusion of trapped gas out of the pumice has not previously been identified to be the controlling process. Figure 4.6, in combination with observations of gas trapping, suggests that it is the diffusion of trapped gas out of pumice that causes raft and other floating pumice to eventually sink.

4.5 Discussion

4.5.1 Gas Trapping Timescale

We find that water saturation of pumice is a two-step process. First, capillary and hydrostatic pressures drive water into pores. Water invasion often leads to gas trapping (e.g. section 4.1) and ends when there are no longer pores to invade. Second, gas slowly diffuses out of trapped gas pockets thereby creating more space for the liquid (section 4.3). Here we estimate the timescale for the first of these processes - the time for pumice to reach its residual saturation state. If pumice can be modeled as a bundle of horizontal parallel cylindrical tubes and capillary pressures drive fluid into the tubes, then the Washburn equation can describe the timescale for water saturation over horizontal distance L,

$$t = \frac{4L^2\mu}{\gamma d} \tag{4.7}$$

where d is mean pore throat diameter. Equation 4.7 suggests that pumice with 0.05 mm diameter pores should reach its residual saturation state very rapidly: 2.7 seconds for 5 cm pumice and 18 minutes for 1 m pumice. In other words, if a dry pumice is set on water, then capillary forces draw in liquid quickly and set the wetting pattern and trapped gas geometry in timescale, t. We emphasize that pumice can remain buoyant following water invasion due to gas trapping.

4.5.2 Water saturation of hot versus cold pumice

We find that residual gas saturation is lower for hot pumice (500°C) compared to ambient temperature pumice, and that these lower gas saturations can account for the buoyancy differences of hot versus cold pumice (Table 4.1). Because hot pumice may rapidly saturate due to non-condensable gas contraction [70, 71, 108], we compare the pressure differences generated by three processes that can drive fluid into pumice: water column weight, capillary action, and gas cooling and contraction. Gravity induces a pressure difference when pumice is submerged in water proportional to,

$$\Delta p = (\rho_l - \rho_g)gL \approx 10^3 \text{ Pa}, \tag{4.8}$$

choosing $L = 10$ cm. The pressure difference induced by capillary forces is,

$$\Delta p = \frac{2\gamma}{R} \approx 1.5 \times 10^4 \text{ Pa}, \tag{4.9}$$

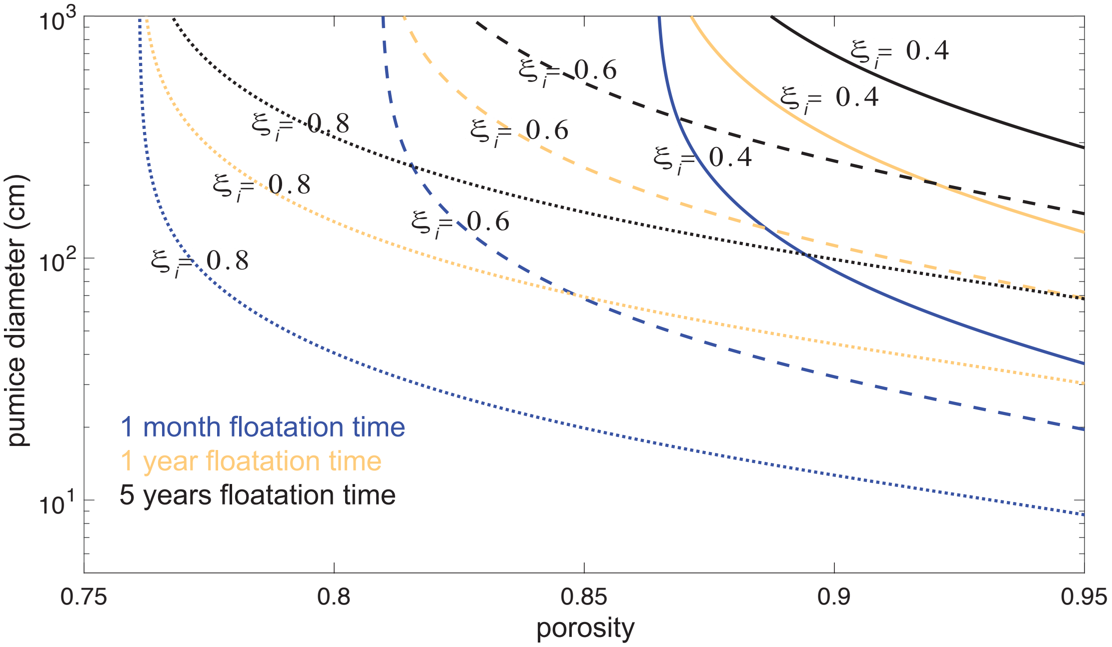

Figure 4.7: Floatation time as a function of clast size, porosity and initial saturation. We plot solutions to Equations 4.14 and 4.15 to demonstrate how floatation time varies with pumice size, porosity, and initial gas saturation, ξ_i. We assume $\rho_r = 2.4$ g cm^3, $\rho_l = 1.0$ g cm^3, and sum the first ten terms of Equation (14).

where $R = 10$ μm is pore throat radius. Lastly, the pressure difference created by gas contraction is proportional to the change in temperature of the gas by the ideal gas law such that

$$\Delta p = P_i \frac{\Delta T}{T_i} \tag{4.10}$$

Assuming that the initial pressure, P_i, of the gas is atmospheric ($\approx 10^5$ Pa), the initial temperature of the gas, T_i, is 800 K, and the change in gas temperature, ΔT, is 500 K, then $P \approx 3.7 \times 10^4$ Pa.

Gas contraction can thereby produce pressure differences as large as those produced by capillary forces which suggests that, because pressure gradients drive fluid flow, gas contraction can be a relevant process for liquid ingestion. Furthermore, we expect that heat transfer from pumice to liquid is rapid (<1 s) because pumice walls are very thin,

$$t \approx \frac{L_w^2}{D_w}, \tag{4.11}$$

where $L_w \approx 10^{-5} - 10^{-6}$ m is the glass wall thickness (Figure 4.2) and $D_w \approx 10^{-7}$ m^2 s^{-1} is water thermal diffusivity. Rapid heat transfer suggests that gas contraction occurs simultaneously with capillary induced pore filling. We note, however, that gas contraction may not proceed prior to pore filling because hot gas must contact cool liquid for heat transfer [e.g., 55]. Following the derivation of the Washburn equation (Equation 4.7), we derive a new timescale for the initial stage of water ingestion into pumice when both gas contraction and capillary forces drive fluid flow:

$$t = \frac{4\mu L^2}{R^2(\frac{2\gamma}{R} + \frac{P_i \delta T}{T_i})} \tag{4.12}$$

Gas contraction in hot pumice may help to explain the differences in residual gas saturation of hot and cold pumice. When pressure does not change, according to the ideal gas law

$$\frac{V_i}{V_f} = \frac{T_i}{T_f}, \tag{4.13}$$

where V_i and T_i are initial volume and temperature of gas within a pumice and V_f and T_f are final volume and temperature, respectively. We therefore expect that when air is cooled from 800 to 300 K, $V_f = 0.37V_i$. Our experiments showed that hot pumice contained gas in ≈ 23 percent of pore space while ambient temperature pumice retained gas in $54 - 79$ percent of its pore space. This reduction in trapped gas volume is $\approx 0.23/0.7 = 0.32$ and is approximately the value (0.37) predicted by gas contraction alone. Trapped bubble size distributions matched percolation theory for both hot and ambient temperature pumice (Figure 4.5). Invasion percolation theory works by prescribing a capillary entry pressure for each pore and filling pores from highest to lowest entry pressure. Percolation theory may apply to hot and non-condensable gas-filled pumice because gas contraction introduces a new, yet additive, pressure difference across each pore and thus does not fundamentally change the mechanism for pore filling.

4.5.3 Bypass versus snap-off trapping

While the fit of Equation 4.4 to the measured trapped gas bubble size distributions supports a percolation theory control on pumice saturation, we have yet to determine if gas is trapped by bypass or snap-off mechanisms. The trapped bubble area-to-volume ratios show that the trapped bubbles are non-spherical (Table 4.1). Furthermore, we observe trapped gas within many interconnected pores (Figure 4.3). Because snap-off trapping leads to gas bubbles trapped in single pores (e.g., Figure 4.1), these observations support a bypass trapping mechanism. Furthermore, bypass trapping is topologically favored over snap-off trapping when both are possible.

4.5.4 Gas diffusion model

In section 3 we demonstrated that the slow diffusion of trapped gas bubbles causes pumice to eventually sink. Here we plot solutions to the diffusion equation to examine how

Sample name	Dry weight (g)	Estimated volume (cm^3)	Floatation time (days)
SMF02	0.30	0.63	17.3
SMF03	0.25	0.53	22.7
SMF05	0.46	0.95	20.2
SMF06	0.68	1.42	17.0
SMF09	0.61	1.28	195.5
SMF10	0.06	0.13	2.6
SMF11	0.55	1.15	28.2
SMF12	0.54	1.12	2.5
SMF22	0.12	0.24	20.1

Table 4.2: Floatation time measurements for Santa Maria pumice

pumice floatation time varies as a function of pumice size, porosity, and initial trapped gas saturation. To write a solution to the diffusion equation we make several assumptions: (1) pumice is spherical; (2) the binary water and gas mixture in pumice can be described as a continuum, (3) initial trapped gas saturation is uniform within the pumice, (4) the diffusion coefficient is constant, (5) pumice pores are entirely connected, and (6) the pumice is entirely submersed in water. With these assumptions in place, the average saturation (gas volume/pore volume) in a spherical pumice of diameter L, with initial interior gas saturation ξ_i, and with gas saturation equal to zero at the boundaries $L/2$ is

$$\xi(t) = \frac{6\xi_i}{\pi^2} \sum_{n=1}^{\infty} \frac{1}{n^2} e^{-D_{eff} n^2 \pi^2 t/(L/2)^2} \tag{4.14}$$

[141, 143]. Here we let $D_{eff} = D\theta_i^2 = D(1-\xi_i)^2$ (e.g., Equation 4.6). Pumice sinks when its average density is equal to the density of the surrounding liquid such that

$$(1-\phi)\rho_r + \phi(1-\xi^*)\rho_l = \rho_l, \tag{4.15}$$

where ρ_r is the density of the solid phase, ξ^* is the gas saturation when a pumice is neutrally buoyant and ρ_l is the liquid density. By combining Equations 4.14 and 4.15 we can calculate pumice floatation time, the time it takes a pumice to reach gas saturation ξ^*, as a function of pumice size L, porosity ϕ, and initial gas saturation ξ_i. Figure 4.7 shows solutions to Equations 4.14 and 4.15 using contours of constant floatation time. Figure 4.7 explores how pumice size, porosity, and initial gas saturation affect pumice floatation. We find that high porosity pumice need higher initial gas saturations to float for the same period of time as lower porosity pumice. Pumice size and porosity vary inversely along contours of constant floatation time and, for constant ϕ and ξ_i, larger pumice float longer.

4.6 Conclusions

In this paper, we explore the processes that allow pumice to float and sink. To do this, we studied pumice saturation at the scale of pore level processes where capillary forces may be relevant. From estimates of the capillary number - which indicate that surface tension dominates over viscous forces in pumice - we hypothesized that pumice can trap isolated gas bubbles as water infiltrates its pores. We used X-ray microtomography to determine if gas trapping occurs in pumice and found that both ambient temperature and hot (500°C) pumice trap gas. We observed, however, that hot pumice traps far less gas than ambient temperature pumice, consistent with the observation that hot pumice (> 300°C) often sinks after contact with water [70–72]. That is, cold pumice can trap enough gas to keep the pumice afloat while gas contraction in hot pumice leads to lower residual gas saturations.

We examined the size distributions of trapped gas in both hot and ambient temperature pumice and found that the distributions fit a power-law prediction from percolation theory. The power-law fits support a percolation theory treatment of water infiltration into pumice.

While trapped gas can buoy pumice, we hypothesized that outward diffusion of the trapped gas clusters causes pumice to eventually sink. We quantified this hypothesis with a model for pumice floatation time in terms of trapped gas diffusion (Equation 4.6). To test the gas diffusion hypothesis, we conducted pumice floatation experiments and compared Equation 4.6 to our results as well as data from four other studies. We found that the observed pumice floatation times match a trapped gas diffusion prediction (Figure 4.6). Furthermore, we plot solutions to the diffusion equation on a sphere to explore pumice porosity, size, and initial gas saturation affect floatation time (Figure 4.7).

A mechanistic explanation for pumice floatation is an important step towards understanding when and how pumice is partitioned into rafts versus submarine deposits [e.g., 105, 107, 108, 112]. Indeed, submarine volcanic deposits may not record eruption dynamics because non-condensable (i.e., CO_2 or air) gas trapping can make pumice buoyant. Furthermore, our results suggest that the lifetime of buoyant pumice rafts is not just limited by pumice abrasion [e.g., 13, 142], but also by gas diffusion. Non-condensable gas trapping and diffusion, by controlling pumice buoyancy, are therefore important controls on the transport and fate of pumice in the marine environment and location in the rock record.

4.7 Acknowledgements

X-ray microtomography was enabled by access to the Lawrence Berkeley National Lab Advanced light source on beamline 8.3.2. We thank Dula Parkinson for guidance with XRT imaging and image processing. A stimulating conversation with Alan Rempel helped to develop the initial gas trapping hypothesis. We thank Tushar Mittal for suggesting the machine learning segmentation algorithm and Steve Breen for informative discussions on percolation theory and for reviewing an earlier version of this manuscript. We thank Ray Cas, Thomas Giachetti, and EPSL editor Tamsin Mather for thoughtful reviews that contributed to this manuscript. Finally, we are grateful for support from Judy Webb and the US National Science Foundation EAR 1447559. Data and code used in this study are available on VHub at https://vhub.org /resources/4117.

Chapter 5

Conclusions and future directions

Nearly every natural surface on Earth was formed or sculpted by a geophysical flow such as a river, glacier, lava flow, or density current. Even the ocean floor is covered in lava flows, sediment, and volcanic ash. Understanding how geophysical flows transport, erode, and deposit material is central to understanding the past and future evolution of Earth's surface. The focus of this dissertation has been on understanding the dynamics of two types of volcanic phenomena - dilute pyroclastic density currents and the products of submarine eruptions. Here I outline open questions and a vision for future work.

5.1 Future work: erosion by pyroclastic density currents and multiphase flows

Pyroclastic density current are similar to other gravity flows composed of fluid-particle mixtures such as turbidity currents and debris flows in that particles and density contrasts drive the flow forward. While density currents have been widely studied and it is known that debris flows, turbidity currents, and PDCs can be erosional, we lack a mechanistic understanding of the erosional processes relevant for many particle-laden flows [e.g., 5, 21, 144]. Erosion matters because erosion can dramatically alter a landscape and the bulking of the flows changes flow mobility.

In chapter 2, I proposed a new erosional mechanism that may be important in dilute PDCs, particle splash. I incorporated a term for particle splash into the mass conservation equation for a depth-averaged PDC model and found that particle splash could increase PDC runout distance by an order of magnitude. The effectiveness of particle splash on PDC bulking may be hampered, however, by the presence of a dense bed load region that was not considered in my model. Particle entrainment may also increase the thickness or density of a dense bedload region. To test these ideas and determine how vertical gradients in particle concentration affect entrainment, in the future I can incorporate expressions for particle splash, and the accompanying particle velocity distributions, into 3D multiphase models for PDCs [e.g., 38]. My 1-D model assumed, furthermore, that entrained particles

Figure 5.1: Channel erosion by a Februrary 2017 debris flow. The debris flow removed overlying sediment and scoured at least 10 cm into shale bedrock. Debris flow scouring in this channel continued for 100s of meters downstream of this photo. One can see boulder and fine-sediment deposits from a debris flow that entered the channel on the right side of the figure.

were instantly accelerated to the mean velocity of the flow and a more rigorous treatment of momentum conservation [e.g., 21] may be needed to fully understand how entrainment and erosion affect PDC dynamics.

The connection between the dilute and dense PDC end-members remains poorly understood. Specifically, the mass and momentum exchange between the two regions has not been directly measured and it remains to be seen if these two end-member models (e.g., Figure 2.1) apply to the full spectrum of PDC behavior. Recent studies have made progress towards understanding this coupling. [145] examined the internal structure of density currents in the lab and discovered an intermediate flow region containing mesoscale turbulent structures (particles cluster on the outer region of eddies and turbulence is dampened) and that efficiently transfers mass and momentum to the dense bed load region. [146] coupled depth-averaged flow models for the dilute and dense region of PDCs and concluded that dense PDCs can form a surge when their velocity exceeds ≈ 25 m s^{-1} and that topographic features that increase PDC speed greatly enhance dilute PDC formation. These conclusions rest, however, on a highly non-linear term that governs the exchange between the dilute and concentrated flow regions and that is borrowed from windblown particle transport dynamics

$$q_e \propto u^3, \tag{5.1}$$

where q_e is particle flux due to particle entrainment and u is mean flow velocity. A model for particle splash is embedded in Equation 5.1. Energy conservation dictates that the flux of particles resulting from splash is, $q_e \propto Nv^2$, where N is the number of particles hitting the bed and v is the particle impact velocity. One can then derive Equation 5.1 by assuming $N \propto c$, $c \propto u^* \propto u$ and $v \propto u$, where c is particle concentration and u^* is the shear velocity of the flow [e.g. 43, 147]. Particle splash has therefore not only been proposed as an entrainment mechanism in PDCs, but is being used to model dense and dilute flow coupling. Care should be taken, however, to carefully consider the form of the splash expression because our study demonstrates that the form may be different than previously assumed (Chapter 2) and the expression directly affects conclusions drawn about PDC dynamics. Laboratory experiments [e.g., 66, 145] may help to validate internal coupling functions used in PDC models.

Debris flows are similar to PDCs because they are particle laden density flows but differ in that they are particle-water mixtures and their density contrast with the ambient fluid is often much higher. Debris flows are common, are important geomorphic agents, and can be devastating (e.g., Armero Colombia, 1985). Following a heavy rain event in Northern California on February 17 and 18, 2017 (8.9 cm in 10 hours), I explored a field area in California's Great Valley Sequence where debris flows had scoured tens of centimeters into the underlying bedrock (intermixed shale and sandstone) (Figure 5.1). Figure 5.1 shows that the event triggered debris flows scoured into bedrock and transported sediment and boulders. Not all landslides generated debris flows, however, and in at least one case an erosional debris flow was triggered without a landslide. This event highlights opportunities for future work and open questions in areas of active research including: How do debris flows erode underlying bedrock and loose sediment? How does the underlying lithology affect the effectiveness of debris flow scour? How do we predict the occurrence and location of debris flows with process-based models? How do we incorporate a mechanistic understanding of debris flow dynamics into landscape evolution models? Field observations at the site shown in Figure 5.1 could motivate and constrain experiments and models that address these questions.

5.2 Future work: submarine eruption dynamics

Despite comprising up to 80 percent of Earth's volcanism [e.g., 11], submarine eruptions remain poorly understood and understudied. Only 11 submarine eruptions have been verified in the last 30 years [148]. As a result, mechanisms that disperse material from from submarine eruptions also remain relatively unobserved and poorly quantified. For example, it has only recently been proposed that volcanic ash may be widespread or prevalent in oceanic sediment [e.g., 14, 149] and there are few quantitative models for submarine plume dynamics [e.g., 73]. As a step towards understanding how volcanic material is dispersed, I used laboratory experiments to develop clast-scale models for pyroclast dynamics in water in chapters 3 and 4. More work is needed, however, to develop and test models for the dispersal of volcanic material in the submarine environment. In the future I plan to use the clast-scale models presented here to build submarine plume models that can test ideas about submarine plume dynamics.

Increasing observations of submarine eruptions and the dispersal of volcanic products is key to understanding the spectrum of behavior of these processes. For example, the 2012 eruption of Havre submarine volcano demonstrated that high porosity clasts can be created in the deep (> 800 m) submarine environment [14]. The 2015 eruption of Axial volcano showed us how submarine volcanoes can display precursory activity (earthquake sensitivity to tides) prior to an eruption [150]. Small-scale explosive basaltic eruptions at NW Rota-1 and West Mata, NE Lau Basin suggest that gas slugs can drive explosive submarine eruptions (similar to a Strombolian eruption model) [7–9]. These submarine eruptions are some of the most well-studied and they have widely varying eruption styles. Rather than build models based a single case-study volcano, more observations are needed to fill out a catalog of eruption styles and create a statistically significant data set. More observations may help, for example, identify the signature/s of magma-water interactions in volcanic deposits and therefore elucidate the role of water in submarine eruptions. At the same time, submarine volcano exploration is resource intensive and existing data sets (e.g., satellite imagery) may be better leveraged to address open questions about the frequency and location of submarine volcanism.

Pumice rafts provide a surface expression of submarine volcanism. However, only twenty rafts have been documented within the last 200 years [117], in part because our volcano databases are not well-suited for documenting rafts which have no clear vent of origin. Work is in progress in collaboration with Tushar Mittal to identify pumice rafts with satellite images. From Landsat 7 and 8 data we have found more than 200 images containing pumice rafts in the Tonga and Fiji region and since 1999. While it is unclear how many distinct eruptions created these rafts, the prevalence of rafts in the region suggests that number of raft-forming submarine eruptions, at least in the Tonga/Fiji region, is greater than previously recognized.

In several cases, rafts can be traced back to a specific vent. By identifying new vents we can better understand the geographic distribution of active submarine volcanoes. Our catalog of submarine eruptions could be further improved by acquiring bathymetry data once new vents or eruptions are identified. While submarine exploration is limited by the high costs related to cruises, ship-based multibeam provides a relatively low-cost method to learn about the occurrence and style of submarine volcanism. In the case where a vent has been mapped previously, difference-mapping allows one to measure the volume of new deposits.

By increasing our observations of submarine eruptions, we can better understand the styles of submarine volcanism and the processes that govern the dispersal of volcanic material. Submarine volcanoes have important consequences for Earth systems. For example, buoyant submarine plumes may mix the oceans, rafts and hydrothermal vents are known to be important homes for biota, and submarine volcanoes set the flux of material from the crust and mantle. Submarine volcanoes therefore play a potentially important, yet poorly defined role influencing ocean chemistry and climate.

Submarine lava flows and lavas entering the ocean have been spatially and temporally correlated with impulsive acoustic signals. For example, impulsive acoustic events have been documented at Gakkel ridge [151, 152], East Pacific Rise [10], Axial Volcano [150], and offshore Hawaii [153] and in all cases correlated with submarine lava flows or lava entering the ocean. Together, these observations have led to the interpretation that impulsive acoustic signals are diagnostic of submarine lava flows and are signatures of events occurring near the lava-water interface.

Despite the correlation with submarine lava flows, the mechanism/s that create these impulsive acoustic signals are not known. Several different hypotheses have been proposed including: (1) the thermal contraction and fragmentation of lavas as they contact water [e.g., 73, 151]; (2) pyroclastic magma fragmentation (driven by internal volatiles) [e.g., 10, 152, 154, 155]; (3) the collapse of vapor films; or (4) none or some combination. Discerning between these hypotheses is important because each hypothesis implies a different method or degree of fragmentation. By understanding the mechanisms that create impulsive acoustic signals, we can link these sounds not just to the presence of lava, but to specific process/es that occur in submarine lava flows. The above hypotheses could be tested with laboratory experiments were we conduct magma water interaction experiments and listen with hydrophones.

5.3 Conclusions

This dissertation has focused on understanding the dynamics of pyroclastic density currents and submarine eruptions using physical models. I proposed and modeled a new mechanism for particle entrainment in PDCs, particle splash. I concluded that particle splash can increase the runout distance of PDCs by an order of magnitude. I conducted experiments on pyroclasts in water and found that heat transfer can control pyroclast saturation rather than permeability. I found that pumice floats because of gas trapping and sinks because of gas diffusion.

Looking forward, many open questions about the dynamics of pyroclastic density currents and submarine eruptions remain. The processes that incorporate material into particle-laden flows remain poorly quantified and yet are important for understanding and modeling flow dynamics, interpreting deposits, and understanding how landscapes are evolve. While submarine eruptions are important for Earth systems, we are only beginning to observe and understand their styles, magnitudes, and frequencies. Existing data sets can be better harnessed to improve our submarine eruption catalog. Experiments and models can be combined with observations to develop a better understanding of submarine volcanism.

Bibliography

1. Miller, T. P. & Smith, R. L. Spectacular mobility of ash flows around Aniakchak and Fisher calderas, Alaska. *Geology* **5,** 173–176 (1977).
2. Fisher, R. V., Orsi, G., Ort, M. & Heiken, G. Mobility of a large-volume pyroclastic flowfffdfffdfffdemplacement of the Campanian ignimbrite, Italy. *Journal of Volcanology and Geothermal Research* **56,** 205–220 (1993).
3. Gardner, J. E., Burgisser, A. & Stelling, P. Eruption and deposition of the Fisher Tuff (Alaska): evidence for the evolution of pyroclastic flows. *The Journal of geology* **115,** 417–435 (2007).
4. Branney, M. J. & Kokelaar, B. P. *Pyroclastic density currents and the sedimentation of ignimbrites* in (2002).
5. Dufek, J. The Fluid Mechanics of Pyroclastic Density Currents. *Annual Review of Fluid Mechanics* **48,** 459–485. ISSN: 0066-4189 (2016).
6. *Volcanic Eruptions and Their Response, Unrest, Precursors, and Timing* (Washington, DC, 2017).
7. Chadwick, W. *et al.* Direct video and hydrophone observations of submarine explosive eruptions at NW Rota-1 volcano, Mariana arc. *Journal of Geophysical Research: Solid Earth* **113** (2008).
8. Deardorff, N. D., Cashman, K. V. & Chadwick, W. W. Observations of eruptive plume dynamics and pyroclastic deposits from submarine explosive eruptions at NW Rota-1, Mariana arc. *Journal of Volcanology and Geothermal Research* **202,** 47–59 (2011).
9. Resing, J. A. *et al.* Active submarine eruption of boninite in the northeastern Lau Basin. *Nature Geoscience* **4,** 799–806 (2011).
10. Tan, Y. J., Tolstoy, M., Waldhauser, F. & Wilcock, W. S. Dynamics of a seafloor-spreading episode at the East Pacific Rise. *Nature* **540,** 261–265 (2016).
11. White, J., Schipper, C. & Kano, K. Submarine explosive eruptions. *The Encyclopedia of Volcanoes (second edition): Amsterdam, Elsevier,* 553–569 (2015).
12. Jutzeler, M. *et al.* On the fate of pumice rafts formed during the 2012 Havre submarine eruption. *Nature communications* **5.** `https://doi.org/10.1038/ncomms4660` (2014).

13. Carey, R. J., Wysoczanski, R., Wunderman, R. & Jutzeler, M. Discovery of the largest historic silicic submarine eruption. *Eos, Transactions American Geophysical Union* **95,** 157–159 (2014).

14. Carey, R. *et al.* Dynamics and mass partitioning of the largest deep ocean silicic eruption of the past century. *Science Advances* (2018).

15. Bursik, M. I. & Woods, A. W. The dynamics and thermodynamics of large ash flows. *Bulletin of Volcanology* **58,** 175–193 (1996).

16. Andrews, B. J. Dispersal and air entrainment in unconfined dilute pyroclastic density currents. *Bulletin of Volcanology* **76,** 1–14 (2014).

17. Freundt, A. Formation of high-grade ignimbrites Part II. A pyroclastic suspension current model with implications also for low-grade ignimbrites. *Bulletin of Volcanology* **60,** 545–567. ISSN: 02588900 (1999).

18. Dufek, J., Manga, M. & Staedter, M. Littoral blasts: Pumice-water heat transfer and the conditions for steam explosions when pyroclastic flows enter the ocean. *Journal of Geophysical Research: Solid Earth* **112.** `https://doi.org/10.1029/2006JB004910` (2007).

19. Sparks, R. S. J. *et al.* Sediment-laden gravity currents with reversing buoyancy. *Earth and Planetary Science Letters* **114,** 243–257. ISSN: 0012821X (1993).

20. Dade, W. B. & Huppert, H. E. A box model for non-entraining, suspension-driven gravity surges on horizontal surfaces. *Sedimentology* **42,** 453–471. ISSN: 0037-0746 (1995).

21. Iverson, R. M. & Ouyang, C. Entrainment of bed material by Earth-surface mass flows: Review and reformulation of depth-integrated theory. *Reviews of Geophysics* **53,** 27–58 (2015).

22. Valentine, G. A. & Giannetti, B. Single pyroclastic beds deposited by simultaneous fallout and surge processes: Roccamonfina volcano, Italy. *Journal of volcanology and geothermal research* **64,** 129–137 (1995).

23. Dellino, P. & La Volpe, L. Structures and grain size distribution in surge deposits as a tool for modelling the dynamics of dilute pyroclastic density currents at La Fossa di Vulcano (Aeolian Islands, Italy). *Journal of Volcanology and Geothermal Research* **96,** 57–78. ISSN: 03770273 (2000).

24. Scarpati, C. & Perrotta, A. Erosional characteristics and behavior of large pyroclastic density currents. *Geology* **40,** 1035–1038. ISSN: 00917613 (2012).

25. Brand, B. D. *et al.* Dynamics of pyroclastic density currents: Conditions that promote substrate erosion and self-channelization - Mount St Helens, Washington (USA). *Journal of Volcanology and Geothermal Research* **276,** 189–214. ISSN: 03770273 (2014).

26. Kieffer, S. W. & Sturtevant, B. Erosional furrows formed during the lateral blast at Mount St. Helens, May 18, 1980. *Journal of Geophysical Research* **93,** 14793. ISSN: 0148-0227 (1988).

27. Sparks, R. S. J., Gardeweg, M. C., Calder, E. S. & Matthews, S. J. Erosion by pyroclastic flows on Lascar Volcano, Chile. *Bulletin of Volcanology* **58,** 557–565. ISSN: 0258-8900 (1997).

28. Cole, P. *et al.* Pyroclastic flows generated by gravitational instability of the 1996–97 lava dome of Soufriere Hills Volcano, Montserrat. *Geophysical Research Letters* **25,** 3425–3428 (1998).

29. Charbonnier, S. J. & Gertisser, R. Field observations and surface characteristics of pristine block-and-ash flow deposits from the 2006 eruption of Merapi Volcano, Java, Indonesia. *Journal of Volcanology and Geothermal Research* **177,** 971–982 (2008).

30. Suzuki-Kamata, K. The ground layer of Ata pyroclastic flow deposit, southwester Japan - evidence for the capture of lithic fragments. *Bulletin of Volcanology* **50,** 119–129 (1988).

31. Buesch, D. C. Incorporation and redistribution of locally derived lithic fragments within a pyroclastic flow. *Geological Society of America Bulletin* **104,** 1193–1207. ISSN: 00167606 (1992).

32. Calder, E. S., Sparks, R. S. J. & Gardeweg, M. C. Erosion, transport and segregation of pumice and lithic clasts in pyroclastic flows inferred from ignimbrite at Lascar Volcano, Chile. *Journal of Volcanology and Geothermal Research* **104,** 201–235. ISSN: 03770273 (2000).

33. Bernard, J., Kelfoun, K., Le Pennec, J. L. & Vallejo Vargas, S. Pyroclastic flow erosion and bulking processes: comparing field-based vs. modeling results at Tungurahua volcano, Ecuador. *Bulletin of Volcanology* **76,** 1–16. ISSN: 14320819 (2014).

34. Hsu, L., Dietrich, W. E. & Sklar, L. S. Experimental study of bedrock erosion by granular flows. *Journal of Geophysical Research: Earth Surface* **113.** ISSN: 21699011. doi:`10.1029/2007JF000778` (2008).

35. Roche, O. *et al.* Dynamic pore-pressure variations induce substrate erosion by pyroclastic flows. *Geology* **41,** 1107–1110. ISSN: 00917613 (2013).

36. Roche, O. Nature and velocity of pyroclastic density currents inferred from models of entrainment of substrate lithic clasts. *Earth and Planetary Science Letters* **418,** 115–125 (2015).

37. Dufek, J., Wexler, J. & Manga, M. Transport capacity of pyroclastic density currents: Experiments and models of substrate-flow interaction. *Journal of Geophysical Research: Solid Earth* **114,** 1–13. ISSN: 21699356 (2009).

38. Benage, M., Dufek, J. & Mothes, P. Quantifying entrainment in pyroclastic density currents from the Tungurahua eruption, Ecuador: Integrating field proxies with numerical simulations. *Geophysical Research Letters* **43,** 6932–6941 (2016).

39. Pollock, N., Brand, B. & Roche, O. The controls and consequences of substrate entrainment by pyroclastic density currents at Mount St Helens, Washington (USA). *Journal of Volcanology and Geothermal Research* **325,** 135–147 (2016).

40. Ungar, J. E. & Haff, P. K. Steady state saltation in air. *Sedimentology* **34,** 289–299. ISSN: 0037-0746 (1987).

41. Anderson, R. S. A theoretical model for aeolian impact ripples. *Sedimentology* **34,** 943–956. ISSN: 0037-0746 (1987).

42. Werner, B. A steady-state model of wind-blown sand transport. *The Journal of Geology* **98,** 1–17 (1990).

43. Kok, J. F., Parteli, E. J. R., Michaels, T. I. & Karam, D. B. The physics of wind-blown sand and dust. *Reports on Progress in Physics* **75,** 106901. ISSN: 0034-4885 (2012).

44. Druitt, T. *et al.* Small-volume, highly mobile pyroclastic flows formed by rapid sedimentation from pyroclastic surges at Soufrière Hills Volcano, Montserrat: an important volcanic hazard. *MEMOIRS-GEOLOGICAL SOCIETY OF LONDON* **21,** 263–280 (2002).

45. Birch, S. P. D., Manga, M., Delbridge, B. & Chamberlain, M. Penetration of spherical projectiles into wet granular media. *Physical Review E - Statistical, Nonlinear, and Soft Matter Physics* **90,** 1–8. ISSN: 15502376 (2014).

46. Mitha, S., Tran, M. Q., Werner, B. T. & Haff, P. K. The grain-bed impact process in aeolian saltation. *Acta Mechanica* **63,** 267–278. ISSN: 00015970 (1986).

47. Andreotti, B. A two-species model of aeolian sand transport. *Journal of Fluid Mechanics* **510,** 47–70. ISSN: 0022-1120 (2004).

48. Wu, C.-Y. *An energy-based splash function for the impact of particles with granular beds* in *POWDERS AND GRAINS 2013: Proceedings of the 7th International Conference on Micromechanics of Granular Media* **1542** (2013), 630–633.

49. Oger, L., Ammi, M., Valance, a. & Beladjine, D. Study of the collision of one rapid sphere on 3D packings: Experimental and numerical results. *Computers and Mathematics with Applications* **55,** 132–148. ISSN: 08981221 (2008).

50. Newhall, K. A. & Durian, D. J. Projectile-shape dependence of impact craters in loose granular media. *Physical Review E - Statistical, Nonlinear and Soft Matter Physics* **68,** 3. ISSN: 1063-651X (2003).

51. Willetts, B. B. & Rice, M. A. Collisions in aeolian saltation. *Acta Mechanica* **63,** 255–265. ISSN: 00015970 (1986).

52. Werner, B. & Haff, P. *A simulation study of the low energy ejecta resulting from single impacts in eolian saltation* in *Advancements in Aerodynamics, Fluid Mechanics and Hydraulics* (1986), 337–345.
53. Anderson, R. S. & Haff, P. K. Simulation of eolian saltation. *Science* **241,** 820–823 (1988).
54. Beladjine, D., Ammi, M., Oger, L. & Valance, A. Collision process between an incident bead and a three-dimensional granular packing. *Physical Review E - Statistical, Nonlinear, and Soft Matter Physics* **75,** 1–12. ISSN: 15393755 (2007).
55. Stroberg, T. W., Manga, M. & Dufek, J. Heat transfer coefficients of natural volcanic clasts. *Journal of Volcanology and Geothermal Research* **194,** 214–219 (2010).
56. Roche, O. *et al.* Dynamic pore-pressure variations induce substrate erosion by pyroclastic flows. *Geology* **41,** 1107–1110 (2013).
57. Huppert, H. E. & Simpson, J. E. The slumping of gravity currents. *Journal of Fluid Mechanics* **99,** 785–799 (1980).
58. Benage, M. C. *The thermal evolution and dynamics of pyroclasts and pyroclastic density currents* PhD thesis (Georgia Institute of Technology, 2015).
59. Sparks, R., Wilson, L. & Hulme, G. Theoretical modeling of the generation, movement, and emplacement of pyroclastic flows by column collapse. *Journal of Geophysical Research: Solid Earth* **83,** 1727–1739 (1978).
60. Neri, A., Esposti Ongaro, T., Macedonio, G. & Gidaspow, D. Multiparticle simulation of collapsing volcanic columns and pyroclastic flow. *Journal of Geophysical Research: Solid Earth* **108** (2003).
61. Todesco, M. *et al.* Pyroclastic flow hazard assessment at Vesuvius (Italy) by using numerical modeling. I. Large-scale dynamics. *Bulletin of volcanology* **64,** 155–177 (2002).
62. Doronzo, D. M., Valentine, G. A., Dellino, P. & de Tullio, M. D. Numerical analysis of the effect of topography on deposition from dilute pyroclastic density currents. *Earth and Planetary Science Letters* **300,** 164–173 (2010).
63. Ongaro, T., Clarke, A., Voight, B., Neri, A. & Widiwijayanti, C. Multiphase flow dynamics of pyroclastic density currents during the May 18, 1980 lateral blast of Mount St. Helens. *Journal of Geophysical Research: Solid Earth* **117** (2012).
64. Andrews, B. J. & Manga, M. Experimental study of turbulence, sedimentation, and coignimbrite mass partitioning in dilute pyroclastic density currents. *Journal of Volcanology and Geothermal Research* **225,** 30–44 (2012).
65. Dufek, J., Ongaro, T. E. & Roche, O. Pyroclastic Density Currents: Processes and Models. *The encyclopedia of volcanoes,* 631–648 (2015).
66. Lube, G., Breard, E., Cronin, S. & Jones, J. Synthesizing large-scale pyroclastic flows: Experimental design, scaling, and first results from PELE. *Journal of Geophysical Research: Solid Earth* **120,** 1487–1502 (2015).

67. Denlinger, R. P. A model for generation of ash clouds by pyroclastic flows, with application to the 1980 eruptions at Mount St. Helens, Washington. *Journal of Geophysical Research: Solid Earth* **92,** 10284–10298 (1987).
68. Garcia, M. & Parker, G. Experiments on the entrainment of sediment into suspension by a dense bottom current. *Journal of Geophysical Research: Oceans* **98,** 4793–4807 (1993).
69. Branney, M. & Brown, R. Impactoclastic density current emplacement of terrestrial meteorite-impact ejecta and the formation of dust pellets and accretionary lapilli: Evidence from stac fada, Scotland. *The Journal of Geology* **119,** 275–292. ISSN: 00221376 (2011).
70. Whitham, A. & Sparks, R. Pumice. *Bulletin of Volcanology* **48,** 209–223 (1986).
71. Allen, S., Fiske, R. & Cashman, K. Quenching of steam-charged pumice: Implications for submarine pyroclastic volcanism. *Earth and Planetary Science Letters* **274,** 40–49 (2008).
72. Jutzeler, M. *et al.* Submarine deposits from pumiceous pyroclastic density currents traveling over water: An outstanding example from offshore Montserrat (IODP 340). *Geological Society of America Bulletin* **129,** 392–414 (2017).
73. Head, J. W. & Wilson, L. Deep submarine pyroclastic eruptions: theory and predicted landforms and deposits. *Journal of Volcanology and Geothermal Research* **121,** 155–193 (2003).
74. Thomas, R. & Sparks, R. Cooling of tephra during fallout from eruption columns. *Bulletin of Volcanology* **54,** 542–553 (1992).
75. Stroberg, T. W., Manga, M. & Dufek, J. Heat transfer coefficients of natural volcanic clasts. *Journal of Volcanology and Geothermal Research* **194,** 214–219 (2010).
76. Ongaro, T. E., Cavazzoni, C., Erbacci, G., Neri, A. & Salvetti, M.-V. A parallel multiphase flow code for the 3D simulation of explosive volcanic eruptions. *Parallel Computing* **33,** 541–560 (2007).
77. Dufek, J. & Bergantz, G. Suspended load and bed-load transport of particle-laden gravity currents: the role of particle–bed interaction. *Theoretical and Computational Fluid Dynamics* **21,** 119–145 (2007).
78. Bryan, S. *et al.* Pumice rafting and faunal dispersion during 2001–2002 in the Southwest Pacific: record of a dacitic submarine explosive eruption from Tonga. *Earth and Planetary Science Letters* **227,** 135–154 (2004).
79. DeVantier, L. *et al.* Rafting of tropical marine organisms on buoyant coralla. *MARINE ECOLOGY-PROGRESS SERIES* **86,** 301–301 (1992).
80. Fauria, K. E., Manga, M. & Wei, Z. Trapped bubbles keep pumice afloat and gas diffusion makes pumice sink. *Earth and Planetary Science Letters* **460,** 50–59 (2017).

81. Rotella, M. D. *et al.* Dynamics of deep submarine silicic explosive eruptions in the Kermadec arc, as reflected in pumice vesicularity textures. *Journal of Volcanology and Geothermal Research* **301,** 314–332 (2015).
82. Vella, D. & Huppert, H. E. The waterlogging of floating objects. *Journal of Fluid Mechanics* **585,** 245–254 (2007).
83. Houghton, B. & Wilson, C. A vesicularity index for pyroclastic deposits. *Bulletin of volcanology* **51,** 451–462 (1989).
84. Horton, R. E. The role of infiltration in the hydrologic cycle. *Eos, Transactions American Geophysical Union* **14,** 446–460 (1933).
85. Assouline, S. Infiltration into soils: Conceptual approaches and solutions. *Water Resources Research* **49,** 1755–1772 (2013).
86. Turcotte, D. & Schubert, G. *Geodynamics* (Cambridge University Press, 2014).
87. Klug, C. & Cashman, K. V. Permeability development in vesiculating magmas: implications for fragmentation. *Bulletin of Volcanology* **58,** 87–100 (1996).
88. Saar, M. O. & Manga, M. Permeability-porosity relationship in vesicular basalts. *Geophysical Research Letters* **26,** 111–114 (1999).
89. Rust, A. & Cashman, K. V. Permeability of vesicular silicic magma: inertial and hysteresis effects. *Earth and Planetary Science Letters* **228,** 93–107 (2004).
90. Mueller, S., Melnik, O., Spieler, O., Scheu, B. & Dingwell, D. B. Permeability and degassing of dome lavas undergoing rapid decompression: an experimental determination. *Bulletin of Volcanology* **67,** 526–538 (2005).
91. Wright, H. M., Cashman, K. V., Gottesfeld, E. H. & Roberts, J. J. Pore structure of volcanic clasts: measurements of permeability and electrical conductivity. *Earth and Planetary Science Letters* **280,** 93–104 (2009).
92. Degruyter, W., Bachmann, O. & Burgisser, A. Controls on magma permeability in the volcanic conduit during the climactic phase of the Kos Plateau Tuff eruption (Aegean Arc). *Bulletin of Volcanology* **72,** 63 (2010).
93. Burgisser, A., Chevalier, L., Gardner, J. E. & Castro, J. M. The percolation threshold and permeability evolution of ascending magmas. *Earth and Planetary Science Letters* **470,** 37–47 (2017).
94. Colombier, M. *et al.* The evolution of pore connectivity in volcanic rocks. *Earth and Planetary Science Letters* **462,** 99–109 (2017).
95. Gonnermann, H. M. *et al.* Permeability during magma expansion and compaction. *JGR: Solid Earth* (2018).
96. Bagdassarov, N., Dingwell, D. B. & Webb, S. L. Viscoelasticity of crystal-and bubble-bearing rhyolite melts. *Physics of the earth and planetary interiors* **83,** 83–99 (1994).

97. Pedroso, R. & Domoto, G. A. Inward spherical solidificationfffdfffdfffdsolution by the method of strained coordinates. *International Journal of Heat and Mass Transfer* **16,** 1037–1043 (1973).
98. Ismail, K. & Henrıquez, J. Solidification of PCM inside a spherical capsule. *Energy conversion and management* **41,** 173–187 (2000).
99. Incropera, F. P., Dewitt, D. P., Bergman, T. & Lavine, A. Fundamentals of mass and heat transfer. *Australia: John Willey and Sons* (2002).
100. Schneider, P. J. *Conduction heat transfer* (Addison-Wesley Pub. Co., 1955).
101. Bamberger, M. & Prinz, B. Determination of heat transfer coefficients during water cooling of metals. *Materials Science and Technology* **2,** 410–415 (1986).
102. Cahalan, R. & Dufek, J. *Numerical modeling of pumice clast heat transfer dynamics in subaqueous eruptions* in (Hobart, Tasmania, 2017).
103. Clough, B., Wright, J. & Walker, G. An unusual bed of giant pumice in Mexico. *Nature* **289,** 49–50 (1981).
104. Allen, S. R., Fiske, R. S. & Tamura, Y. Effects of water depth on pumice formation in submarine domes at Sumisu, Izu-Bonin arc, western Pacific. *Geology* **38,** 391–394 (2010).
105. Allen, S. R. & McPhie, J. Products of neptunian eruptions. *Geology* **37,** 639–642 (2009).
106. Barker, S. *et al.* Geochemistry and petrogenesis of silicic magmas in the intra-oceanic Kermadec arc. *Journal of Petrology* **54,** 351–391 (2012).
107. Rotella, M. D., Wilson, C. J., Barker, S. J. & Wright, I. C. Highly vesicular pumice generated by buoyant detachment of magma in subaqueous volcanism. *Nature Geoscience* **6,** 129–132 (2013).
108. Cashman, K. V. & Fiske, R. S. Fallout of pyroclastic debris from submarine volcanic eruptions. *Science(Washington)* **253,** 275–280 (1991).
109. Allen, S. & McPhie, J. Water-settling and resedimentation of submarine rhyolitic pumice at Yali, eastern Aegean, Greece. *Journal of Volcanology and Geothermal Research* **95,** 285–307 (2000).
110. Fiske, R. S., Naka, J., Iizasa, K., Yuasa, M. & Klaus, A. Submarine silicic caldera at the front of the Izu-Bonin arc, Japan: Voluminous seafloor eruptions of rhyolite pumice. *Geological Society of America Bulletin* **113,** 813–824 (2001).
111. Kano, K., Yamamoto, T. & Ono, K. Subaqueous eruption and emplacement of the Shinjima Pumice, Shinjima (Moeshima) Island, Kagoshima Bay, SW Japan. *Journal of Volcanology and Geothermal Research* **71,** 187–206 (1996).
112. Cas, R. A. & Giordano, G. Submarine volcanism: a review of the constraints, processes and products, and relevance to the Cabo de Gata volcanic succession. *Italian Journal of Geosciences* **133,** 362–377 (2014).

113. Riley, D., Smith, F. & Poots, G. The inward solidification of spheres and circular cylinders. *International Journal of Heat and Mass Transfer* **17,** 1507–1516 (1974).

114. Richards, A. F. Transpacific distribution of floating pumice from Isla San Benedicto, Mexico. *Deep Sea Research (1953)* **5,** 29IN331–30IN535 (1958).

115. Risso, C., Scasso, R. A. & Aparicio, A. Presence of large pumice blocks on Tierra del Fuego and South Shetland Islands shorelines, from 1962 South Sandwich Islands eruption. *Marine Geology* **186,** 413–422 (2002).

116. Von Lichtan, I., White, J., Manville, V. & Ohneiser, C. Giant rafted pumice blocks from the most recent eruption of Taupo volcano, New Zealand: Insights from palaeomagnetic and textural data. *Journal of Volcanology and Geothermal Research* **318,** 73–88 (2016).

117. Bryan, S. E. *et al.* Rapid, long-distance dispersal by pumice rafting. *PLoS One* **7,** e40583 (2012).

118. Jokiel, P. L. Long distance dispersal of reef corals by rafting. *Coral Reefs* **3,** 113–116 (1984).

119. Lenormand, R., Zarcone, C., *et al. Role of roughness and edges during imbibition in square capillaries* in *SPE annual technical conference and exhibition* (1984).

120. Ide, S. T., Jessen, K. & Orr, F. M. Storage of CO 2 in saline aquifers: Effects of gravity, viscous, and capillary forces on amount and timing of trapping. *International Journal of Greenhouse Gas Control* **1,** 481–491 (2007).

121. Benson, S. M. & Cole, D. R. CO 2 sequestration in deep sedimentary formations. *Elements* **4,** 325–331 (2008).

122. Blunt, M. J. & Scher, H. Pore-level modeling of wetting. *Physical Review E* **52,** 6387 (1995).

123. Geistlinger, H. & Mohammadian, S. Capillary trapping mechanism in strongly water wet systems: comparison between experiment and percolation theory. *Advances in Water Resources* **79,** 35–50 (2015).

124. Iglauer, S., Paluszny, A. & Blunt, M. Simultaneous oil recovery and residual gas storage: A pore-level analysis using in situ X-ray micro-tomography. *Fuel* **103,** 905–914 (2013).

125. Wilkinson, D. Percolation model of immiscible displacement in the presence of buoyancy forces. *Physical Review A* **30,** 520 (1984).

126. Klug, C., Cashman, K. & Bacon, C. Structure and physical characteristics of pumice from the climactic eruption of Mount Mazama (Crater Lake), Oregon. *Bulletin of Volcanology* **64,** 486–501 (2002).

127. Rust, A. & Cashman, K. Permeability controls on expansion and size distributions of pyroclasts. *Journal of Geophysical Research: Solid Earth* **116** (2011).

128. Tait, S., Thomas, R., Gardner, J. & Jaupart, C. Constraints on cooling rates and permeabilities of pumice in an explosive eruption jet from colour and magnetic mineralogy. *Journal of Volcanology and Geothermal Research* **86,** 79–91 (1998).
129. Wright, H., Roberts, J. J. & Cashman, K. V. Permeability of anisotropic tube pumice: model calculations and measurements. *Geophysical research letters* **33** (2006).
130. Chatzis, I., Morrow, N. R., Lim, H. T., *et al.* Magnitude and detailed structure of residual oil saturation. *Society of Petroleum Engineers Journal* **23,** 311–326 (1983).
131. Stauffer, D. Scaling theory of percolation clusters. *Physics reports* **54,** 1–74 (1979).
132. Wilkinson, D. & Willemsen, J. F. Invasion percolation: a new form of percolation theory. *Journal of Physics A: Mathematical and General* **16,** 3365 (1983).
133. Wilkinson, D. Percolation effects in immiscible displacement. *Physical Review A* **34,** 1380 (1986).
134. Aveyard, R. & Saleem, S. M. Interfacial tensions at alkane-aqueous electrolyte interfaces. *Journal of the Chemical Society, Faraday Transactions 1: Physical Chemistry in Condensed Phases* **72,** 1609–1617 (1976).
135. Wildenschild, D., Vaz, C., Rivers, M., Rikard, D. & Christensen, B. Using X-ray computed tomography in hydrology: systems, resolutions, and limitations. *Journal of Hydrology* **267,** 285–297 (2002).
136. Gürsoy, D., De Carlo, F., Xiao, X. & Jacobsen, C. TomoPy: a framework for the analysis of synchrotron tomographic data. *Journal of synchrotron radiation* **21,** 1188–1193 (2014).
137. Hall, M. *et al.* The WEKA data mining software: an update. *ACM SIGKDD explorations newsletter* **11,** 10–18 (2009).
138. Clauset, A., Shalizi, C. R. & Newman, M. E. Power-law distributions in empirical data. *SIAM review* **51,** 661–703 (2009).
139. Iglauer, S. & Wülling, W. The scaling exponent of residual nonwetting phase cluster size distributions in porous media. *Geophysical Research Letters* **43** (2016).
140. Hunt, A., Ewing, R. & Ghanbarian, B. *Percolation theory for flow in porous media* (Springer, 2014).
141. Manville, V., White, J., Houghton, B. & Wilson, C. The saturation behaviour of pumice and some sedimentological implications. *Sedimentary Geology* **119,** 5–16 (1998).
142. White, J. *et al.* Settling and deposition of AD 181 Taupo pumice in lacustrine and associated environments. *Volcaniclastic Sedimentation in Lacustrine Settings (Special Publication 30 of the IAS)* **15,** p141–150 (2001).
143. Carslaw, H. & Jaeger, J. *Heat in solids* (Clarendon Press, Oxford, 1959).
144. Hungr, O., McDougall, S. & Bovis, M. Entrainment of material by debris flows. *Debris-flow hazards and related phenomena,* 135–158 (2005).

145. Breard, E. C. *et al.* Coupling of turbulent and non-turbulent flow regimes within pyroclastic density currents. *Nature Geoscience* **9,** 767–771 (2016).

146. Kelfoun, K. A two-layer depth-averaged model for both the dilute and the concentrated parts of pyroclastic currents. *Journal of Geophysical Research: Solid Earth* (2017).

147. Anderson, R. S. & Hallet, B. Sediment transport by wind: toward a general model. *Geological Society of America Bulletin* **97,** 523–535 (1986).

148. Soule, S. *Deep-Sea Synergy: Humans, Robots, and the Most Active Volcanic Systems on Earth* in (Hobart, Tasmania, 2017).

149. Graham, A., Christin Schindlbeck, J., Kaess, A., Claire Kars, M. & Brown, S. *Deciphering the Sources of Fine-Grained, Late Miocene Volcaniclastic Density Current Deposits in the Manji-Enpo Volcano-Bound Basin* in (2017).

150. Wilcock, W. S. *et al.* Seismic constraints on caldera dynamics from the 2015 Axial Seamount eruption. *Science* **354,** 1395–1399 (2016).

151. Schlindwein, V., Müller, C. & Jokat, W. Seismoacoustic evidence for volcanic activity on the ultraslow-spreading Gakkel Ridge, Arctic Ocean. *Geophysical Research Letters* **32** (2005).

152. Schlindwein, V. & Riedel, C. Location and source mechanism of sound signals at Gakkel ridge, Arctic ocean: submarine Strombolian activity in the 1999–2001 volcanic episode. *Geochemistry, Geophysics, Geosystems* **11** (2010).

153. Caplan-Auerbach, J. & Duennebier, F. Seismicity and velocity structure of Loihi Seamount from the 1996 earthquake swarm. *Bulletin of the Seismological Society of America* **91,** 178–190 (2001).

154. Sohn, R. A. *et al.* Explosive volcanism on the ultraslow-spreading Gakkel ridge, Arctic Ocean. *Nature* **453,** 1236–1238 (2008).

155. Clague, D. A., Paduan, J. B. & Davis, A. S. Widespread strombolian eruptions of mid-ocean ridge basalt. *Journal of Volcanology and Geothermal Research* **180,** 171–188 (2009).